2016

Finite Element Modeling of Active and Passive Behavior of the Human Tibialis Anterior: A Preliminary Approach

David Joda
Michigan Technological University, dbjoda@mtu.edu

FINITE ELEMENT MODELING OF ACTIVE AND PASSIVE BEHAVIOR OF THE HUMAN TIBIALIS ANTERIOR: A PRELIMINARY APPROACH

By

David B. Joda

A REPORT

Submitted in partial fulfillment of the requirements for the degree of

MASTER OF SCIENCE

In Mechanical Engineering

MICHIGAN TECHNOLOGICAL UNIVERSITY

2016

This report has been approved in partial fulfillment of the requirements for the Degree of MASTER OF SCIENCE in Mechanical Engineering.

Department of Mechanical Engineering – Engineering Mechanics

Report Advisor:	*Dr. Gregory Odegard*
Committee Member:	*Dr. Mohammad Rastgaar-Aagaah*
Committee Member:	*Dr. Tammy Haut Donahue*
Department Chair:	*Dr. William Predebon*

TABLE OF CONTENTS

ABSTRACT

This research project serves as exploratory work in the field of computational human biomechanics. A connection between muscular force and intramuscular pressure (IMP) has been uncovered that could prove invaluable in medical diagnostics as a method to circumvent the use of electromyography.

Preliminary finite element simulations were conducted to model the human tibialis anterior muscle in passive lengthening and active contraction. These simulations, totaling over 50 unique runs, utilized a novel constitutive model developed within the IMP research group. Volumetric strain, reaction forces, and pressure gradients were compared to data acquired from ongoing *in vivo* human experiments. A mechanism for passive stretching and active contraction was theorized, with the aponeuroses bearing the majority of the load due to their high stiffness.

Though the model will require future iterations to make adjustments, several promising conclusions were drawn during analysis. Fluid pressure distributions mimic those of the volumetric strain, and provide a better prediction of IMP than hydrostatic pressure. Reaction forces and pressure readings can be iterated to a reasonable level of accuracy. A thorough list of recommendations was compiled in order to guide the future direction of the model. Fluid pressures for the active contractile simulations were higher than the expected IMP values, likely owing to the stiffness of the aponeuroses being greater than necessary. Several options for addressing this issue were proposed, such as decreased aponeurosis length and graduated thickness and stiffness of the elements in the extremes of the parts.

1. INTRODUCTION

This master's report summarizes the initial exploratory efforts in creating a functional finite element model of passive and active behavior of the human tibialis anterior muscle (TA). A provided finite element mesh and constitutive material model were used to simulate passive lengthening and active contraction of the TA. This report describes the methods used, simulation protocol and initial results. It provides potential causes of the disparity between simulation results and human data, and lists improvements to be made in future iterations of the model.

1.1 MOTIVATION

Computational modeling in human biomechanics is a promising field. Creating functional computer models of human tissue can prove invaluable to researchers and engineers alike.

A research group of engineers and scientists from Michigan Technological University, Colorado State University, and the Mayo Clinic in Rochester, MN, have spent the past decade studying the correlation between intramuscular pressure (IMP) and muscular force during passive and active behavior. Previous work within this group has modeled a rabbit (lapine) tibialis anterior using the finite element method and a hyper-poro-viscoelastic constitutive model (described in Section 3) to create material parameters for the muscular tissue and surrounding connective tissue, called aponeuroses. These simulations have had some success in matching selected *in vivo* data collected from Giant Flemish rabbits [1].

Concurrently, researchers at the Mayo Clinic have conducted *in vivo* human trials to gather data for the human tibialis anterior in both passive and active situations. Given the success of the material model and FEM simulations matching the lapine data, the group elected to analyze the effectiveness of the material model in a human muscle by simulating these passive and active experiments in a computational setting. This report summarizes the efforts to mimic these experiments computationally. The results were analyzed, roadblocks to success identified, and recommendations given for improvements in the next iteration of the human model.

1.2 INTRAMUSCULAR PRESSURE

The IMP research group is testing a theory that IMP provides a better picture of muscular behavior than the electrical impulses collected through electromyography (EMG). This is because EMG only monitors neural impulses sent to the muscle tissue; it does not actually measure what the muscle is doing [2]. A physically damaged or diseased muscle may still receive neural impulses, but not generate force according to the intensity of the signal. A further advantage of studying IMP involves the observation of passive muscular behavior such as stretching, in which no impulses may be recorded by the EMG in the muscle since it is not active.

However, the similarities between IMP and muscular behavior seen in previous research are unique. In informal work conducted by the IMP research group, IMP has shown to have a direct correlation with both muscle lengthening (passive tension) and muscle contraction. This is interesting because it means IMP increases with both a passive length increase and an active length decrease. Because of this, the relationship between IMP and computational pressure measurements seems to fall somewhere between the hydrostatic and fluid pressure measurements from FEM programs. IMP is also known to increase with muscle depth and near stiffer structures such as bone and connective tissue [3].

1.3 RABBIT MODEL

The muscular material model has been applied to an FEM simulation of a lapine TA. These simulations were conducted to mimic the experimental work of Davis, et al [4], in which a lapine TA was transected near the insertion and lengthened using an apparatus in order to isolate reaction forces generated by the muscle.

The rabbit model, created by Mr. Benjamin Wheatley, a Ph.D. student at Colorado State University, has been optimized through the testing of small strips of lapine TA tissue in the

longitudinal and transverse directions. Wheatley was able to successfully model whole-muscle simulations of passive stretching in the isolated lapine TA, mimicking that of [4]. However, the model was not as transferrable to data collected in an identical manner by researchers at the University of California – San Diego.

This epitomizes the inherent difficulty in fitting finite element method (FEM) models to real-world data. As such, it is acknowledged that this attempt to transfer muscle parameters from a lapine to human model will encompass its own challenges. Iteration to an accurate model will undoubtedly take some time.

1.4 GOALS AND TASKS

This is a first attempt to combine the constitutive model used by the IMP research group with a human muscle simulation. In fact, there is very limited evidence of previous work to simulate the behavior of the human TA using FEM. A literature search of ProQuest and PubMed was conducted to search for existing studies. This search is discussed in Section 3.3. As such, this is a preliminary work which focuses on identifying immediate roadblocks within the model and methods to improve them. The goals for this research project can be summarized as follows:

1. Combine prior knowledge of the IMP distribution in skeletal muscle with a novel constitutive model and a human TA mesh to conduct FEM simulations of passive lengthening and active contraction.
2. Compare simulation results to experimental data. Draw conclusions from the comparison and provide suggestions for future research in this direction.

These goals were expanded into nine overall tasks:

1. Analyze human *in vivo* data from passive lengthening and active contractile experiments. Gather key trends and target data to create benchmarks for computational simulations.

2. Convert human TA mesh to usable format within selected solver (FEBio – discussed in Section 4).
3. Conduct mesh convergence study to ensure accurate simulation results and appropriate mesh density.
4. Determine applicable boundary conditions, loads, constraints, and other FEM parameters for passive and active simulations.
5. Simulate passive lengthening and active contractile experiments using FEM.
6. Conduct applicable post-processing to analyze passive and active simulations. Investigate trends and gather similar data to allow comparison between computational and *in vivo* work.
7. Compare results of human experiments and FEM simulations. Identify similar trends and data points, as well as disparities in the data.
8. Propose theories for differences between human and FEM data, make initial adjustments and run follow-up simulations if applicable.
9. Gather conclusive findings and discuss improvements in the FEM model for future iterations of the human TA simulation.

2. HUMAN TIBIALIS ANTERIOR

2.1 OVERALL STRUCTURE AND FUNCTION

The human tibialis anterior is a fusiform muscle located in the anterior compartment of the distal lower limb. Adjacent to the tibia, this muscle is the main force associated with dorsiflexion and inversion of the foot [5]. The TA is bipennate, with anterior and posterior sections that travel at ±5° from the longitudinal axis of the muscle [5]. It originates from the proximal 2/3 of the tibia, specifically the tibial tuberosity, anterior fascia and interosseous membrane. The muscle inserts at the base of the first metatarsal via a central tendon that traverses the ankle joint.

Figure 2.1 illustrates the shape and position of the human tibialis anterior muscle, seen just lateral to the tibia in the image.

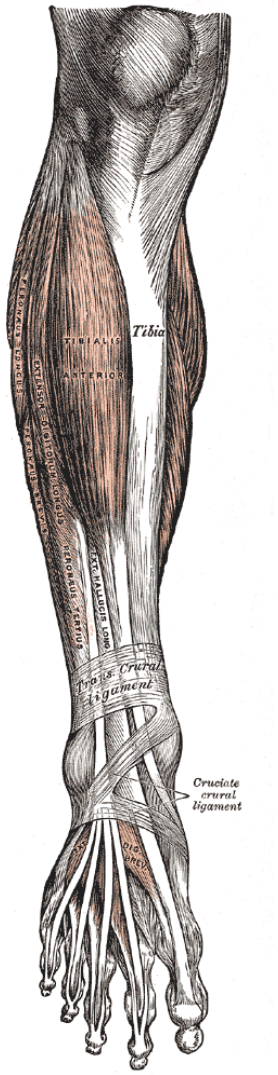

Figure 2.1: Drawing of the distal lower limb including the tibialis anterior (center), taken from the 20th edition of Gray's Anatomy (public domain) [5].

2.2 APONEUROSES

Confounding the otherwise simple nature of the TA are sections of stiff connective tissue known as aponeuroses. The human TA system includes aponeuroses that wrap around the exterior of the muscle on the proximal ¾ of its length, consisting of skin and fascia on the anterior side and

the interosseous membrane on the posterior side. Additionally, an aponeurosis extends upward from the distal region of the muscle, effectively bisecting the belly of the muscle to form the anterior and posterior sections. This aponeurosis culminates in the central tendon at the insertion of the TA [5]. Together, these three aponeuroses serve to provide structural support for the belly of the TA muscle and continuous connections to tendinous material on the muscle's exterior.

Figures 2.2-2.3 are images taken during a post-mortem autopsy of the human TA by researchers at the Mayo Clinic [6]. These images provide a graphical explanation of the TA components and connective tissue.

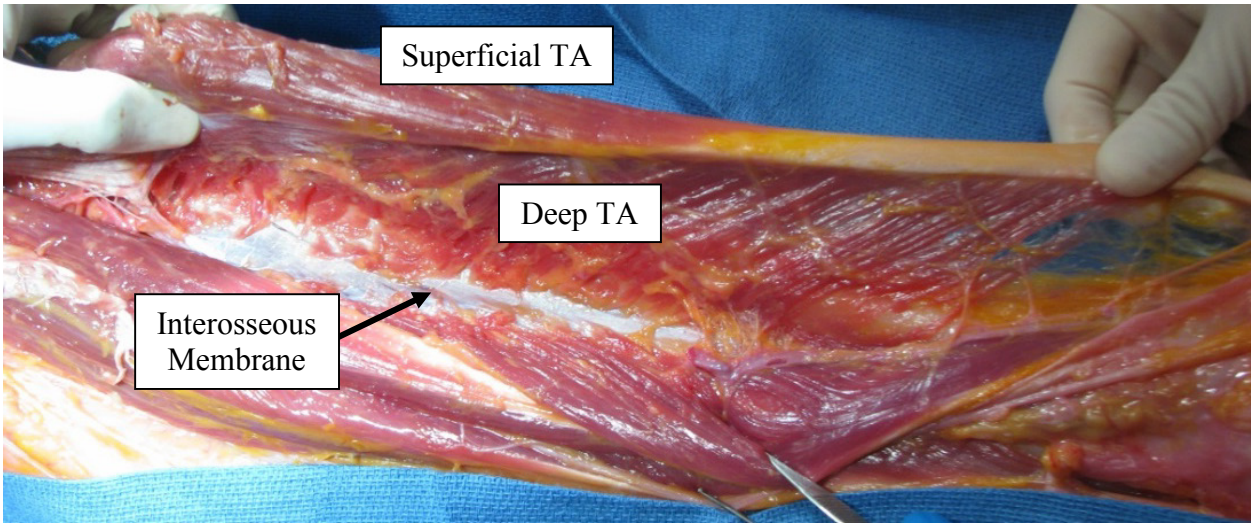

Figure 2.2: Human TA cadaveric study images. The superficial (anterior) and deep (posterior) components of the muscle can be seen, with the posterior fibers extended. The progression from the central tendon to the fiber insertion on the interosseous membrane (posterior aponeurosis) can be seen [6].

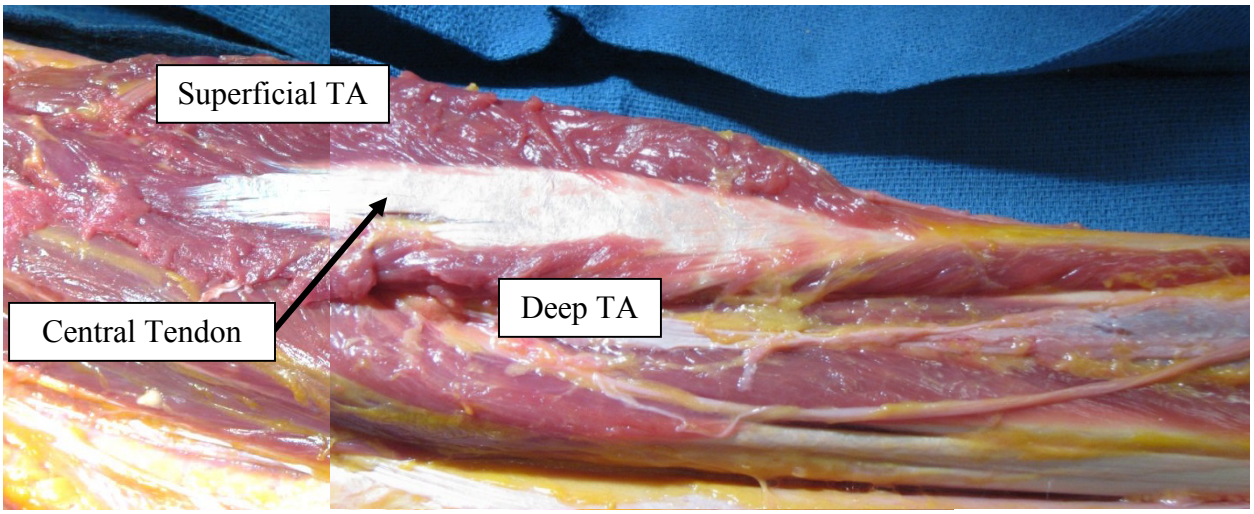

Figure 2.3: Human TA cadaveric study images. Lateral view of the TA, showing the superficial (anterior) and deep (posterior) sections of the muscle diverging from the central tendon [6].

2.3 RATIONALE FOR SELECTION

There are several reasons for the continued use of the tibialis anterior muscle as an entry point in this field of computational biomechanics. First, the TA is located in a limb of the body, meaning it is far from internal organs and other crucial bodily structures. Second, the muscle is positioned superficially, thus it can be easily accessed through the skin and outer fascia for measurements and transection, if needed. Finally, and perhaps most importantly, the tibialis anterior is virtually isolated in its action of dorsiflexion of the foot. Because of this, experiments involving dorsiflexion can measure the strength and quality of the TA without interference from other tissue. This data collection can also be done less invasively, as there is no need to isolate the muscle fibers within the body for measurement.

3. FINITE ELEMENT MODELING IN BIOMECHANICS

Computational modeling can be a very useful tool, especially in a research field such as biomechanics. Having virtual models that can be used to simulate real-world experiments can bypass the need for institutional review boards, human subject training and strict guidelines for experimental protocol. It also allows the researcher to study small changes in the protocol by controlling or iterating specific variables. In essence, a virtual tissue model can significantly

speed up research by simplifying the experimental process and making it possible to test multiple theories in a short time.

However, the benefits of added flexibility and decreased time for experiments do not come without corresponding drawbacks. Computational modeling requires a thorough understanding of the physics and mechanisms involved in the real-world experiment to be modeled. That is, because the researcher is responsible for setting up the simulation, he or she must know the proper techniques to do so. Barring that, one must be prepared to devote significant time to methods of trial-and-error to determine the optimum modeling parameters.

The finite element method involves subdividing a computational model into many small divisions, called elements. Together the elements form the mesh for a given model. This mesh is assigned material properties through various material parameters. In this case, a constitutive material model is used to simulate the behavior and physical properties of skeletal muscle. Additionally, the mesh is subject to boundary conditions such as loads and constraints. Loads can be surface forces applied to a specific part of the mesh (point loads, supports, etc.) or body forces that affect the entire mesh equally (gravity, magnetism, etc.). Constraints are physical manifestations of typical mechanical implements, such as pins or rollers, which secure part of the mesh in assigned degrees of freedom. Boundary conditions can also involve prescribed displacements in place of loads, if one desires to apply a measured degree of movement and examine the results. Combined, the mesh, constitutive model and boundary conditions comprise the backbone of a finite element simulation.

Once the finite element model is prepared, the time variants of the simulation are input. This research project utilizes transient, or dynamic, simulations, because the computations are designed to follow time-variant experimental data. Solution methods involve calculating various mechanical parameters such as displacement, force, stress, and strain in each element. The differences between these parameters for each element form residuals. The solver will iterate the simulation for each step until such time as the residuals fall below a desired degree of accuracy.

3.1 BENEFITS AND LIMITATIONS FROM UNIFORMITY

A key difference between real-world data and that from FEM lies in uniformity and repeatability. Due to the computational nature of FEM, repeated trials of the same simulation will result in identical results. This is highly unlikely in real-world experiments. Because of this, the results of a computational simulation should never be taken as "true," especially in the presence of experimental data. However, this means that FEM is a useful tool when accompanied or validated by experimental results.

3.2 SOLVER AND SOFTWARE

The meshes used in this research project were constructed in TrueGrid. From here, initial pre-processing was done using Abaqus CAE. This involved selecting appropriate surfaces for the aponeuroses and creating element sets for the anterior and posterior muscle sets. Finally, the simulation setup, calculations, and post-processing utilized the FEBio software suite. The programs within this suite consist of PreView, FEBio, and PostView.

PreView is a pre-processing program used to define the mesh and corresponding boundary conditions. It also allows the user to create simulation parameters, such as the type of simulation, timesteps and optimal iterations while solving. FEBio is an open-source FEM solver capable of a linear or non-linear format. All information is output in text-friendly files that can be manually edited without major difficulty if required. PostView is a relatively simple post-processer allowing users to graphically examine simulation data and perform low-complexity post-processing, such as outputting simulation parameters of elements or nodes selected within the GUI. This software suite is developed and maintained by a research group out of the University of Utah. As such, the programs are continuously under development, with frequent iterative releases to fix bugs or processing errors discovered by users. A major benefit of the software is the many bio-related functions that are built into the program, specifically in the definitions of complex materials. FEBio even has a "Muscle material" definition used as an

overarching simulation of muscle tissue, along with a function to define an active contraction in any coupled material [7].

3.3 PREVIOUS WORK FOR THE HUMAN TIBIALIS ANTERIOR

There is limited evidence of previous studies of FEM modeling of the human tibialis anterior. A search of ProQuest and PubMed uncovered one study that used New Zealand rabbits to gather mechanical properties of the lapine TA. These parameters were used to create a "transversely isotropic viscoelastic continuum model" of lapine TA muscle fibers [8]. The constitutive model developed in this study is very similar in theory to that developed for these simulations. However, the authors of this paper only sought to verify their constitutive model against *in vivo* lapine data. There was no attempt to transfer this model into a human simulation. Other studies created an FEM model of rat TA muscles, again with no foray into the human tissue system [9]. Jenkyn, et al, focused on the ties between IMP and muscular force in lapine TA tissue when they created a novel finite element model that effectively mimicked IMP distributions with hydrostatic pressure from the model [10].

One study attempted to model human muscular tissue. Blemker, et al, created a simplified model of the biceps brachii to model strain distributions in the muscle [11]. Some of the mathematical parameters for this model were used in the constitutive model for these simulations because of their ability to help match experimental data. Together, these works provide useful insight in the current state of research with regards to human skeletal muscle, IMP and computational biomechanics. To date, no research was found with the purpose of analyzing the connection between force and IMP in human skeletal muscle such as the TA.

Additionally, this is the first attempt to combine the constitutive material model from the IMP research group with a human TA study. To this point, all research has used the rabbit model due to ease of gathering a larger amount of experimental data. Only recently has the Mayo Clinic begun to collect human data for behavior of the TA, so thus the need for an FEM human model has also become relevant of late.

Because the IMP research group has spent the better part of decade constructing and testing lapine FEM models, the focus for this research project will be to lay the foundation for future work in the human TA field. Therefore, perhaps more important than the initial simulation results is the need for future direction for the model. It will be especially important to note opportunities for improvement that arise during the simulations and analysis of data, and elaborate on these in the final sections of this report.

4. CONSTITUTIVE MODEL

A major objective of this research project was to utilize an existing constitutive model, which has had some success in lapine TA simulations, and apply it to a human TA muscle simulation. This constitutive model was also developed by Mr. Benjamin Wheatley from Colorado State University.

4.1 EQUATION DESCRIPTION

The constitutive model is described as hyper-poro-viscoelastic, meaning it has three separate components. A viscoelastic component is used to define time-dependent behavior, while the porous component defines a fluid-solid mixture and corresponding permeability of muscle tissue. Lastly, the elastic component models the transversely isotropic fibrous material within muscle tissue. The basic equations of the constitutive model are shown below.

A hyperelastic material is one designed to handle large deformations, where a strain energy density (SED) function defines the interaction between stress and strain. The constitutive model utilitizes a decoupled transversely isotropic SED function that is dependent on the right Cauchy-Green deformation tensor as shown below:

$$\Psi_p(\boldsymbol{C}) = \Psi_p(\bar{\boldsymbol{I}}_1, \bar{\boldsymbol{I}}_2, J, \bar{\boldsymbol{I}}_4) = \Psi_p{}^{iso}(\bar{\boldsymbol{I}}_1, \bar{\boldsymbol{I}}_2, \bar{\boldsymbol{I}}_4) + \Psi_p{}^{vol}(J)$$

The decoupled designation indicates that the SED function can be broken down into volume-preserving (isochoric/deviatoric) and volume-changing (volumetric) behavior, as shown below:

$$\Psi_p{}^{iso} = \sum_{i=1}^{N} a_{2i}(\bar{\boldsymbol{I}}_1 - 3)^{2i} + \sum_{i=1}^{N} b_{2i}(\bar{\boldsymbol{I}}_2 - 3)^{2i} + \sum_{i=1}^{N} d_{2i}(\bar{\boldsymbol{I}}_4 - 1)^{2i}$$

$$\Psi_p{}^{vol} = \sum_{i=1}^{N} c_{2i}(J - 1)^{2i}$$

The viscoelastic behavior of the muscle is modeled using a Prony Series, which controls the relaxation of a particular modulus over time at a constant load. This behavior uses viscoelastic coefficients (g) and time constants (τ) according to the following equation:

$$g(t) = 1 - \sum_{i=1}^{N} g_i \left[1 - exp\left(-\frac{t}{\tau_n}\right)\right]$$

Finally, the poroelastic component defines the relationship between fluid and solid components within the muscle. The purpose of this component is to give the material the compressive stiffness a fluid can provide while concurrently containing the tensile strength of muscle fibers. The poroelasticity of the muscle material is defined by its permeability, which in turn depends on an adaptation of Darcy's Law:

$$q = \frac{-k\nabla p}{\mu}$$

Where q is the flow rate, k is the permeability, ∇p is the pressure gradient, and μ is the fluid viscosity. Typically the permeability is not constant because it changes as the material deforms, but a constant permeability was used in this case to simplify the model [12].

Together, these three components form the constitutive material models for this research project. The connective aponeurosis tissue does not contain the fluid component; rather, it is modeled as an uncoupled viscoelastic material. The mathematical parameters used for each material model were determined by fitting the constitutive model to experimental tensile testing data from lapine TA tissue. These parameters are listed in Section 6.

4.2 RABBIT MODEL

As stated previously, this equation has been used with some recent success in a lapine TA model to simulate passive lengthening of a transected, isolated muscle. Prior to this work, a similar constitutive model was used to model a lapine meniscus in a passive anisotropic fashion [13]. This is the first attempt to combine the hyper-poro-viscoelastic constitutive model with a human TA simulation, as well as the first attempt at modeling an active contraction using this constitutive model.

5. HUMAN EXPERIMENTS

Prior to conducting the FEM simulations, findings were gathered from the *in vivo* experiments for which these computational simulations were modeled. These experiments covered passive lengthening and active contraction of the human TA conducted at the Mayo Clinic in Rochester, MN. Both sets of data are as of yet unpublished and the active contraction trials ongoing. However, they do provide a good foundation against which to compare findings from the FEM simulations.

5.1 PASSIVE LENGTHENING

The passive lengthening data was collected by Dr. Elizabeth Jensen, a former Ph.D. student working with the Motion Analysis Laboratory in the Orthopedic Research Division of the Mayo Clinic in Rochester, MN, under Dr. Kenton Kaufman. Jensen's study attempted to quantify the volumetric strain distribution within the TA muscle so as to provide a building block for understanding the IMP-muscle force relationship. Because volumetric strain and IMP have been shown to increase with muscle depth and near bodily structures with increased stiffness such as bones, Jensen believed that volumetric strain was an appropriate replacement for IMP [3].

5.1.1 EXPERIMENTAL SETUP

This study used MRI to continuously scan a patient's ankle as it was rotated in 26° of plantarflexion from the neutral axis, thus lengthening the TA muscle. After scanning the neutrally-positioned TA to gather anatomical data, Jensen used an apparatus to control the plantarflexion along a 2s cycle while the MRI continuously scanned the region. The anatomical scans were used to create a finite element mesh – the same geometry used in the mesh for this research project. The velocities from the second MRI scan were mapped onto the anatomical data to create a deformed mesh with corresponding velocities. These velocities were used to compute the volumetric strain in each element.

The volumetric strains were first output in the overall mesh for qualitative analysis, and then further analyzed by subdividing the mesh into slices. First, five transverse superior-inferior partitions were made in the mesh, followed by a further ten longitudinal slices in either the anterior-posterior or medial-lateral directions, as shown in Figure 5.1 below. The average volumetric strain for each slice was plotted on separate charts for the anterior-posterior and medial-lateral slices, respectively. Finally, statistical analysis was conducted to determine the significance of any variation seen in the data.

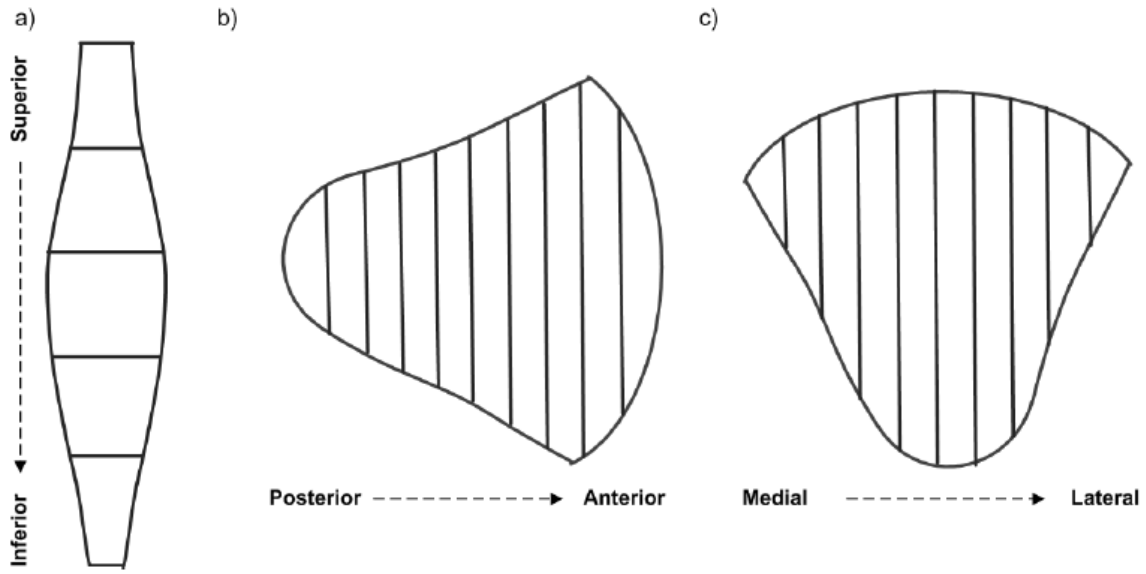

Figure 5.1: Illustration of partitions used to define slice data in Jensen's study [3]. This procedure will be reproduced in the passive lengthening FEM studies.

5.1.2 DATA

As seen Figure 5.2 below, the strain distribution calculated in Jensen's study was clearly non-uniform. Gray and red regions indicate areas of very high strain (up to 47% seen), while black areas indicate regions of low or compressive strain (up to -20% seen).

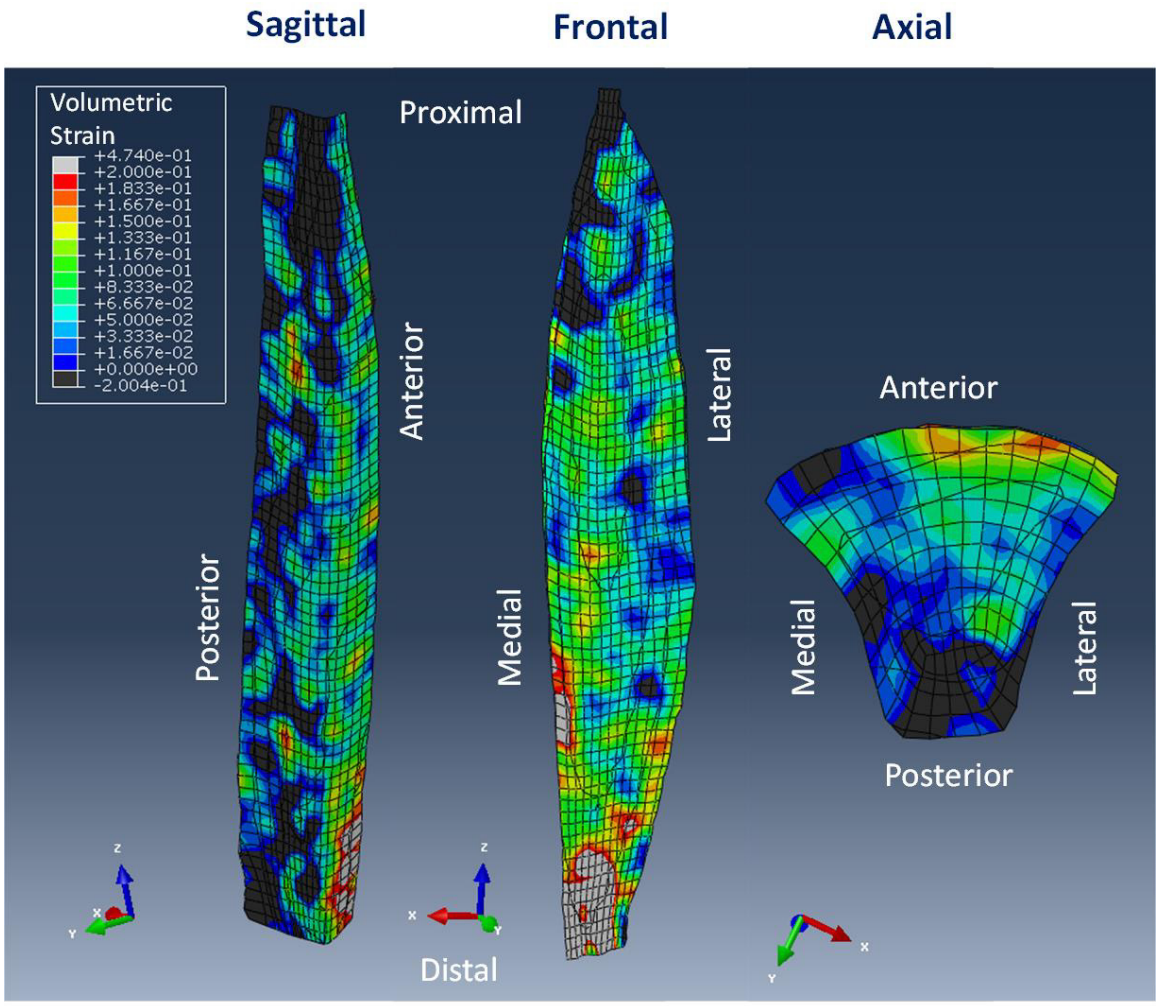

Figure 5.2: Overall volumetric strain distribution seen from Jensen's studies. Note the high strain regions located distally and anterior, and the compressive strain seen in the posterior region [3].

The slice data from Jensen's study was digitized and reproduced in Figures 5.3-5.4 below. The series SI1-SI5 represent the transverse partitions, with 1 corresponding to the most superior (proximal) and 5 the most inferior (distal)

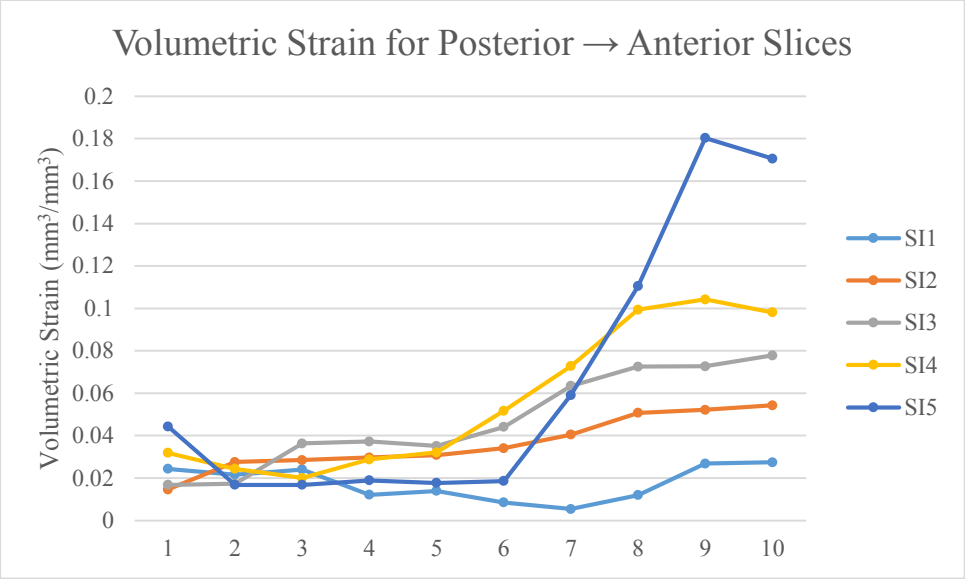

Figure 5.3: Volumetric strain plot reproduced from Jensen's data for the posterior-anterior slices.

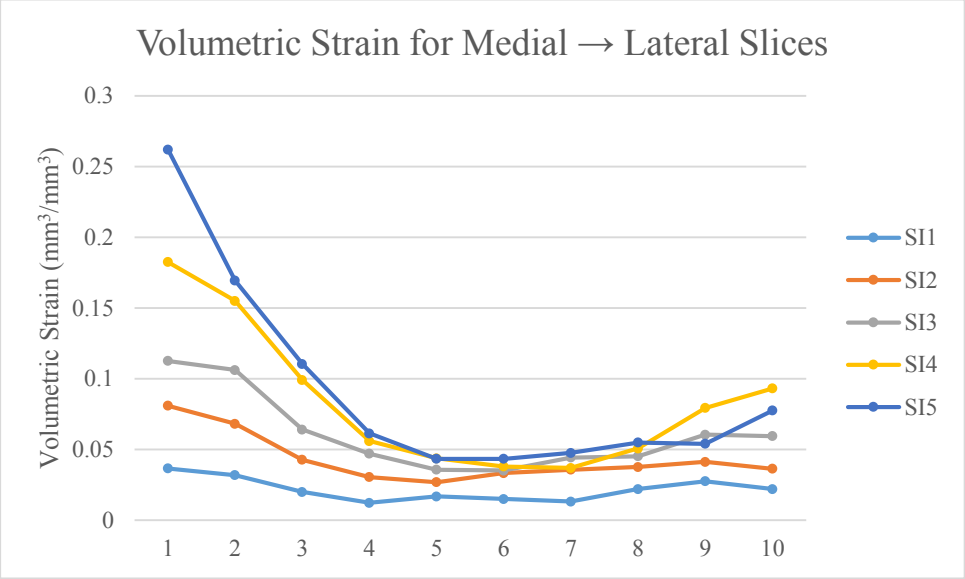

Figure 5.4: Volumetric strain plot reproduced from Jensen's data for the medial-lateral slices.

As seen above, Jensen identified a clear increasing trend from posterior to anterior in volumetric strain, as well as a decreasing trend from medial to lateral. Additionally, she noted that strain tended to increase in distal partitions (SI5 had the highest reported strain, SI1 the lowest). These findings were statistically significant for most slice values.

5.1.3 CONCLUSIONS

Jensen concluded that volumetric strain follows a non-uniform distribution in the human TA muscle with an increasing trend in anterior, medial, and distal regions. Jensen noted that all slices output a positive volumetric strain, which correlates to a volume increase and a corresponding pressure drop. Because of this, she hypothesized that the mechanism for IMP generation must be based within the muscle fibers (she provided evidence of muscle fiber volume shrinking during stretching), as a positive volumetric strain would generally result in a drop in pressure [3].

Perhaps more important than specific findings are the general benchmarks for volumetric strain that can be gathered from Jensen's data regarding passive lengthening of the human TA. Much of the strain appears to be clustered in the 0-5% range, with maximum slice averages peaking around 20%. Interestingly, although Jensen's slice data did not report any compressive volumetric strain, the raw data in Figure 5.2 show significant portions of the mesh with the dark color corresponding to compressive strain – especially in the posterior region. This may correlate to only superficial compressive strains, or could show some compressive data being masked by the slice values. Indeed, strain values in the posterior slices (#1-4 in Figure 5.3) seem clustered at or below 2%. The strain contours shown above have definite stagnation regions (slices 3-5 in the PA direction and 5-7 in the ML direction) which indicate relative uniformity in the strain distribution.

5.2 ACTIVE CONTRACTION

The active contractile data was collected by Dr. Shanette Go, an MD-Ph.D. student in the Mayo Clinic Medical Scientist Training Program. Go's ongoing study is measuring force, IMP and EMG readings during isometric contraction of the human TA. The goal of this study is to investigate the relationship between these three variables in hopes of furthering the understanding of connections between IMP and muscular force.

5.2.1 EXPERIMENTAL SETUP

Go's study runs three sets of trials for each subject, with 15 repetitions of each trial. First, subjects are lying prone with their right ankle secured in a stationary apparatus. A load cell (SM-50 - Interface, Inc., Scottsdale, AZ) was secured on the apparatus oriented near the insertion of the TA at the base of the first metatarsal. The pressure transducer (FOP-M260 - FISO Technologies, Inc., Quebec, Canada) was positioned in the belly of the muscle, approximately 6cm distal to the origin of the TA near the tibial tubercle [14].

The force of the maximum voluntary contraction (MVC) of each patient's TA was first measured using the load cell. After measuring this force, the 50% MVC force became the target force for each subsequent trial. Fifteen repetitions of this contraction were conducted at varying rates. These contraction rates were 5%, 10% and 15% of MVC/s, corresponding to a total time to reach 50% MVC of 10s, 5s, and 3.33s, respectively. A plot of the directed force vs. time was shown on a screen within view of the patient, where it was to be followed as closely as possible by the patient during the trial. Thus, there was some human error introduced into the experiments since it was the responsibility of the patient to follow the force curve as closely possible. The general protocol for each run was a 5 second initial period with no force applied, the ramp of force up to the prescribed 50% MVC, and a 10 second relaxation period with no applied load. Data were collected at a sampling rate of 2500Hz. Following 15 trials at each contraction rate, the data was compiled and transformed according to the impedance readings of the force and pressure transducers.

5.2.2 DATA

Because of the preliminary nature of this research project as well as the Mayo experiments, only data from one patient was analyzed for this report. Additionally, because all contraction rates finished at 50% MVC, only the 5% MVC/s trial was analyzed for this patient. This means that the experimental data cannot be considered a representative sample of the human population as a

whole. Ideally, as the FEM model develops, more experimental data will be available for comparison, thus strengthening the findings of this research.

The transformed data for all 15 trials of the 5% MVC/s contraction rate were analyzed to determine the baseline and peak force and pressure values for each run, which were then averaged. The resulting values are shown below in Table 5.1:

Table 5.1: Statistical averages gathered from Go's active contractile data, 5% MVC/s contraction rate [14]

F_{max} (N)	**77.331**
IMP_0 (mmHg)	493.468
IMP_{max} (mmHg)	519.187
ΔIMP (mmHg)	25.719
ΔIMP (kPa)	**3.429**

The average force for 50% MVC for this patient's data was 77.331N. After converting the difference in pressure from the given mmHg to kPa (units used by the FEBio solver), the pressure increase allotted to 3.429kPa on average. It is interesting to note that the initial pressure seen on all runs is much higher than zero gage pressure. This indicates that there is a substantial initial IMP even when the muscle tissue is completely relaxed, providing another reason to consider IMP as an adaptation of the pressure readings calculated in the simulations.

Plots of one representative run in the 5% MVC/s trial are shown below to illustrate the typical force vs. time and IMP vs. time curves seen in these experiments.

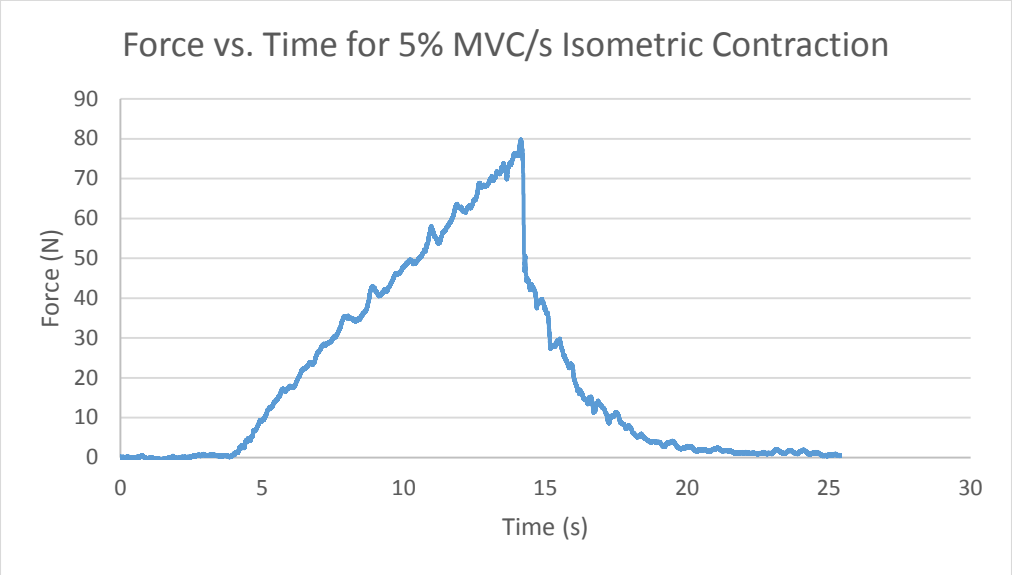

Figure 5.5: Force vs. time plot of a representative trial for the 5% MVC/s contraction rate showing the initial baseline, force ramp and relaxation phases.

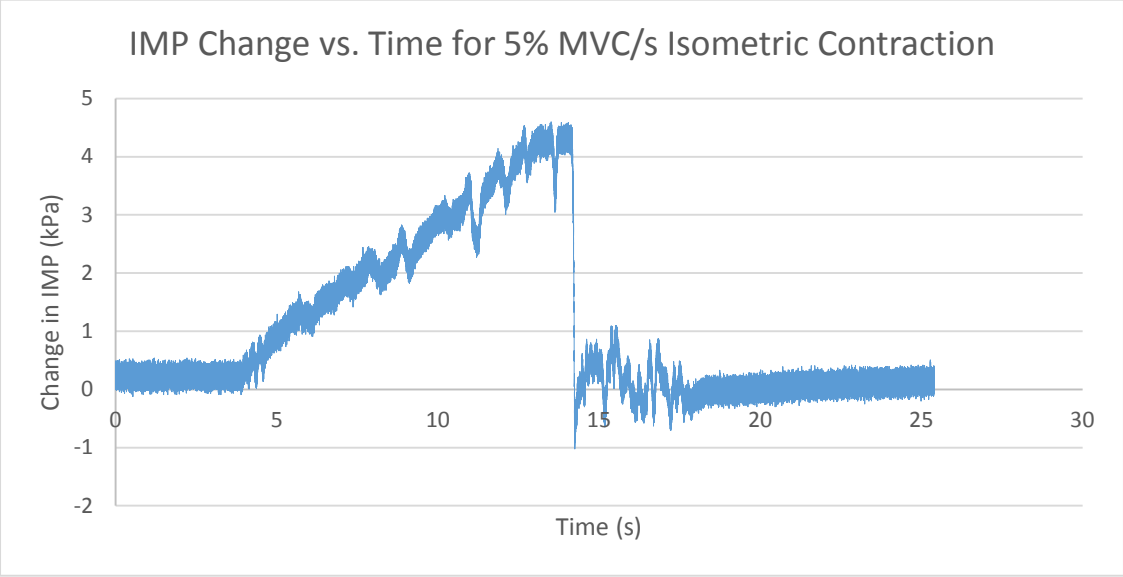

Figure 5.6: IMP change vs. time plot of a representative trial for the 5% MVC/s contraction rate showing pressure oscillations during the initial baseline, force ramp and relaxation phases.

The ΔIMP vs. time plot shows a high degree of oscillation in the pressure readings, likely owing to the sensitivity of the pressure transducer, among other effects. In order to better examine the pressure data and its comparison to the force readings, a 10-point moving average in the pressure

data was created to smooth out the oscillations. This series was overlaid against the force vs. time data on a single plot shown in Figure 5.7.

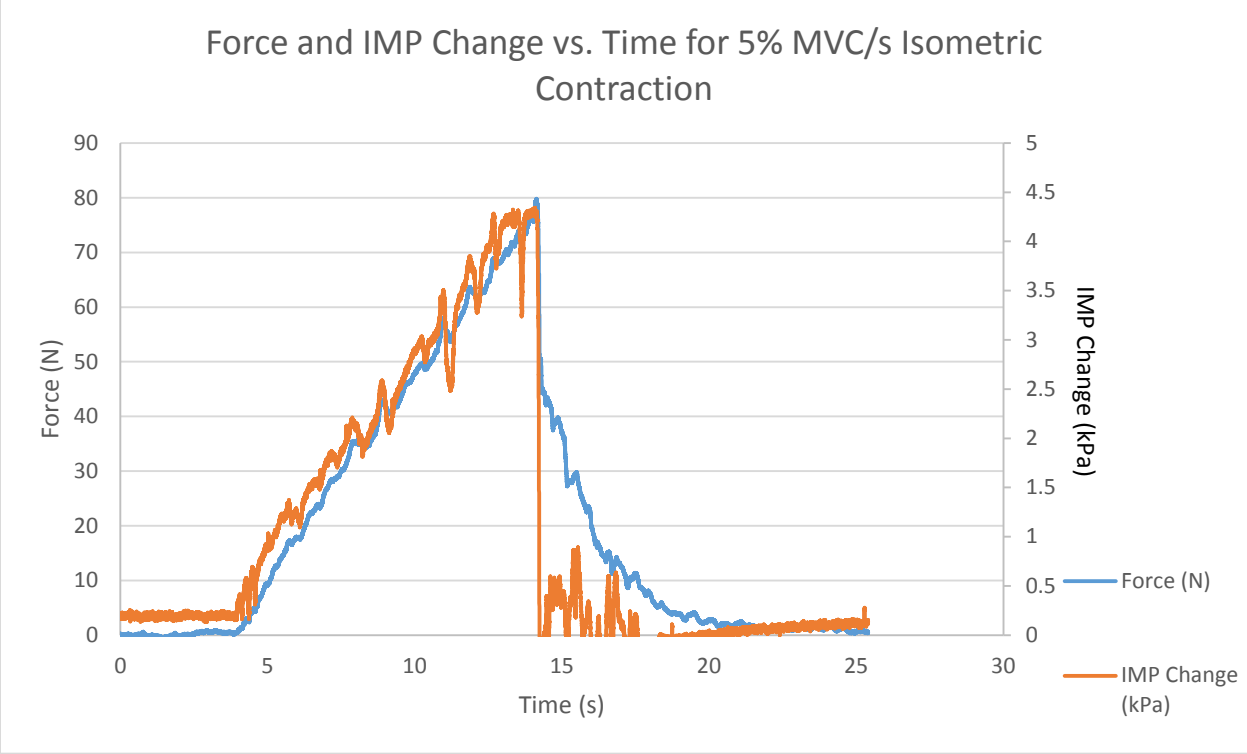

Figure 5.7: Comparison of force and ΔIMP illustrating the strong correlations in the data aside from the pressure drop-off at the initiation of the relaxation phase.

As shown, there is a high degree of similarity between the force readings and the IMP moving average. The larger oscillations in the pressure readings tend to mimic those of the force data. However, the gradual relaxation curve seen in the force series corresponds to a sharp drop in IMP back to its baseline level, indicating that the mechanisms for IMP must differ between contraction and relaxation.

5.2.3 CONCLUSIONS

A strong correlation was seen between force readings taken near the human TA insertion site and the change in IMP seen at a location in the proximal belly of the muscle. This provides further evidence that an empirical relationship between IMP and muscle force could prove beneficial

towards medical diagnostics. The data from these experiments will be used as a general benchmark for the active simulations conducted for this research project.

It should be noted that the data in these experiments comes from a single patient, from which 15 runs of a single experimental trial were conducted. This greatly diminishes the significance of the experimental results, but still can provide us a good target for preliminary simulation data. As Go's work progresses with more patients and further trials, the average peak force and change in IMP will become more robust, and thus will provide a stronger standard for which to tailor the FEM simulations.

6. MESH AND SIMULATION SETUP

The original mesh used for the FEM simulations in this research project was identical to that of the one used by Jensen in her passive lengthening experiments. The anatomy and structure of the first mesh attempt are the same. However, because Jensen was only mapping velocity values to corresponding nodal coordinates, she did not require a robust mesh from a density standpoint. Corrective actions for this issue are touched on in Section 7.

6.1 ELEMENTS AND SIZE

The original mesh comprised 12734 elements, the majority of which were 8-noded hexahedral bricks with some 4-noded quadrilateral shell elements. It models a transected version of the human TA muscle, in which the proximal and distal connective tendons are removed to leave the main belly of the muscle. This simplifies the simulations by removing additional variables associated with tendons, muscle origin and insertion, and other factors. The resulting mesh is approximately 170mm in length, and roughly 30mm in maximum transverse diameter. It is asymmetrical in that the shape and volume of the anterior and posterior muscle halves are not identical. However, each muscle half contains the same number of elements. An image of the mesh is shown below in Figure 6.1, which includes the anterior and posterior muscle components as well as the aponeuroses.

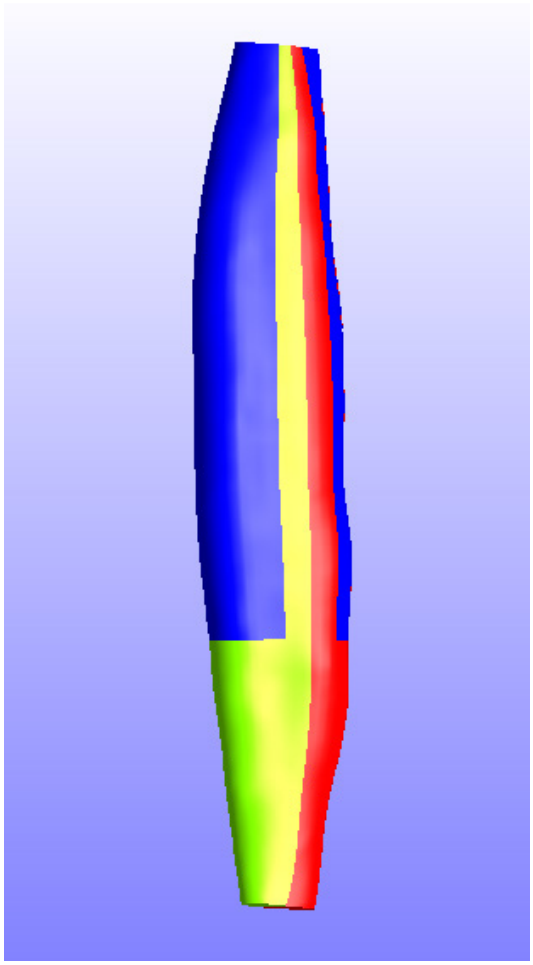

Figure 6.1: Overview of the human mesh showing the external aponeuroses (blue), the anterior muscle (green) and the posterior muscle (red) components. The distal aponeurosis is located at the boundary of the two muscle components.

6.2 MUSCLE MATERIAL

The muscle material was assigned separately to the anterior and posterior components. This allows for a separate fiber direction to model the bipennate nature of the human TA muscle. The fibers of the human TA span from the distal aponeurosis to the anterior and posterior aponeuroses, leading to a general fiber pennation angle of 5° away from the central axis. The solid component of the muscle constitutive model was a mixture of a coupled Mooney-Rivlin

matrix and fibers with an exponential power law. An approximation of the bulk modulus is needed in this case because the biphasic (fluid + solid) nature of the material means that the standard elastic definition of bulk modulus (pressure divided by volumetric strain) does not apply. Three sets of orthogonal fibers are used to give the material both longitudinal and transverse stiffness. The fiber angles are defined using spherical coordinates. Anterior muscle fibers point 5° in the anterior direction from the longitudinal axis, and posterior muscle fibers equidistant in the posterior direction. Transverse fibers compose the corresponding two orthogonal directions to each. Because the fibers are seen as directionless, their orientation is irrelevant as the longitudinal fibers are aligned properly and all three sets are orthogonal.

The viscoelastic nature of the muscle material is modeled using a 3-term Prony Series with viscoelastic coefficients of g_1=1.589kPa, g_2=0.3769kPa, and g_3=0.6729kPa and time constants of τ_1=0.5s, τ_2=5s and τ_3=50s. Finally, the poroelastic model component was input with a solid volume fraction of 0.2, or 20%. The hydraulic permeability was set at 0.074 $mm^4/mN \cdot s$. All of these parameters were determined experimentally from tissue sample testing or empirically within FEM simulations of lapine tissue.

6.3 APONEUROSIS MATERIAL

The aponeurosis material is modeled as only being viscoelastic (not biphasic), likely due to its nature as a fibrous connective tissue. The elastic nature of the aponeuroses is modeled with a transversely isotropic Mooney-Rivlin material. The bulk modulus approximation is 10000kPa, and the fibers are oriented in the longitudinal direction of the material, or the Z-axis. The viscoelastic component again uses a 3-term Prony Series with viscoelastic coefficients of g_1=.203kPa, g_2=0.133kPa, and g_3=0.191Pa and time constants of τ_1=0.33s, τ_2=47.5s and τ_3=2500s.

Although FEBio does not use the physical bulk modulus because of the biphasic nature of the model, it can still be used to compare between the muscle material and aponeurosis to see that

they differ greatly in stiffness. In practice, the aponeurosis was designed to be approximately 5 times stiffer than the muscle material to reflect the fibrous nature of the connective tissue.

6.4 MESH GOALS

It is important to note that the goal of the FEM simulations was to keep the mesh geometry as close as possible to that of Jensen's mesh from her passive lengthening experiments. Adjustments would add in further uncontrolled variables to the simulations, thus lowering the significance of the results. Therefore, the original mesh was created to mimic Jensen's exactly. The anterior and posterior aponeuroses were added around the exterior of their respective muscle components. These aponeuroses wrap 80-90% of the way around the muscle so as to not completely encircle the mesh and join the distal aponeurosis. They extend from the proximal tip of the mesh to about 2/3 of the longitudinal length, a decision which was based on findings from the human TA cadaveric study [6]. Similarly, the distal aponeurosis bisects the anterior and posterior muscle components and runs proximally from the distal tip of the mesh to approximately 2/3 of the longitudinal length. A simplified mesh showing only the aponeuroses can be seen below in Figure 6.2. The curved exterior of the anterior and posterior aponeuroses can be clearly seen with the planar nature of the distal aponeurosis set in between.

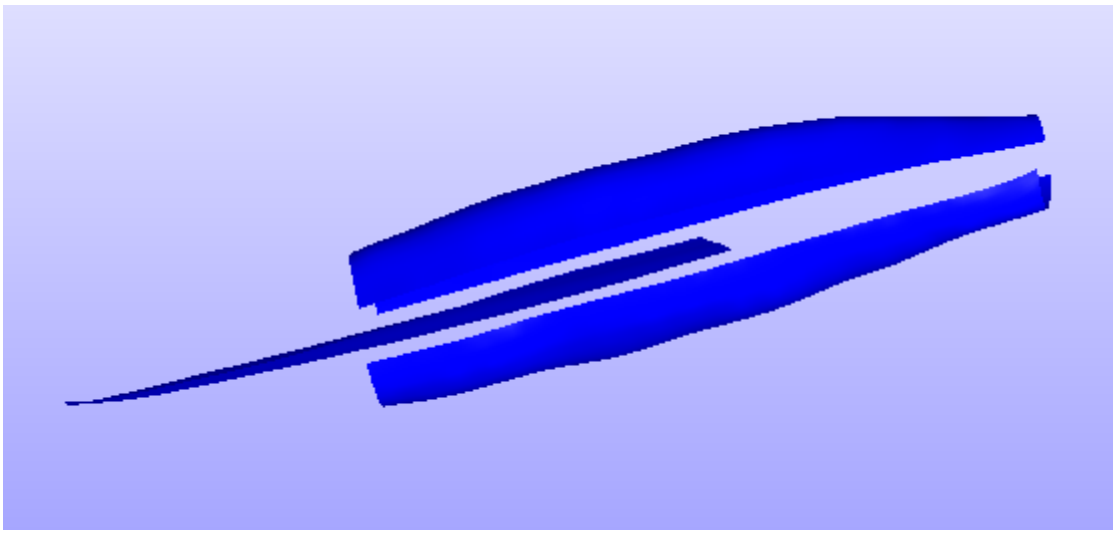

Figure 6.2: Human TA mesh screenshot with the muscle components removed. The anterior (top), distal (middle), and posterior (bottom) aponeuroses are shown.

These aponeuroses were modeled as shell elements to signify their role as connective tissue outside of the TA muscle, and also because of their relative lack of depth.

6.5 CRITICAL ASSUMPTIONS

A number of important assumptions were made to permit simulation of the human TA using FEM. First, the positioning, extent and thickness of the aponeuroses material were estimated based on previous work as well as values from literature. The anterior and posterior aponeuroses were designed to model the skin and superficial fascia, and the tibia and interosseous membrane, respectively. The distal aponeurosis models the central tendon that progresses upward through the muscle to provide the origin for the fibers. All aponeuroses were chosen to extend 2/3 of the longitudinal length of the model based on anatomical evidence [9]. This does, however, permit significant overlap of the stiffer components of the model. The thickness of the aponeuroses was assigned in PreView as 3.125mm, or 1/8", a value estimated from literature [15]. This thickness was assigned as constant in order to simplify the model. In reality, it is likely that the thickness would taper at the extremes of the aponeurosis material. The anterior and posterior aponeuroses were wrapped around 80-90% of the muscle circumference so as to apply the effects of the stiffer connective tissue to the majority of the muscle exterior, but not create a direct link between the

aponeurosis sections. By leaving a gap, this requires the muscle material to transmit the load from the anterior and posterior aponeuroses to the distal aponeurosis, just as in the physical model. The pennation angle of the human TA is known to change during muscle activity [16], but this angle was assumed constant for the extents of this study. Assigning a transient pennation angle may be beyond the abilities of the FEBio Suite at this time.

The boundary conditions applied to the muscle (described in the next section) were designed to accurately mimic the behavior of the human TA. The biphasic nature of the material was modeled as non-draining. That is, fluid could not freely exit the boundaries of the mesh during the simulation. Although the mechanism for the biphasic nature of human skeletal muscle is not yet fully understood, this non-draining assumption is believed to be valid because fluid within the skeletal muscle cannot freely traverse the body during use. This is because the TA muscle fibers, like those of other skeletal muscles within the body, are contained within an epimysium, or fibrous sheath of tissue enveloping the muscle [17].

The final set of assumptions deals with conclusions drawn from the human experiments as well as post-processing of the FEM simulations. The load cell used in Go's active contraction experiments was positioned very close to the insertion point of the human TA. Consequently, the force readings were assumed to be equal to the reaction force calculated in the active contractile FEM simulations. Similarly, the pressure sensor was positioned in the proximal belly of the TA muscle, approximately 1/3 of the length from the distal end. As such, pressure measurements taken in the active contractile FEM simulations were read from a small area of uniform length, width and height approximately 1/3 from the proximal end of the mesh. Strain slices measured in the passive lengthening FEM simulations were designed to mimic those of Jensen's experiments. Therefore, they can be assumed to provide data for a corresponding region of the mesh in both cases. Finally, both sets of experiments provide good data for small sample sizes, likely due to the time and expense required to gather human volunteers. Because of this, we do not yet know whether the data gathered is representative of the human population

as a whole. However, due to the exploratory nature of this research project this data was assumed to provide a good benchmark for beginning work with a human TA simulation.

6.6 PASSIVE LENGTHENING SIMULATIONS

The passive lengthening simulations utilized a prescribed displacement to model the stretching of the TA muscle.

6.6.1 BOUNDARY CONDITIONS

The TA muscle was constrained on both the proximal and distal faces. Combined, these two faces intersect with all five parts within the mesh. Although the only prescribed motion took place along the Z, or longitudinal, axis, the transverse behavior of the model needed to be constrained in order to keep the mesh stationary. Therefore, the nodes on the proximal face all received a "Zero displacement" constraint in the X-, Y-, and Z-directions. Attempts were made to use smaller subsets of nodes on this proximal face for the X- and Y- constraints, but these simulations did not converge.

From here, the distal nodes were assigned a prescribed displacement of 22% strain. This was done by assigning a negative Z-displacement equal to the length of the model (169.897mm) and then using a load curve within the PreView program to apply this displacement up to a fraction of 0.22 over the course of the simulation. The strain value of 22% was chosen using simple mathematical analysis of Jensen's prescribed 26° of plantarflexion, to transform the angular measurement into a linear strain. This 22% value was also chosen because it is similar to the maximum volumetric strain seen in the slices from Jensen's data.

Finally, no pressure boundary conditions were created so as to keep the mesh a closed system. This means no fluid could enter or exit the model during the simulation, similar to what is believed to occur in physical muscle during activity due to the aforementioned epimysium surrounding the muscle fibers.

6.6.2 SOLVER SETUP

A biphasic step was created to model the 2s elongation cycle of plantarflexion used in Jensen's experiments. Although Jensen reports she used multiple cycles to overlay the velocity data, only one elongation cycle was used in the FEM simulations to provide a simple approximation of the experiment. The non-linear solver in FEBio allows users to input their number of timesteps and the length of each step, the product of which is the overall length of the simulation. Therefore, 200 timesteps were used, each with a duration of 0.01s. The autostepping function within FEBio adjusts the length of the timestep in accordance with the convergence behavior of the simulation. The first step length is always the original duration (0.01s in this case), and subsequent steps may increase or decrease in length depending on how long the previous step took to converge. The maximum and minimum allowable steps were set as 0.2s and 0.001s, respectively.

6.7 ACTIVE CONTRACTILE SIMULATIONS

The active contractile simulations modeled an isometric contraction. As such, the active contraction material module was used while the proximal and distal ends of the mesh were pinned to remain stationary. This kept the length of the muscle constant through the simulation.

6.7.1 BOUNDARY CONDITIONS

The constraints on the proximal face remained the same as the passive lengthening simulations – "Zero displacement" constraints on all nodes in the X-, Y-, and Z- directions. The distal node constraints were changed to a prescribed displacement of $Z = 0$ for all nodes on the face. This approach was used rather than the "Zero displacement" style used on the proximal face because it keeps the corresponding deformation equations for the distal face in the mathematical solution instead of removing them when a "Zero displacement" constraint is used. This is important because it forces FEBio to calculate and output reaction forces on the distal face of the mesh – a crucial result for these simulations. Once again, no pressure boundary conditions were created.

Active contraction in FEBio is input in the material designation within the file itself. By creating a new module within the anterior and posterior muscle definitions, a simple version of active contraction was modeled. This contraction only required input of the fiber direction (direction of contraction) and the overall stress level T_0, or the stress generated in the muscle by the contraction. The fiber direction was assigned to follow the contractile longitudinal fibers of the muscle designations, or ±5°. The stress level was varied from 0-200kPa in order to determine the appropriate reaction force. This iterative process will be discussed further in Section 9.

6.7.2 SOLVER SETUP

A biphasic step was created to model the ramp phase of dorsiflexion used in Go's experiments. Although the experiments also had initial neutral phases as well as a final relaxation step, it is difficult to model non-contractile steps in tandem with contractile steps in the current release of FEBio. Additionally, only the ramp step is crucial to achieving the desired data comparison. Although Go conducted trials at 5%, 10% and 15% MVC/s contraction rates, only the 5% MVC/s rate was modeled in this research project. This rate was chosen because it provided the longest duration of contraction. In order to model the 10s ramp phase, 1000 timesteps were used, each with a duration of 0.01s. The maximum and minimum allowable steps were set as 1 s and 0.001s, respectively.

6.8 VARIABLES TO OUTPUT

After completing the simulation setup, a list of variables to output from each simulation was selected.

6.8.1 PRESSURE DISTRIBUTION OPTIONS

FEBio calculates both hydrostatic and fluid pressure. Hydrostatic pressure is simply the trace of the stress tensor [Tr(**S**)], or the sum of the three principal stresses. FEBio uses the Cauchy

stress tensor **S** in its calculations. As such, this calculation is mainly dependent on the deformation of the solid matrix. The program also outputs fluid pressure. There is considerable debate over whether hydrostatic, fluid pressure, or some combination of the two variables best represents IMP. Intuitively, one would believe that IMP more closely follows fluid pressure, because it is the fluid nature of the muscle that provides a pressure reading, not the deformation of the solid matrix. However, previous work has constructed FEM models whose hydrostatic pressure distribution resembles IMP [10]. Because of this uncertainty, both measures of pressure were output from each simulation to allow comparison of the values during analysis.

6.8.2 RELATIVE VOLUME

Relative volume was used to calculate the volumetric strain within the passive lengthening simulations. FEBio outputs relative volume values identical to the Jacobian of each element, or the spatial volume divided by the volume of the reference configuration, dV/dV_R. A Jacobian of greater than 1 indicates volume increase, and less than 1 indicates volume decrease. The volumetric strain in an element is equal to the change in volume divided by the volume of the reference configuration. Therefore, the volumetric strain is equal to J - 1, or 1 subtracted from the relative volume of the element.

6.8.3 REACTION FORCE

The final key output variable was reaction force for the active contractions. This variable is relatively simple. Any non-rigid constraints will induce reaction forces in the nodes that are constrained. Since a Z=0 prescribed displacement was used on the distal face of the mesh, the corresponding nodes will show reaction forces output in mN in this direction. These reaction forces can be averaged over the entire distal face within PostView, then output and multiplied by the total number of nodes on the distal face (649) to achieve the total reaction force. This force will be compared to the load cell readings from Go's active contractile experiments.

7. MESH CONVERGENCE

After setting up the simulation input, the final step before collecting data was to conduct a brief mesh convergence study. This was done to ensure the mesh density was sufficient to ensure accurate results, but not so high as to require unnecessary computational power and time. Insufficient mesh density can lead to irregularities in the FEM data, such as deformation artifacts near boundary conditions or loads. In this convergence study, the average hydrostatic pressure from the TA muscle material was output from a passive lengthening study following the protocol set forth in Section 6.

7.1 PASSIVE SIMULATIONS

A total of five unique meshes were analyzed in this study, each one with a higher density than the last. Mesh 1 is the original mesh modeled to exactly mimic that of Jensen's from her experiments. Mesh 2 adds additional elements in the transverse direction, but keeps the longitudinal number of elements constant. All subsequent meshes add elements in both the longitudinal and transverse directions. The goal of this study was to achieve a change in the average hydrostatic pressure of around or less than 1% difference between a mesh and its immediate predecessor. Midbelly longitudinal slices of the muscle were taken showing the hydrostatic pressure gradient at time t=2s for all meshes. These slices are shown below in Figures 7.1-7.5, followed by a table discussing the overall statistics from each mesh. All meshes are arranged with the distal end on the left, and the pressure gradients range from +15 to -50kPa, as shown in the color map at the right.

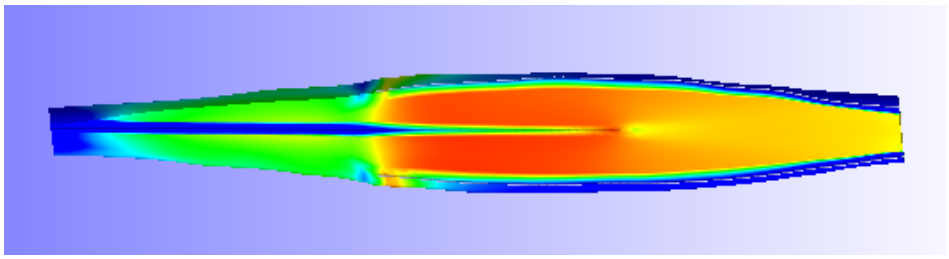

Figure 7.1: Midbelly slice of pressure distribution for Mesh 1.

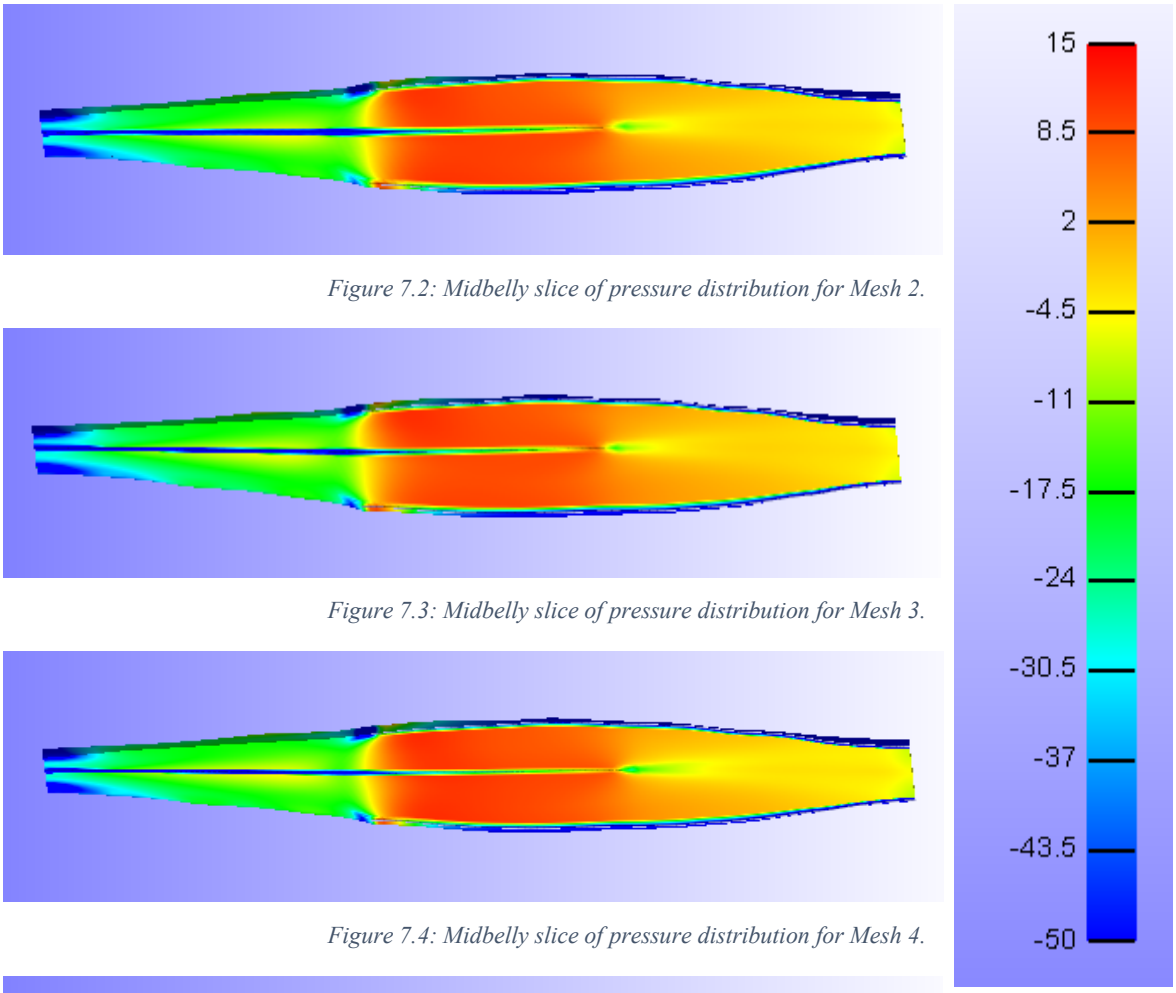

Figure 7.2: Midbelly slice of pressure distribution for Mesh 2.

Figure 7.3: Midbelly slice of pressure distribution for Mesh 3.

Figure 7.4: Midbelly slice of pressure distribution for Mesh 4.

Figure 7.5: Midbelly slice of pressure distribution for Mesh 5.

As seen above, the pressure distributions for Meshes 2-5 seem virtually identical. All of these contours feature a positive pressure (compression) region of muscle beneath the exterior aponeuroses in red-orange, and a negative pressure (tension) region in the distal region of the muscle in green. Elements that directly border the aponeuroses typically show lower pressures than their surroundings. The meaning of this pressure distribution is not important for the purposes of the mesh convergence study, but we must reach a point where a denser mesh brings no new information. To quantify the convergence of the mesh, the hydrostatic pressures for the muscle regions were output as weighted averages of all elements. These pressure readings are discussed below in Table 7.1.

Table 7.1: Mesh Convergence Statistics

Mesh #	Elements	Average Hydrostatic Pressure (kPa)	% Change from Previous*
1	12734	-1.691	N/A
2	23460	-2.126	25.72%
3*	37518	-2.041	-4.00%
4	55778	-2.217	4.28%
5	95114	-2.190	-1.22%

Although the pressure gradient appears identical from Mesh 2 onward, the table shows that the average pressure across the entire mesh still changes significantly until the transition from Mesh 4 to Mesh 5. There, a difference of only 1.22% indicates adequate mesh convergence for the purposes of this research project. Therefore, Mesh 5 was used for all simulations discussed in Sections 8 and 9. It should be noted that the drop in pressure seen in Mesh 3 likely corresponds to a disparity in the number of elements in the anterior and posterior muscle components induced by an odd number of transverse elements. The slight imbalance in the muscle halves can be seen in Figure 7.3. Because of this, the previously symmetric muscle components (in terms of number of elements) became unbalanced. The pressure reading from Mesh 4 seems to follow that of Mesh 2 more closely, and consequently Mesh 5 does as well. Therefore, the minor fluctuation in the convergence pattern seen in Mesh 3 was disregarded. The percent change for Mesh 4 was calculated from Mesh 2, not Mesh 3.

8. PASSIVE SIMULATIONS

A passive lengthening FEM simulation was conducted in accordance with the protocol outlined in Section 6. Following the completion of this simulation, the output file was analyzed in PostView to gather slice data in a manner mimicking that of Jensen in her *in vivo* experiments. The t = 2s timestep was used to gather slice data. The relative volume, hydrostatic pressure and fluid pressure were averaged across the elements in each slice and exported from PostView. The data was then compiled and displayed in the sections below for discussion and further analysis.

8.1 INITIAL DATA AND TRENDS

Figure 8.1A-D below shows an exterior view of the model at the final timestep, t=2s, for the relative volume (Jacobian) output. This figure shows quite an array of variation in volumetric strain.

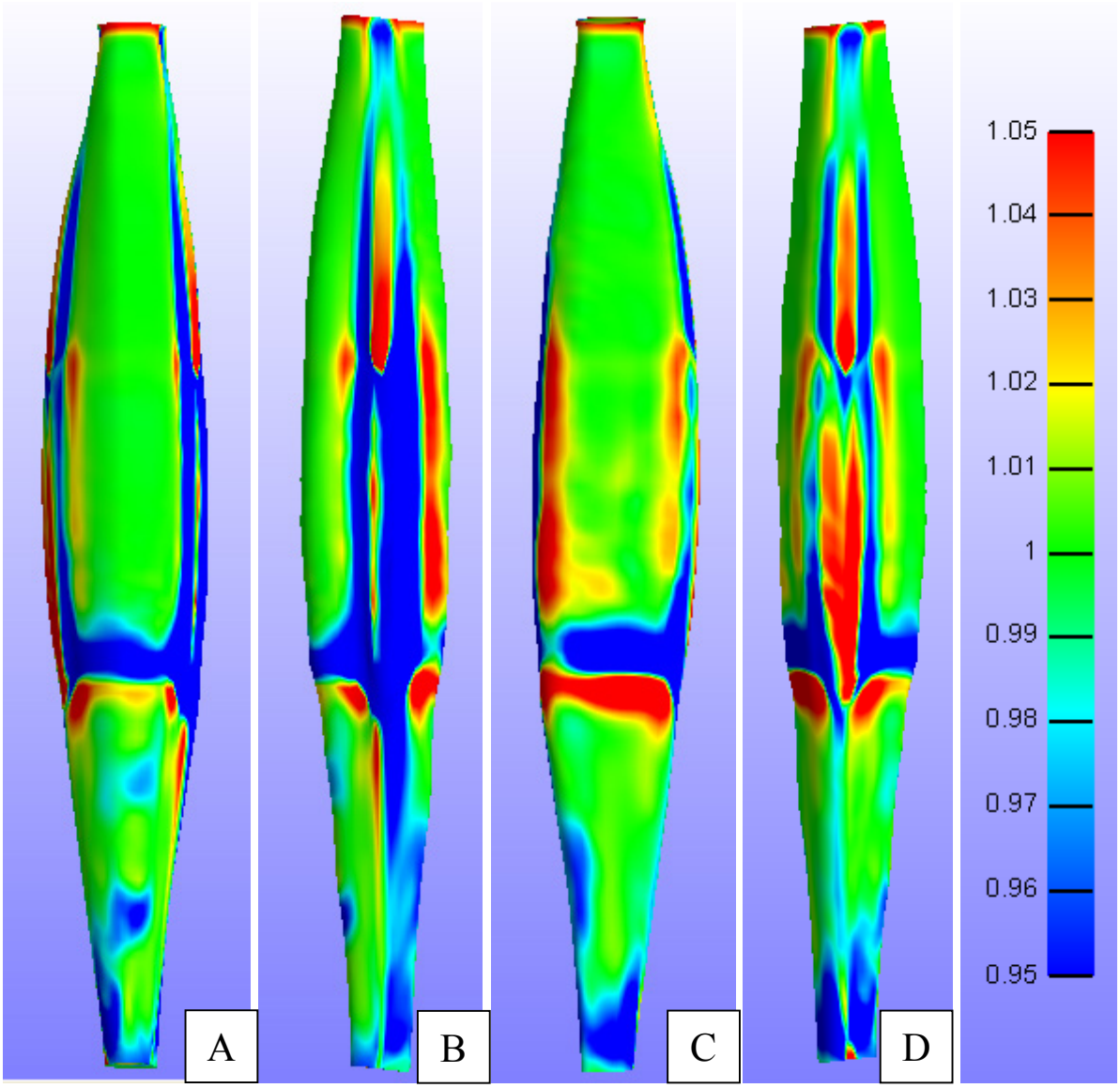

Figure 8.1A-D: Exterior views of the relative volume distribution. The views are from the (A) Anterior, (B) Medial, (C) Posterior and (D) Lateral directions.

The figures above illustrate the non-uniform strain distribution seen in the passive lengthening simulations. Green areas indicate little to no volumetric strain in any direction; this color dominates regions of the mesh away from boundaries in the model or between material designations. There is significant negative or compressive volumetric strain seen (blue), especially in the posterior and medial regions. The large region of compressive strain seen in Figure 8.1B corresponds to the mesh region between the anterior and posterior aponeuroses

along the exterior. There are a number of reasons for this strain, but perhaps the most likely is that there is likely a shearing effect seen as the stiff distal aponeurosis pulls softer muscle tissue while the stiff anterior and posterior aponeuroses attempt to hold the tissue in place at the other extreme. This could lead to some shearing or skewing of the elements between these interfaces as the sides are pulled in opposite directions. On the other hand, positive or expansive volumetric strain is seen on the lateral side of the mesh in the corresponding region. This is interesting as it shows the opposite effect of the elements on the medial side. Further investigation via the mesh slice partitions should provide more insight. Regardless, the strain on the tissue seems much more uniform on the exterior than that seen in Jensen's data. Additionally, significant areas of compressive volumetric strain are seen, whereas Jensen's slices did not report any negative strain on average.

From here, the interior of the mesh was analyzed from a qualitative standpoint. The distribution seen in the midbelly slices is much more uniform than that seen on the exterior, which suggests that the distribution is relatively constant on the interior. Therefore, only one viewpoint was analyzed as it provided representative visual data to the entire model. This viewpoint was from the medial side of the mesh, effectively bisecting all five parts of the mesh in a plane perpendicular to the Y-axis. This was done to provide the best vantage for how the aponeuroses and muscle regions interacted. In this viewpoint, the model is oriented such that the proximal end of the muscle is on the right, and distal end on the left. The anterior portion of the muscle is positioned on the bottom, with the posterior portion on the top. A relative volume distribution from this viewpoint is shown below in Figure 8.2.

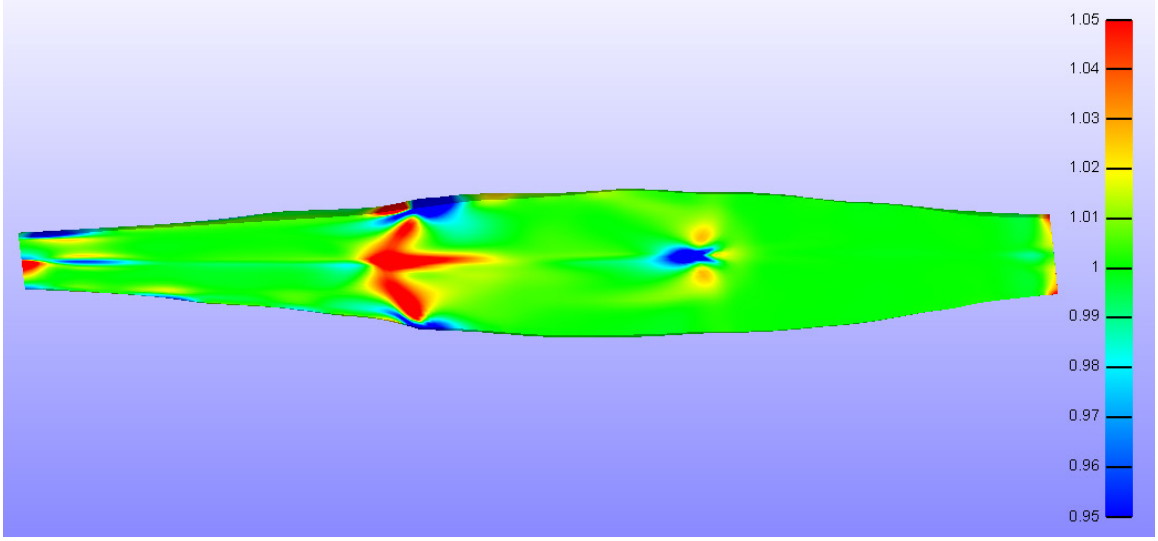

Figure 8.2: Midbelly slice of the relative volume distribution.

As seen above, the volumetric strain distribution on the interior of the model is much more uniform than on the exterior. High strain regions (>5%) are seen near the junction between the anterior/posterior aponeuroses and the distal muscle region. However, compressive can be seen on the exterior border of this junction. This indicates that the interior muscle tissue is undergoing greater volumetric strain, perhaps because it is more in line with the axis of deformation. Some other areas of positive strain are seen in the extreme distal region, which could indicate a possible correlation with Jensen's data.

After completing qualitative analysis of the volumetric strain distribution, the various pressure outputs were also examined. The hydrostatic and fluid pressure distributions are shown below in Figure 8.3 and 8.4, respectively.

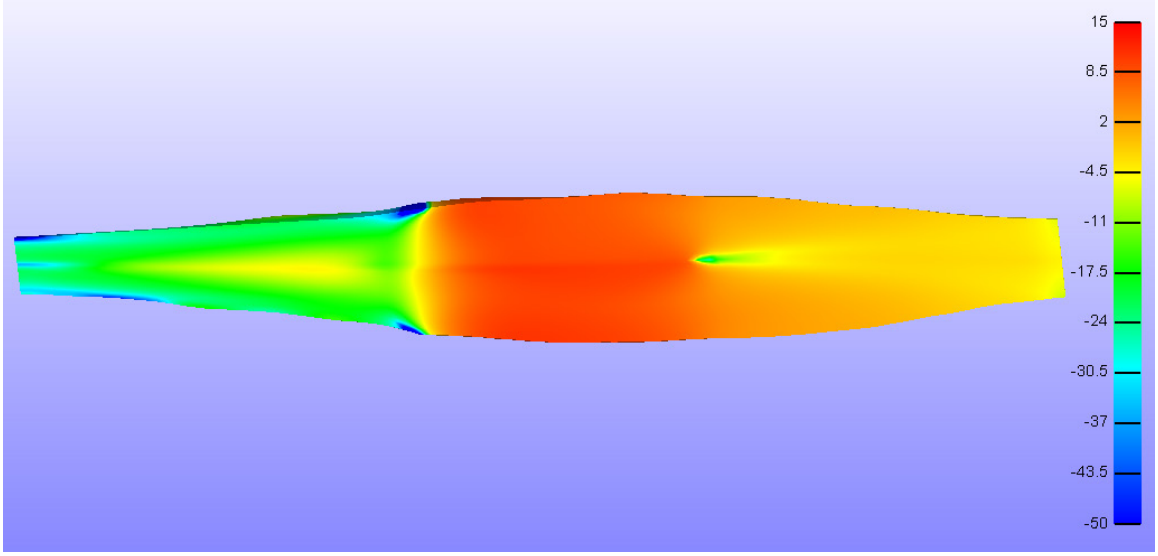

Figure 8.3: Midbelly slice of the hydrostatic pressure distribution (kPa)

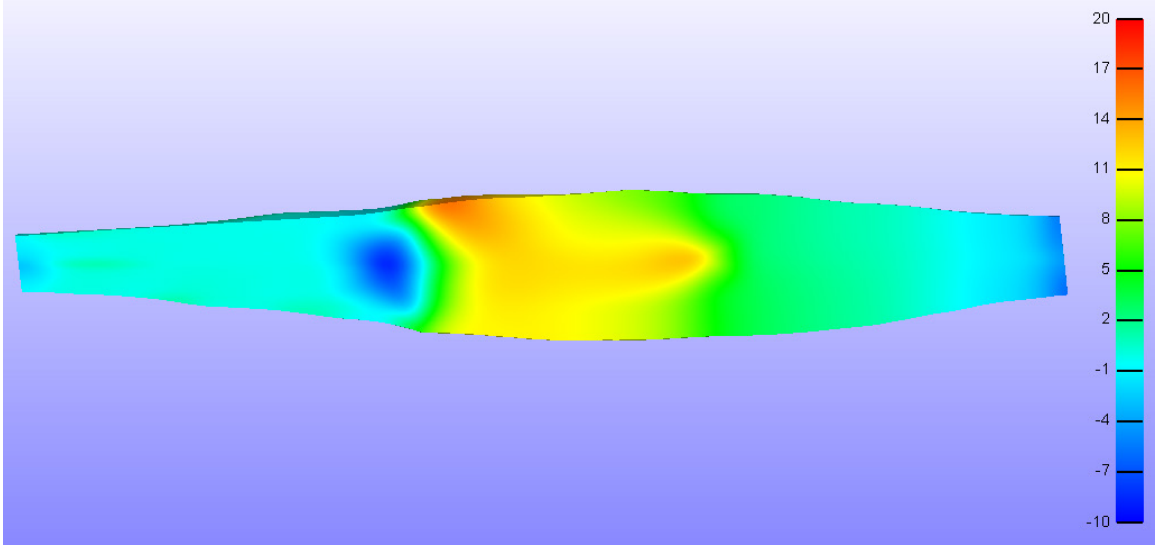

Figure 8.4: Midbelly slice of the fluid pressure distribution (kPa)

These two figures look markedly similar, with peak pressures around 15kPa located in the central belly of the muscle where the aponeuroses overlap. Interestingly, there is significant positive pressure seen in the hydrostatic pressure contour, which corresponds to compressive stresses. One would imagine that in a simulation that stretches the model longitudinally, there would be little compressive stress seen. Also interesting to note is the abrupt change from positive to negative pressure at the transverse border of the anterior/posterior aponeuroses and the distal muscle region of the model. This is the same location as the peak volumetric strains,

which indicates that the boundary of the compressive and expansive stresses is likely to be the source of the peak volumetric strain in the model. This is a different location than the peak strain in Jensen's model seen at the distal tip of the muscle, but this region is still more distal than the majority of the mesh. In short, this suggests that the aponeuroses have a far greater effect on the model behavior than the location within the mesh, among other factors.

To further examine this potential theory, the principal stresses were output in three contours created in Figures 8.5-8.7 below.

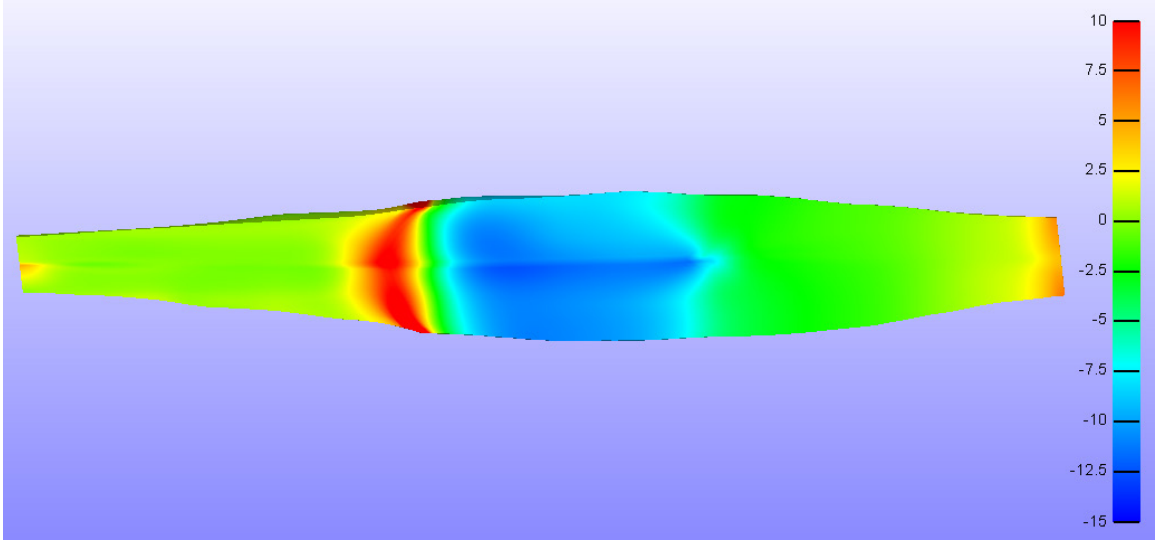

Figure 8.5: Midbelly X-Cauchy stress distribution (kPa)

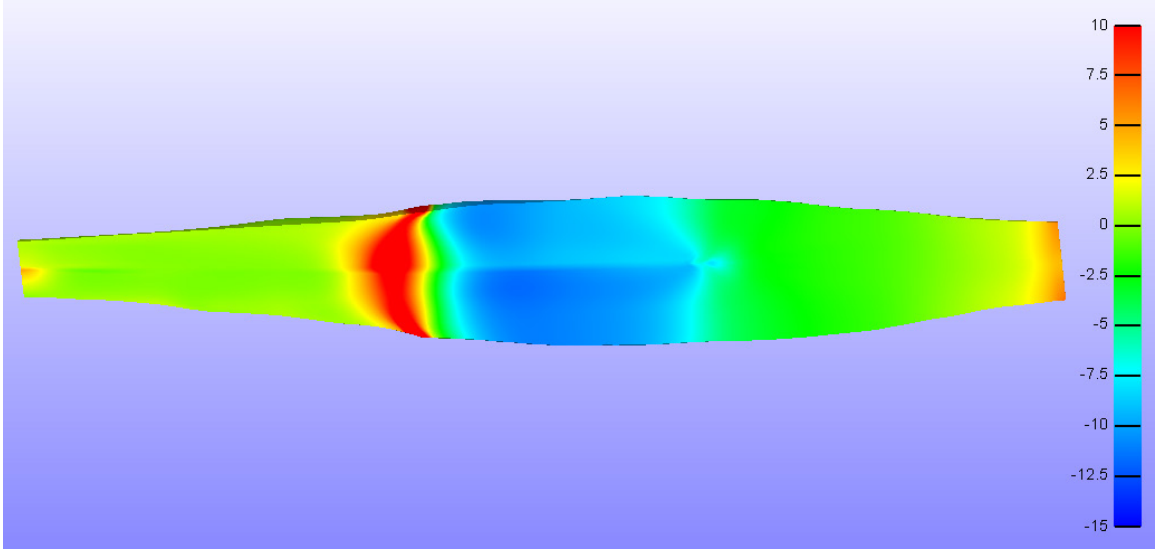

Figure 8.6: Midbelly Y-Cauchy stress distribution (kPa)

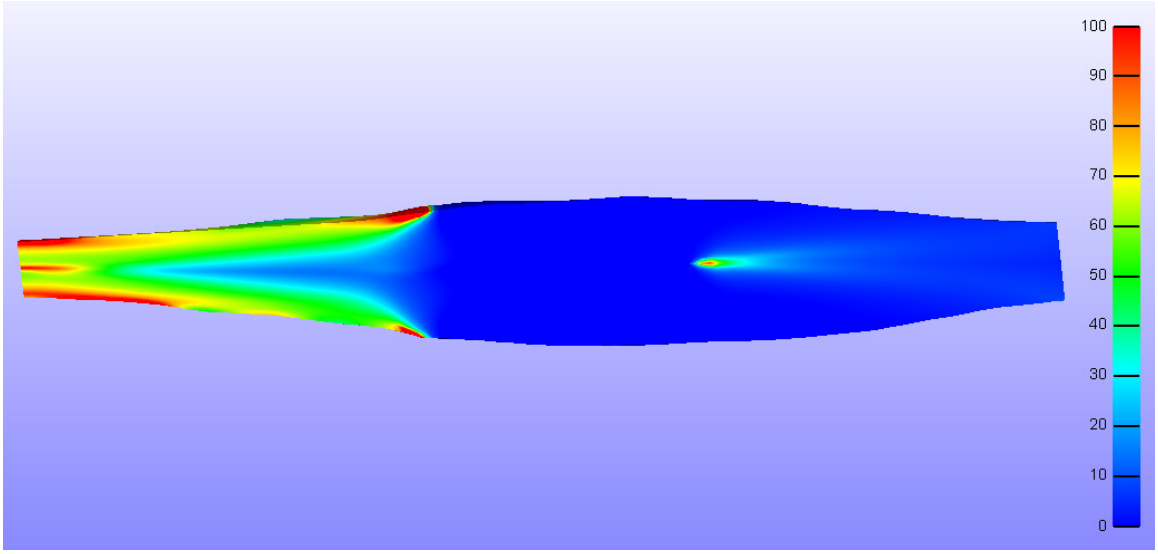

Figure 8.7: Midbelly Z-Cauchy stress distribution (kPa)

The X- and Y- stress distributions are virtually identical, with compressive stress seen in the same regions as the compressive pressures, and maximum stresses seen at the distal junction of the anterior/posterior aponeuroses and the muscle. However, the Z-stress distribution illustrates the differences in strength between the aponeuroses and the muscle tissue. The gradient expanding outward from the distal face, then vanishing at the distal boundary of the exterior aponeuroses indicates that the vast majority of the stresses are carried by the aponeurosis tissue. The three aponeuroses in this model essentially operate in parallel, and so the muscle only serves

as a medium to transmit the load between them. As such, relatively little stress is seen in the proximal 2/3 of the muscle as, under the strains seen, it carries negligible load compared to the aponeuroses. A plot of the scalar Von Mises stress distribution is shown below in Figure 8.8.

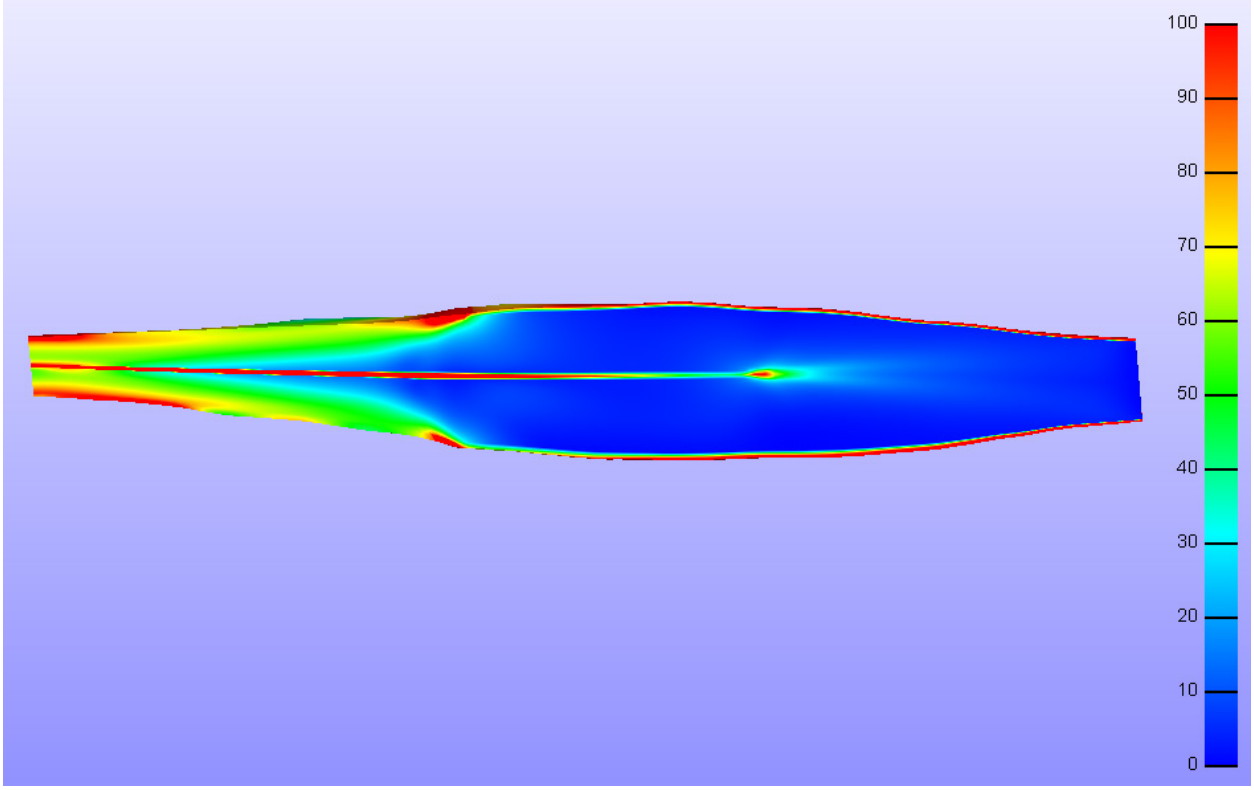

Figure 8.8: Von Mises stress distribution (kPa)

This distribution appears very similar to that of Figure 8.7. However, higher stress regions can be seen along the three aponeurosis cross-sections running horizontally across the figure. This indicates that the aponeuroses are under significant stress, while the belly of the muscle remains relatively unstressed. There is a small portion of muscle with stresses in the 20-50kPa range just proximal to the end of the distal aponeurosis within the muscle tissue, but this stress quickly dissipates. The bands of muscle tissue on both sides of the distal aponeurosis have stresses around 50-70kPa.

To confirm these theories, a contour plot of the Z-displacements in the model is shown below in Figure 8.9.

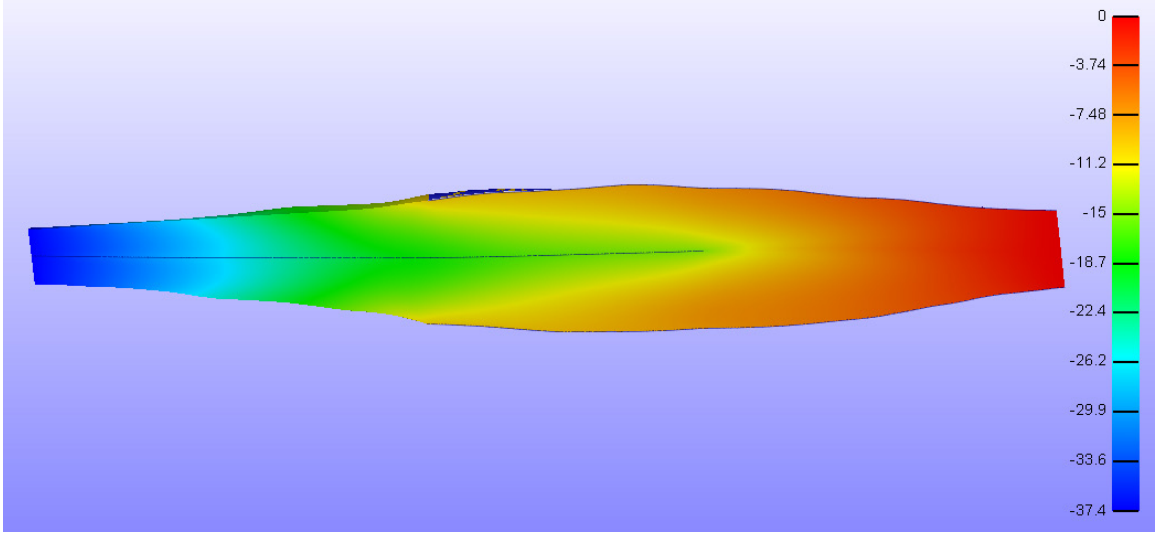

Figure 8.9: Midbelly slice of the Z-displacement distribution

This plot supports the claim that the muscle is supporting little force on its own. There is a sharp change in the displacement seen between the exterior and internal aponeuroses. This diagonal continuum of displacement around the proximal portion of the distal aponeurosis may explain the compressive pressures seen previously, as the muscle tissue is undergoing some relaxation in the regions between the interior (distal) aponeuroses and the exterior layers. The muscle is not elongating in the longitudinal direction in this region, but is being constrained transversely by the aponeuroses that are narrowing as they sustain the load induced by the displacement. This explains the volume reduction seen in this region in the relative volume plots shown previously.

8.2 QUANTITATIVE RESULTS / PLOTS

Plots similar to those found in Jensen's work were developed and are shown below in Figures 8.10-8.11. Volumetric strain plots are shown for both the posterior-anterior and medial-slices with subsequent discussion.

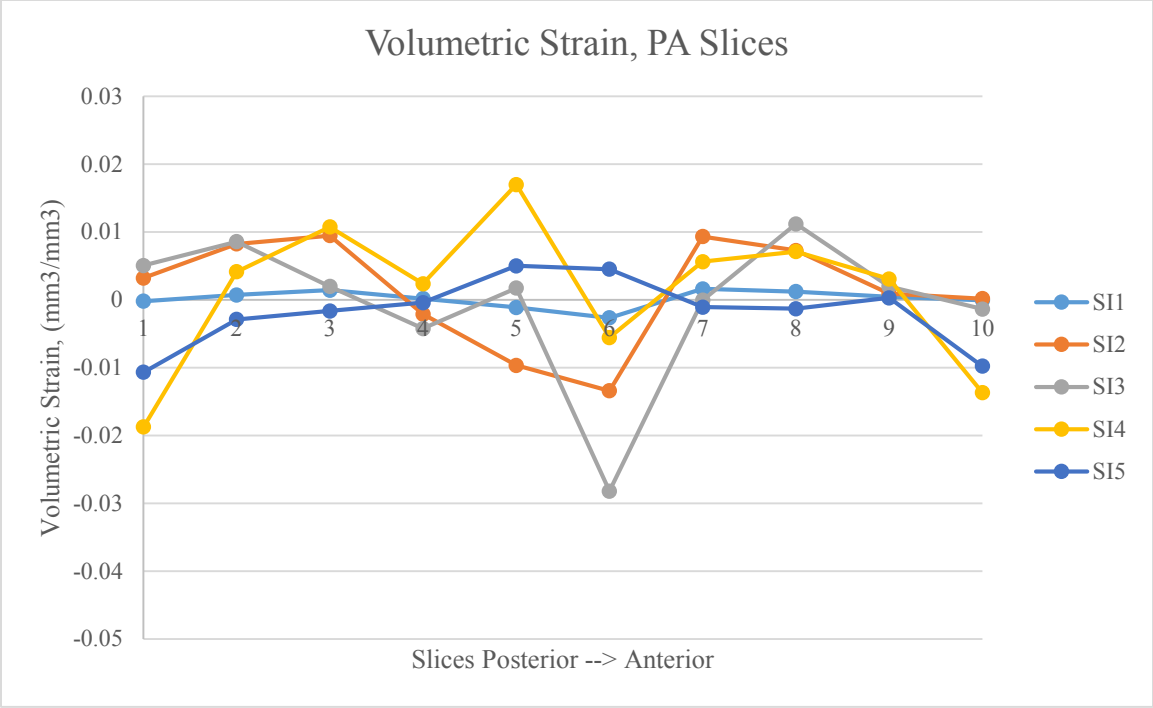

Figure 8.10: Volumetric strain plot for posterior-anterior mesh slices.

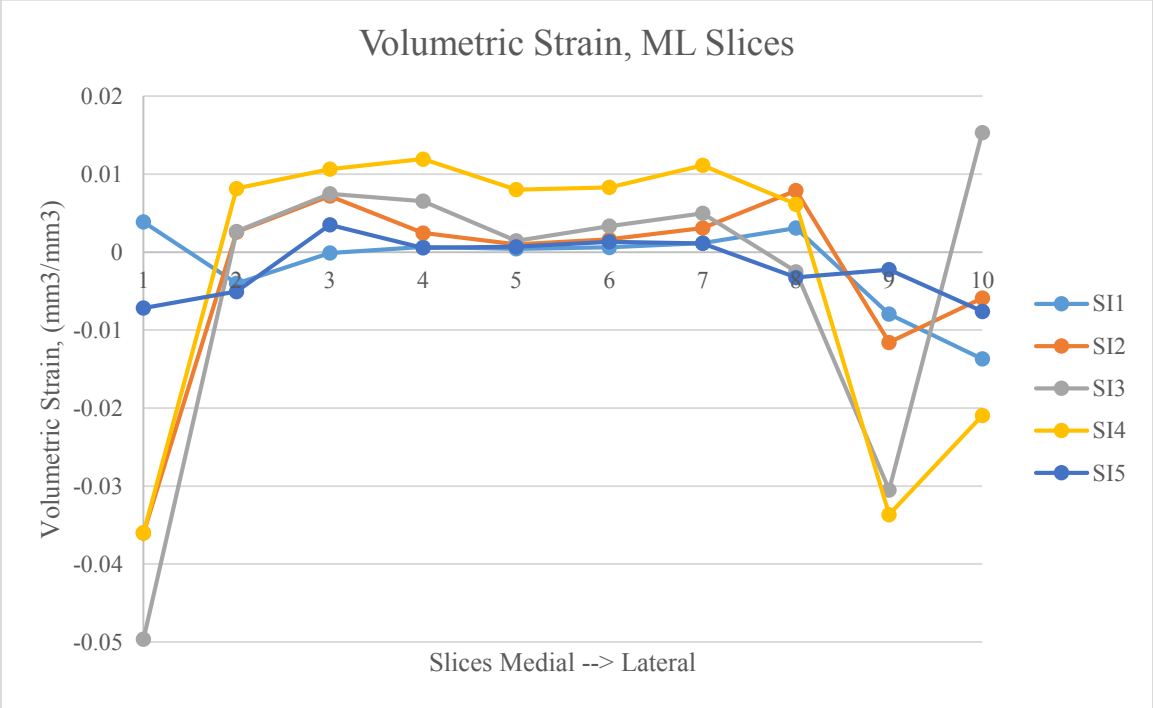

Figure 8.11: Volumetric strain plot for medial-lateral mesh slices.

The strain plots above have some minor correlations to those from Jensen's experiments, but there are also many differences seen. First, Jensen saw the maximum strain in each direction in her most distal slice, SI5. In the simulation data this slice has the strain closest to zero. Jensen's baseline volumetric strain values were between 2-4%, while the strains in the FEM simulations were between 0-2% on average. Additionally, a significant number of slices showed reduction in volume, specifically in the extreme medial and lateral slices of SI3 and SI4. These areas correlate to the compressive strain regions seen on the exterior of the model discussed previously. Additionally, there are some interesting fluctuations in strain seen in the intermediate posterior-anterior slices in SI2, SI3 and SI4. This can be attributed to the jump between the posterior and anterior aponeuroses on the exterior of the model, the same location as the compressive strain regions. These slices contain the most medial and lateral regions of the mesh within them.

Although there are minimal trends to be observed across the posterior-anterior spectrum, all of the 5 superior-inferior sections contain their greatest volumetric strain in a slice on the medial side of the mesh – the same trend as that seen in Jensen's data. Additionally, with the exception of SI5 all of the slices show an increasing trend in volumetric strain from proximal to distal. Together, these trends show promise in the ability of the model to more closely match the data from Jensen's experiments in the future.

The disparity between volumetric strain readings in Jensen's data versus the simulations indicates that an important aspect of the FEM model is either missing or not addressed properly. It appears the aponeuroses within the FEM model are too stiff to permit transmission of force through the muscle tissue – the aponeuroses bear the vast majority of the force induced through stretching. Additionally, transverse volume reduction in stretching may be a result of inadequately address boundary conditions, such as those imposed by the tibia and surrounding fascia. As the model becomes more complex, these boundary conditions should be addressed.

In order to properly compare the volumetric strain readings for the experimental and simulated data, the 5 series from each plot were overlaid on a single axes for each transverse direction. The resulting graphs are shown below in Figures 8.12-13. These plots illustrate the general magnitude difference between Jensen's experimental data (shown in solid lines) and the simulation data (shown in correspondingly-colored dashed lines).

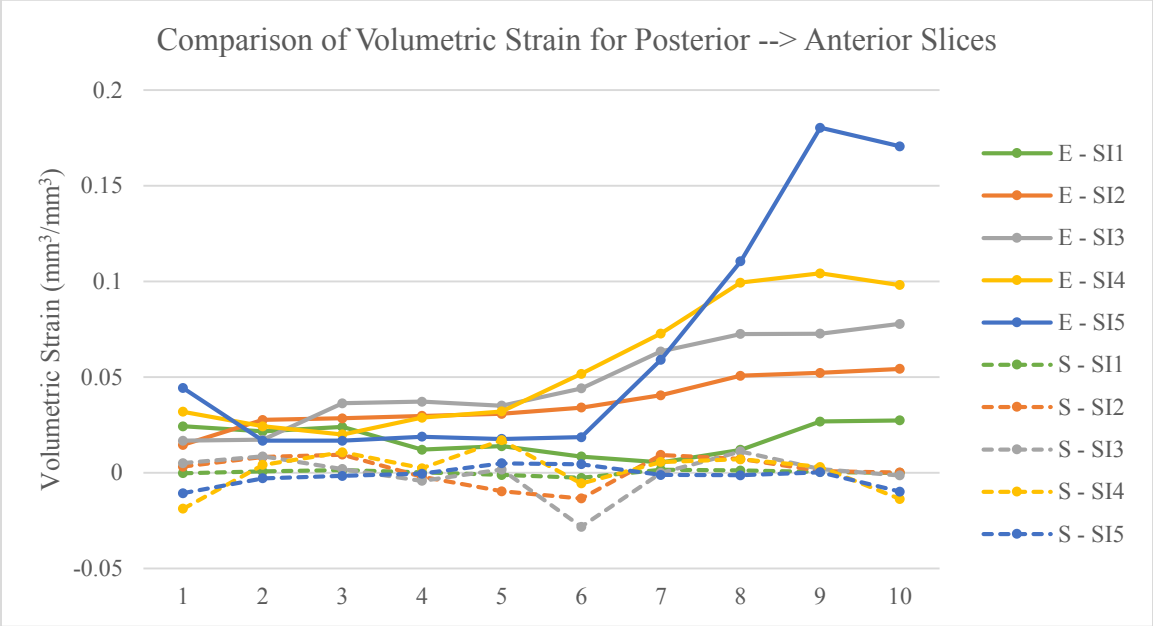

Figure 8.12: Comparison of volumetric strain data in the posterior-anterior slices. Series beginning with 'E' indicate experimental data, while 'S' indicates simulated data.

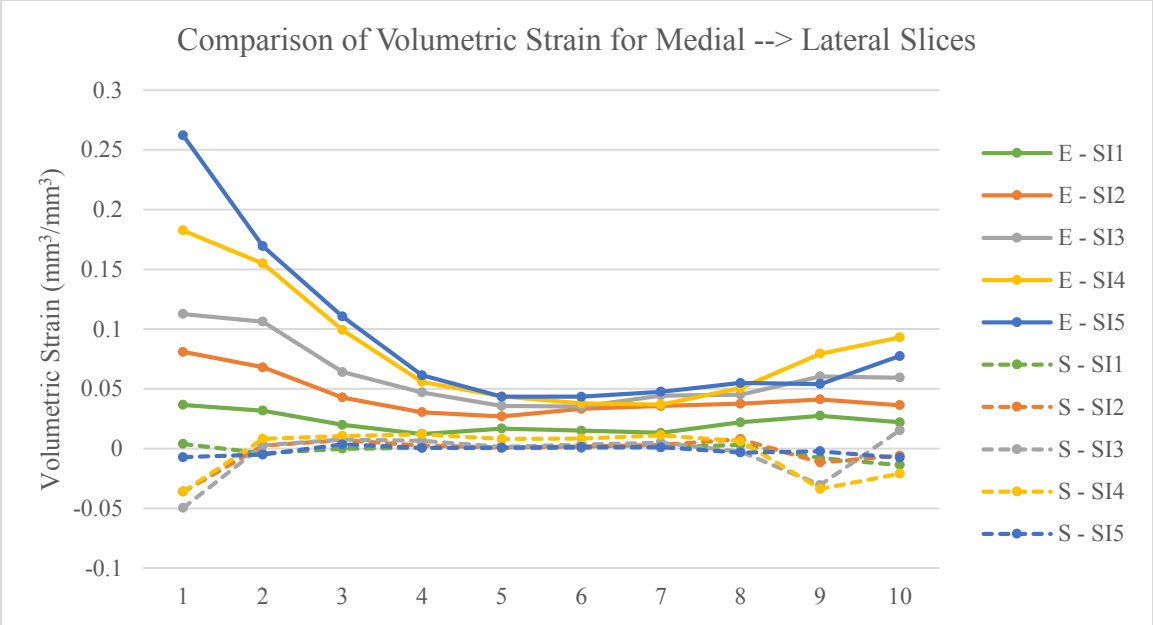

Figure 8.13: Comparison of volumetric strain data in the medial-lateral slices. Series beginning with 'E' indicate experimental data, while 'S' indicates simulated data.

8.2.1 APPROPRIATENESS OF PRESSURE READINGS

As discussed in Section 6, a debate is ongoing regarding how to interpret IMP in FEM simulations. Researchers have yet to unquestionably determine the physical mechanism for IMP recorded by pressure sensors embedded in muscle tissue. FEBio outputs both hydrostatic (stress-induced) and fluid-based pressure. Plots of both parameters over the posterior-anterior and medial-lateral slices are shown in Figures 8.14-8.15 below.

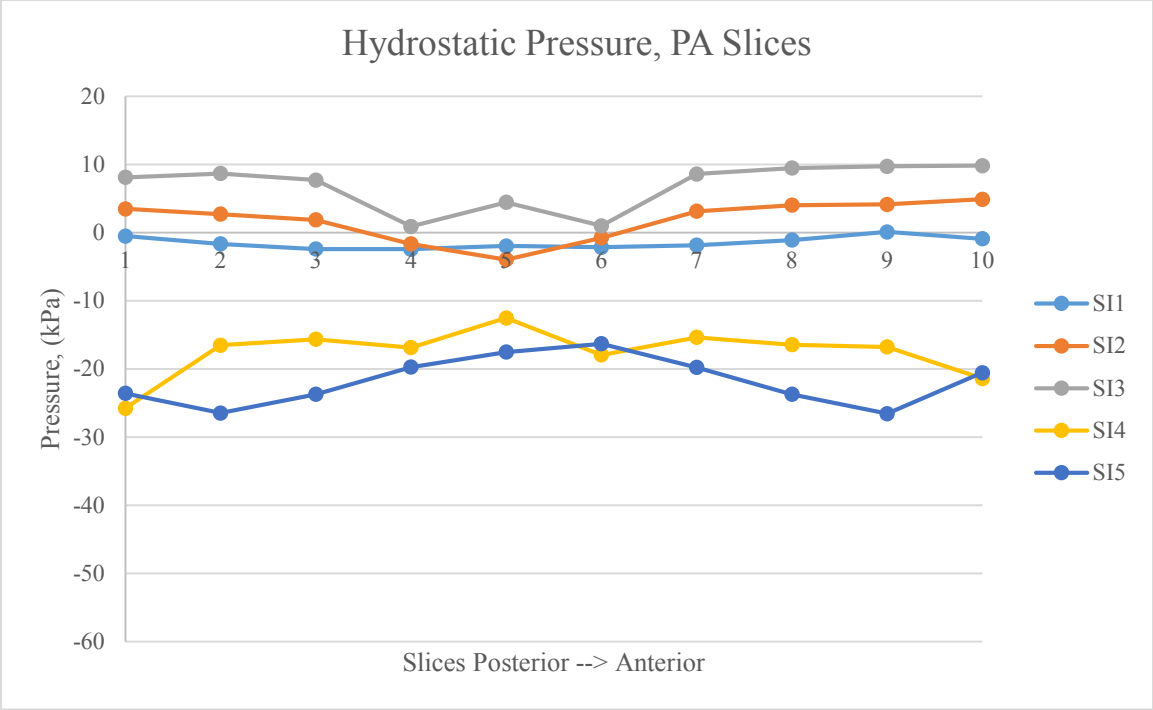

Figure 8.14: Hydrostatic pressure plot for posterior-anterior slices.

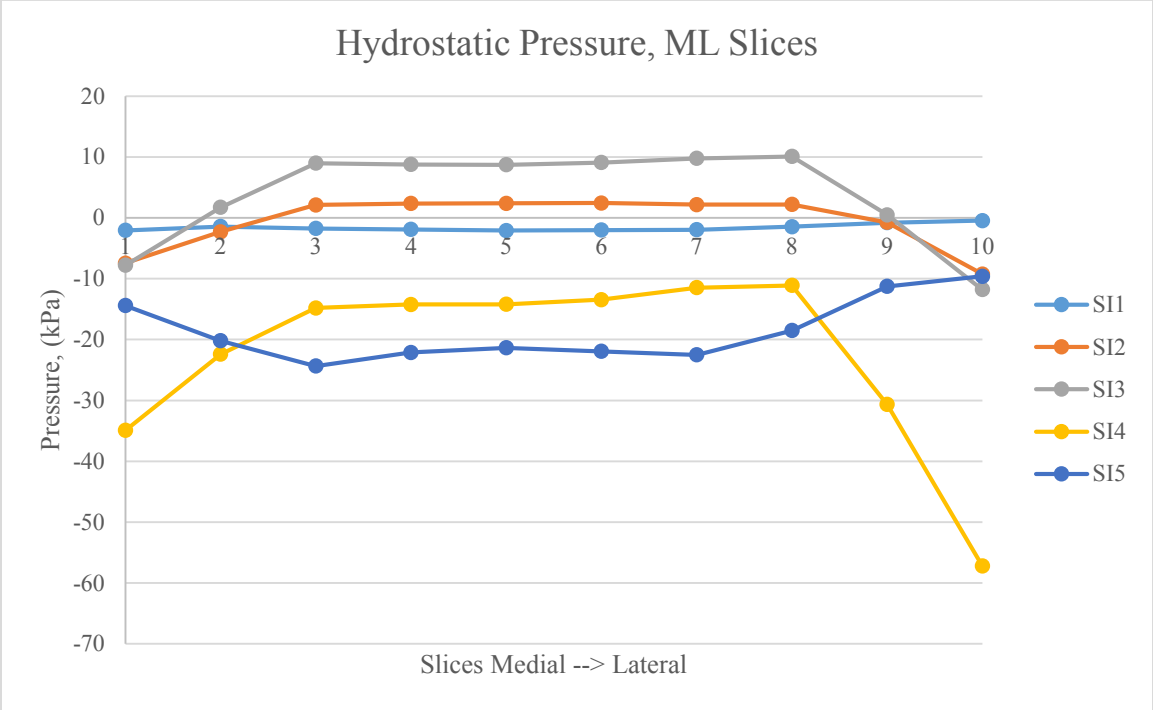

Figure 8.15: Hydrostatic pressure plot for medial-lateral slices.

The main observation from the hydrostatic pressure plots lies in the relative uniformity of the pressure across the transverse directions. There is little change in the hydrostatic pressure regions for slices 1-3 and 7-10 for SI2, SI3 and SI4 in the posterior-anterior direction. Additionally, little change is seen in slices 3-8 for all sections in the medial-lateral direction. The pressure for SI1 hovers around 0kPa for both directions. This is likely not zero actual pressure, but rather zero net pressure observed in each slice as the sum of the principal stresses. Slices SI2 and SI3 both have positive (compressive) pressures between 0-10kPa with the exception of slices 4-6 in SI2 in the posterior-anterior direction. Slices SI4 and SI5 have negative (expansive) pressures ranging from -10 to -30kPa with the exception of the two most lateral slices in SI4 where the pressure plummets to -57kPa, likely an artifact of the aponeurosis-muscle junction.

Overall, the pressure distributions show strong uniform tendencies in the FEM simulations in the transverse directions, but not in the longitudinal directions. This may indicate that longitudinal positioning of a pressure sensor is much more important than transverse positioning, as long as the sensor is placed in the belly of the muscle and not near the boundaries.

Following the completion of the hydrostatic pressure analysis, similar plots were constructed to study the fluid pressure distributions. These are shown in Figures 8.16-8.17 below.

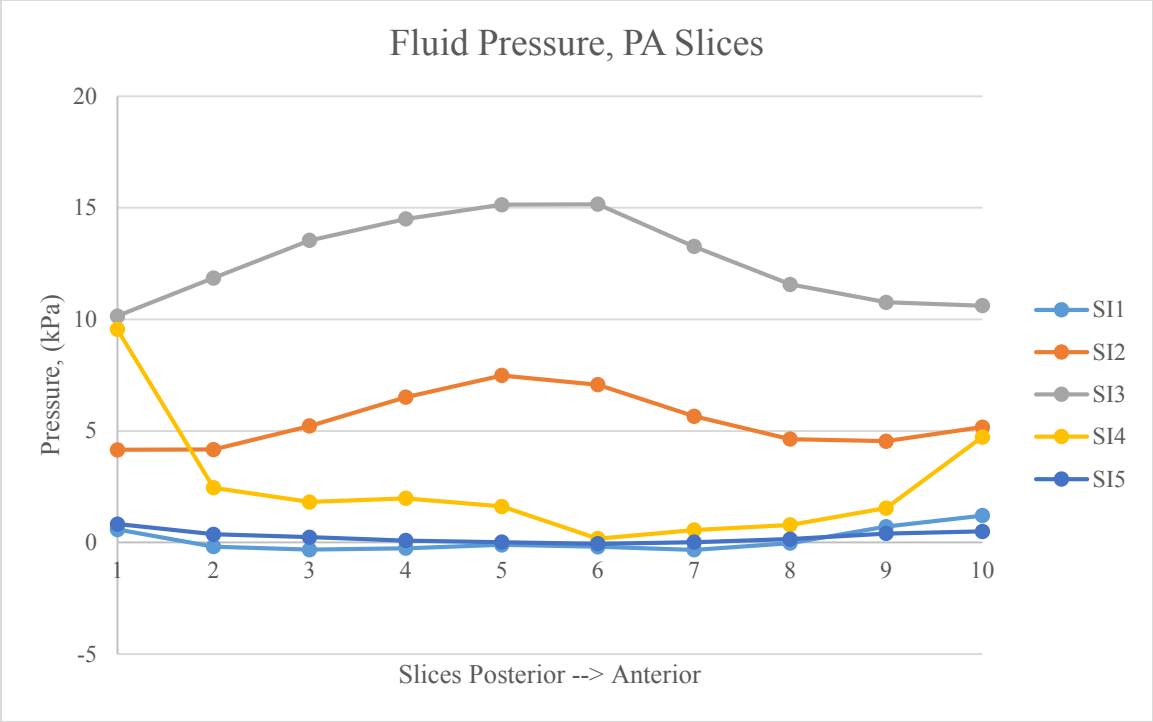

Figure 8.16: Fluid pressure plot for posterior-anterior slices

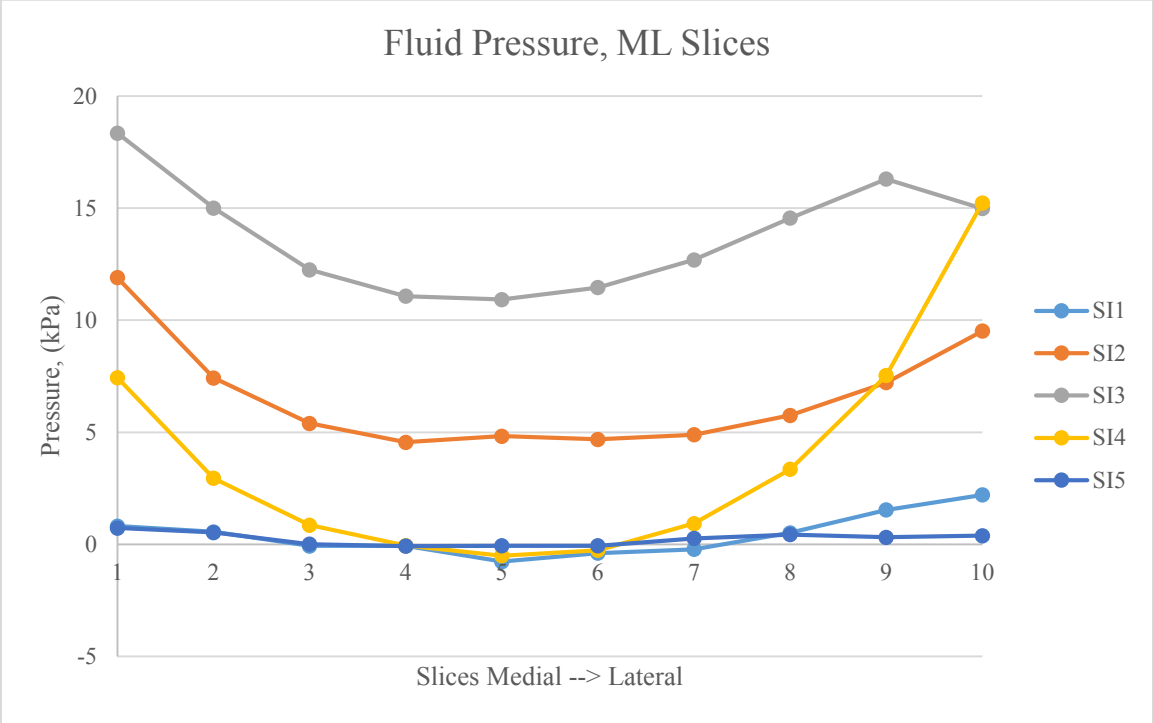

Figure 8.17: Fluid pressure plot for medial-lateral slices

The fluid pressure plots illustrate more varied distributions than those of their hydrostatic pressure counterparts. Typical fluid pressure range from 0-15kPa, with some slices dipping below zero, but never further than -1kPa. The peak fluid pressure was located in the most medial slice of SI3, at 18.3kPa. The values for fluid pressure in both the posterior-anterior and medial-lateral directions for sections SI1 and SI5 hover around zero for their entirety. This may indicate that the majority of the fluid component is located in the larger, and therefore more porous, belly of the muscle. Slices SI2 and SI3 have their maximum pressures in the center of the mesh (slices 4-6) in the anterior direction, but in the most medial slice for the other orientation. IMP is well known to be greater at deep points in the muscle or near stiffer structures such as bones or fibrous tissue. Therefore, it comes as no surprise that the fluid pressure is greater at the extremes of the tissue near the stiff aponeuroses. Jensen's volumetric strain data described an increasing trend in the medial direction. Since IMP is known to correlate directly with passive stretching of muscle tissue, the increase in IMP in the medial direction could indicate a potential correlation. Additionally, the medial-lateral plots from Jensen's data were observed to have a trough-like shape, where the lowest values were found in the center of the mesh. Each of the 5 sections seem to follow this trend in the medial-lateral fluid pressure data, showing promise that fluid pressure is a better representation of IMP for this model.

8.3 SUBSEQUENT ATTEMPTS

After uncovering the initial disparity in volumetric strain for the FEM simulations as compared to Jensen's *in vivo* data, several subsequent simulations were run to study the applicable changes in volumetric strain output and determine if the adjustments pushed the strain readings towards those found in Jensen's experiments.

8.3.1 REMOVAL OF BIPHASIC COMPONENT

First, the biphasic nature of the muscle material was removed and the remaining viscoelastic components were retained in order to make the muscle behave more similarly to the viscoelastic-modeled aponeurosis material. This was done because it would make the muscle material more

susceptible to volume changes. Figure 8.18 shows a comparison of the Jacobian gradients in the original and resulting meshes.

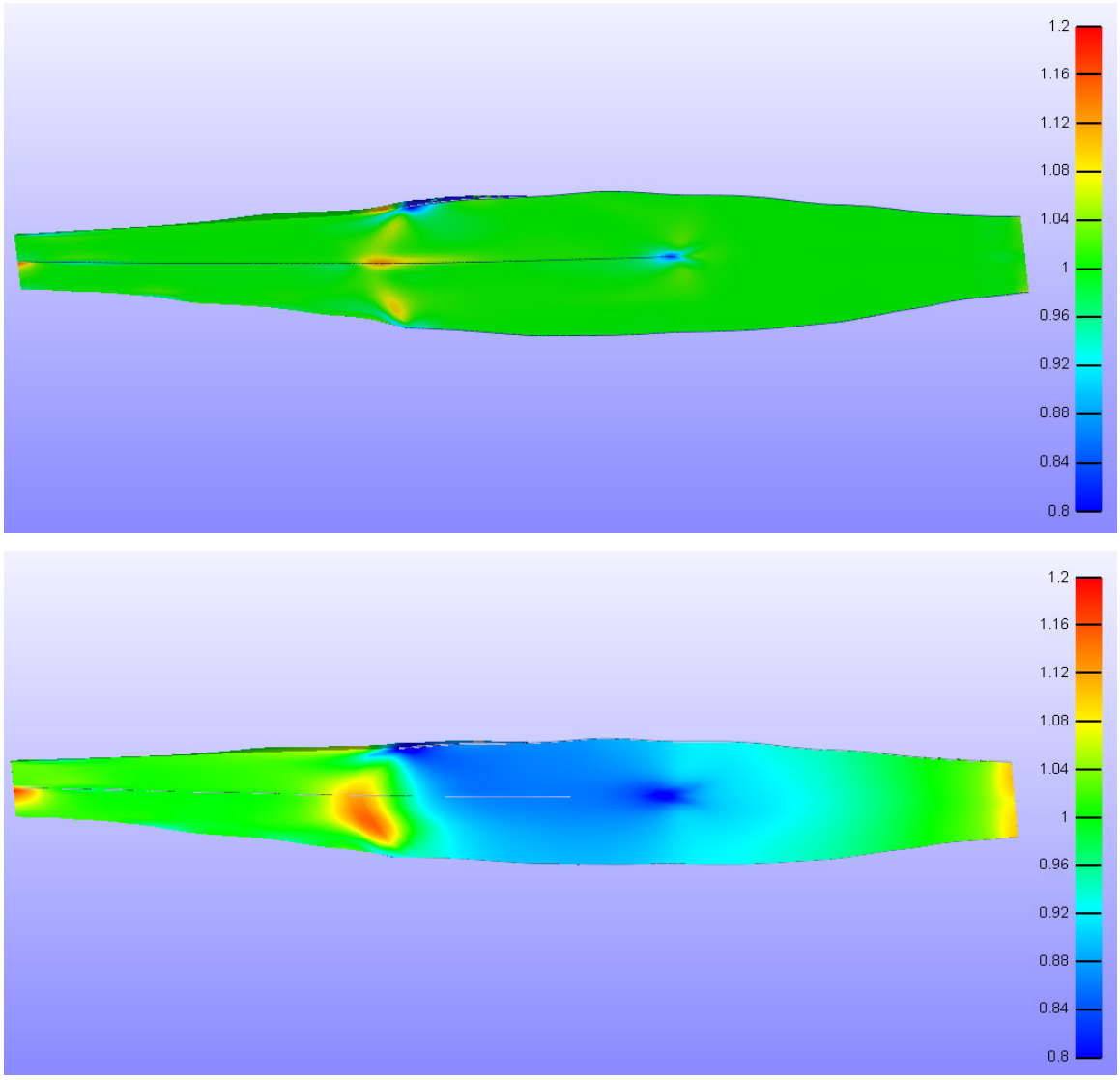

Figure 8.18: Relative volume distribution before (top) and after (bottom) removal of the biphasic (fluid) component of the mesh.

As seen above, removing the fluid component of the muscle causes significant compression in the regions between the three separate aponeurosis materials. This is because there is no longer a

force to resist compression of the material since the fluid was removed. The fibers used to give the muscle tensile strength have no action in compression, and as such only the weak Mooney-Rivlin ground matrix is left to resist the compressive transverse force seen during elongation in this region. Therefore, the fluid component clearly plays an important role in the behavior of the muscular tissue, and should be left intact.

8.3.2 BULK MODULUS

The second post-hoc adjustment made was a decrease in the bulk modulus approximation of the muscle material. This value was set arbitrarily at 5kPa during fitting to the lapine data because no recommended value could be found in literature [12]. Decreasing the bulk modulus approximation would have the effect of increasing the susceptibility of the material to changes in volume. Therefore, the value was decreased by an order of magnitude from 5 to 0.5kPa and the simulation repeated. A screenshot of the Jacobian gradient is shown below in Figure 8.19.

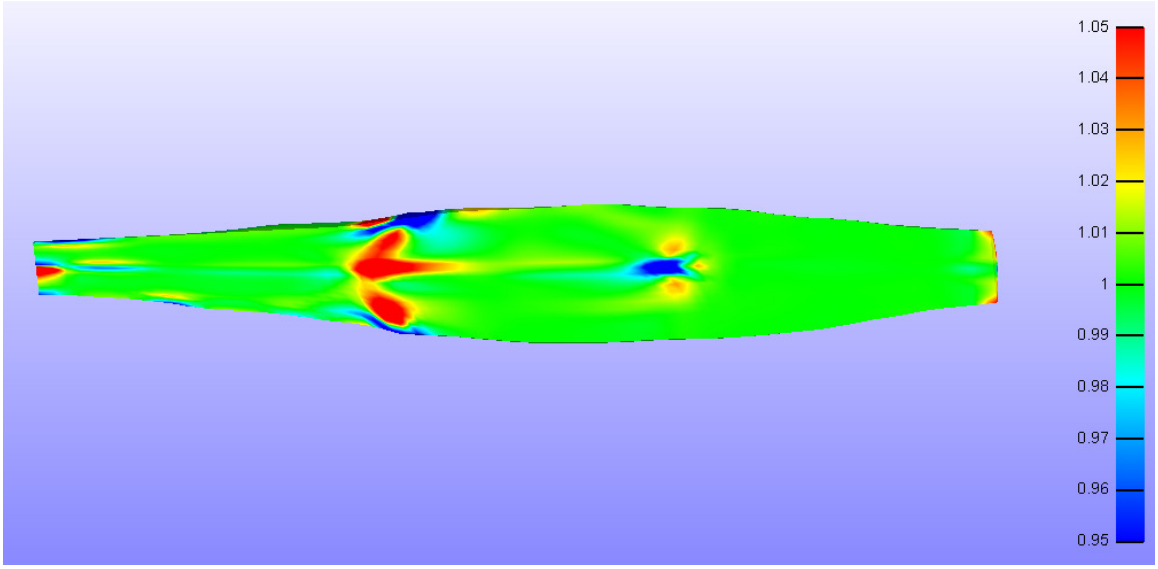

Figure 8.19: Relative volume distribution after reduction in bulk modulus approximation from 5 to 0.5kPa.

As shown, the decreased bulk modulus approximation has minimal effect on the volumetric strain seen in this longitudinal midbelly slice – this contour is almost identical to the original one shown previously. There may be slightly higher strain seen in the distal regions, but the

difference is not enough to warrant a deeper analysis at this time. While the idea to drop the bulk modulus should work in theory, this may indicate that there are other problems to be resolved with the mesh before trying this approach. This is especially true when taking into consideration that there is no basis in literature for the choice of 5kPa or 0.5kPa for this value. Iterating the bulk modulus approximation would be better done in tandem with a fitting process to acquired human TA testing data in the future.

8.3.3 QUADRATIC ELEMENTS

An attempt to address element skewing seen in the regions between the aponeuroses involved the use of second-order elements. Also referred to as quadratics, the use of second-order elements would increase the number of nodes in a standard hexahedral brick element from 8 to 20, by adding a node at the midpoint of each edge of the element. Aside from greatly increasing the accuracy and precision of the simulations, the use of quadratic elements can help reduce problems due to shear, especially when the shear-susceptible linear brick elements are used such as in this simulation. The use of quadratic elements will greatly increase the computation time of a simulation due to the increased number of nodes, but the benefits of their use in complex simulations such as this generally outweighs the additional time and expense involved.

Therefore, the linear brick elements in the muscle material were converted to second order hexahedral brick element in Abaqus. Unfortunately, the 4-noded quadrilateral shell elements could not be converted to their 8-noded quadratic counterparts because FEBio does not support second order shell elements at this time. Therefore, the linear shell elements were retained, and the simulation run again to examine the overall results.

Almost immediately, the results of the simulation were rendered invalid due to the poor interface between the stiff, linear shell elements of the aponeuroses and the more flexible, quadratic brick elements of the muscle tissue. Although the shearing behavior seen was reduced within the muscle material, the newly introduced intermediate nodes of the hexahedral elements could not interact with the quadrilateral shells, and as such they tended to pull away from the aponeurosis

shells while the original nodes remained in contact. This resulted in the “fish-scaling” effect seen below in Figure 8.20.

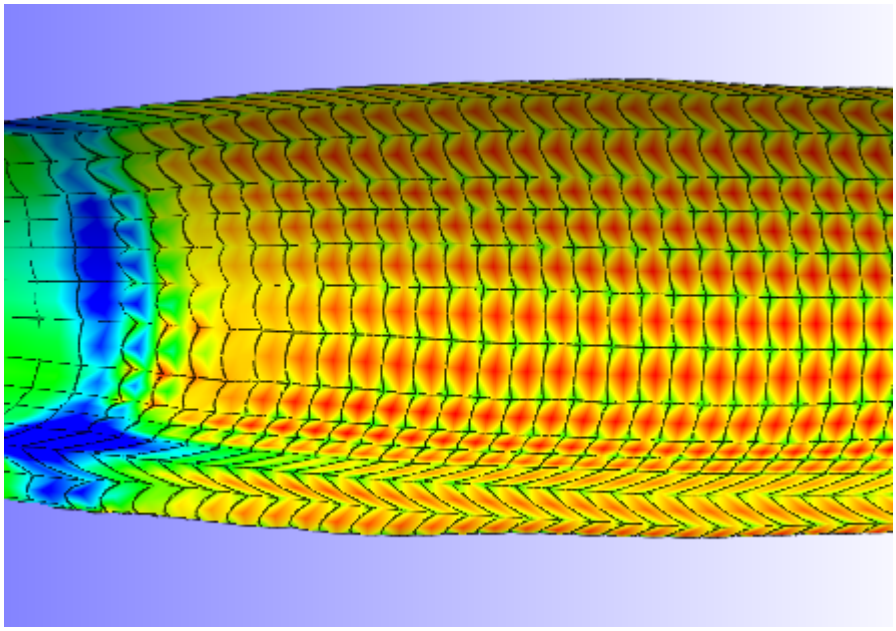

Figure 8.20: "Fish-scaling" effect seen due to the interaction of linear shells and quadratic brick elements.

This behavior is clearly unrealistic, and therefore undesirable for these FEM simulations. Therefore, the use of quadratic elements will be suspended until such time as FEBio can support the second order shell elements as well. However, it does expose just how much stiffer the aponeuroses are than the TA muscle. With linear elements, the muscle elements bordering the aponeuroses are rendered virtually immobile, which may explain the low pressure regions seen.

8.3.4 DECREASED APONEUROSIS THICKNESS

The final post-hoc adjustment made to the passive lengthening model was a drop in the aponeurosis thickness. It is believed that having the muscle and aponeuroses materials closer in overall stiffness would result in a better distribution of the volumetric strain and a reduction in the compressive behavior seen in the model. Therefore, the thickness of the aponeurosis shell

elements was dropped from 3.125mm to 1mm. The resulting Jacobian gradient is shown below in Figure 8.21.

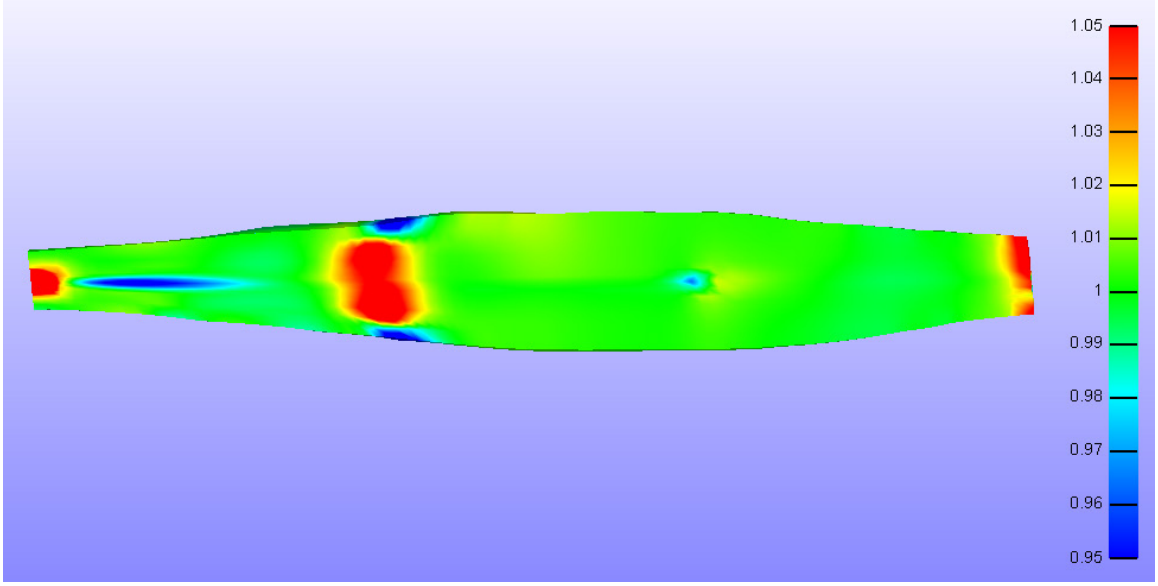

Figure 8.21: Relative volume distribution after reduction in aponeurosis thickness to 1mm.

The decreased thickness of the aponeuroses does not seem to greatly affect the strain distribution. In fact, it actually serves to make the distribution more homogeneous in the previously fluctuating strain areas. This loss of non-uniformity seen in previous simulations is a major drawback. Getting a non-uniform volumetric strain distribution has proven to be the biggest challenge of this aspect of the research thus far, and any adjustments that reduce the variation of the strain distribution should be avoided if possible. Additionally, there is no basis for the 1mm aponeurosis in literature as compared to 3.125mm. Therefore, the original thickness will be retained as there is some physical evidence for its selection and the adjusted thickness does not seem to benefit the model in any major way.

However, this attempt does raise questions about whether the aponeuroses and muscle materials have appropriate stiffness for the simulations used in this project. The parameters for these materials were optimized using coupon testing of lapine TA muscle samples. Therefore, it is very possible that the values used may not transfer between species to the human TA model used

in these simulations. Further work could quantify this difference or even perform a similar fitting process if appropriate human TA testing data is acquired.

9. ACTIVE SIMULATIONS

A set of active contractile FEM simulations was conducted in accordance with the protocol outlined in Section 6. Output files from these simulations were analyzed in PostView to gather reaction force data from the distal face as well as pressure data from a group of elements deemed to represent the pressure sensor implantation region of Go's experiments. The final t=10s timestep was used to gather the force and pressure data. The reaction forces were averaged across the distal face nodes and exported from PostView, while the hydrostatic pressure and fluid pressure were averaged across the elements in the representative region and also exported. The data was then compiled and displayed in the sections below for discussion and further analysis.

9.1 INITIAL DATA AND TRENDS

The goal of this section of the research project was to iterate the overall stress level T_0 until the reaction forces matched that of Go's *in vivo* experiments (about 77.3N). Then, the corresponding pressure identified in the representative region of the mesh could be analyzed. An initial set of simulations was conducted at T_0=1, 5, 10, 50, 100, 150 and 200 kPa, to set a baseline. Overall figures of each simulation, midbelly slices and views of the distal face reaction forces are shown below for the T_0=10kPa simulation.

Because of the isometric nature of this simulation, there was little physical deformation of the model. Therefore, it was crucial to perform quantitative analysis of various qualities. A side-by-side comparison of the undeformed mesh at t=0s and the fully contracted mesh at t=10s are shown below in Figure 9.1.

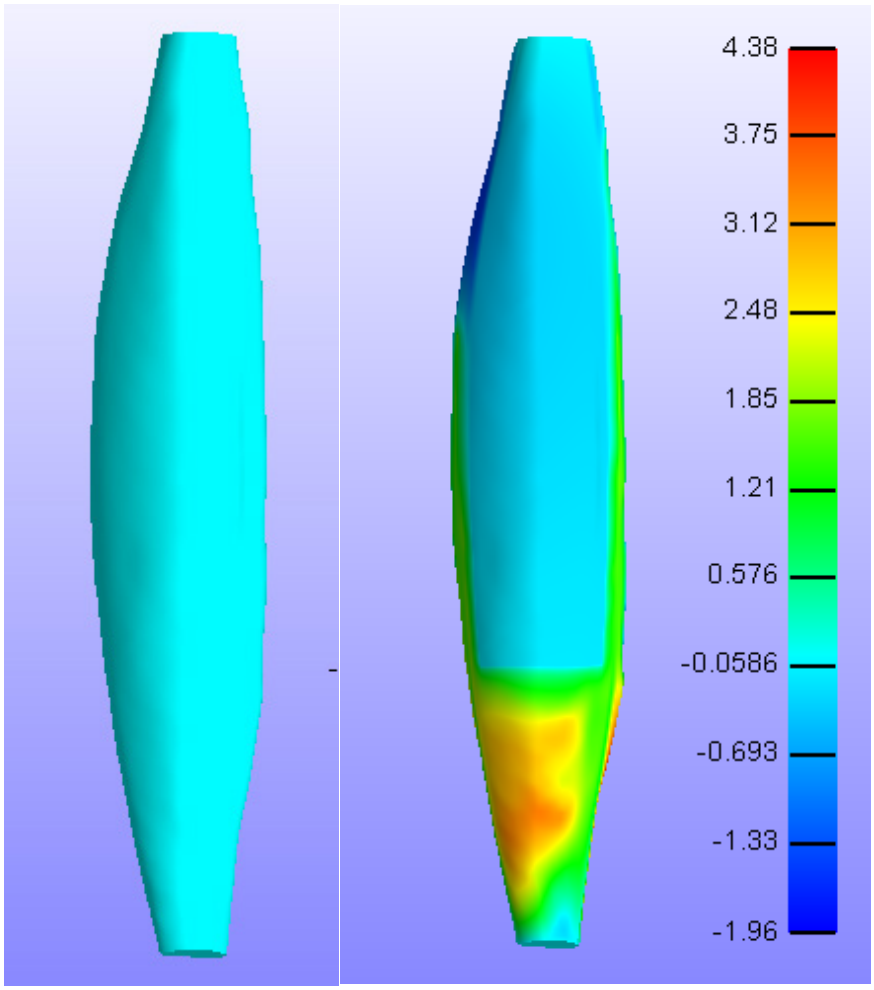

Figure 9.1: Comparison of initial (left) and final (right) mesh displacement gradients (mm)

As seen in the figure, there is very little change in the shape of the TA model from the initial to final timesteps. Also, the exterior aponeuroses appear to experience no displacement, but this will be touched on later in the analysis. Figure 9.2A-D below shows the four main views of the displacement gradient at the final timestep t=10s.

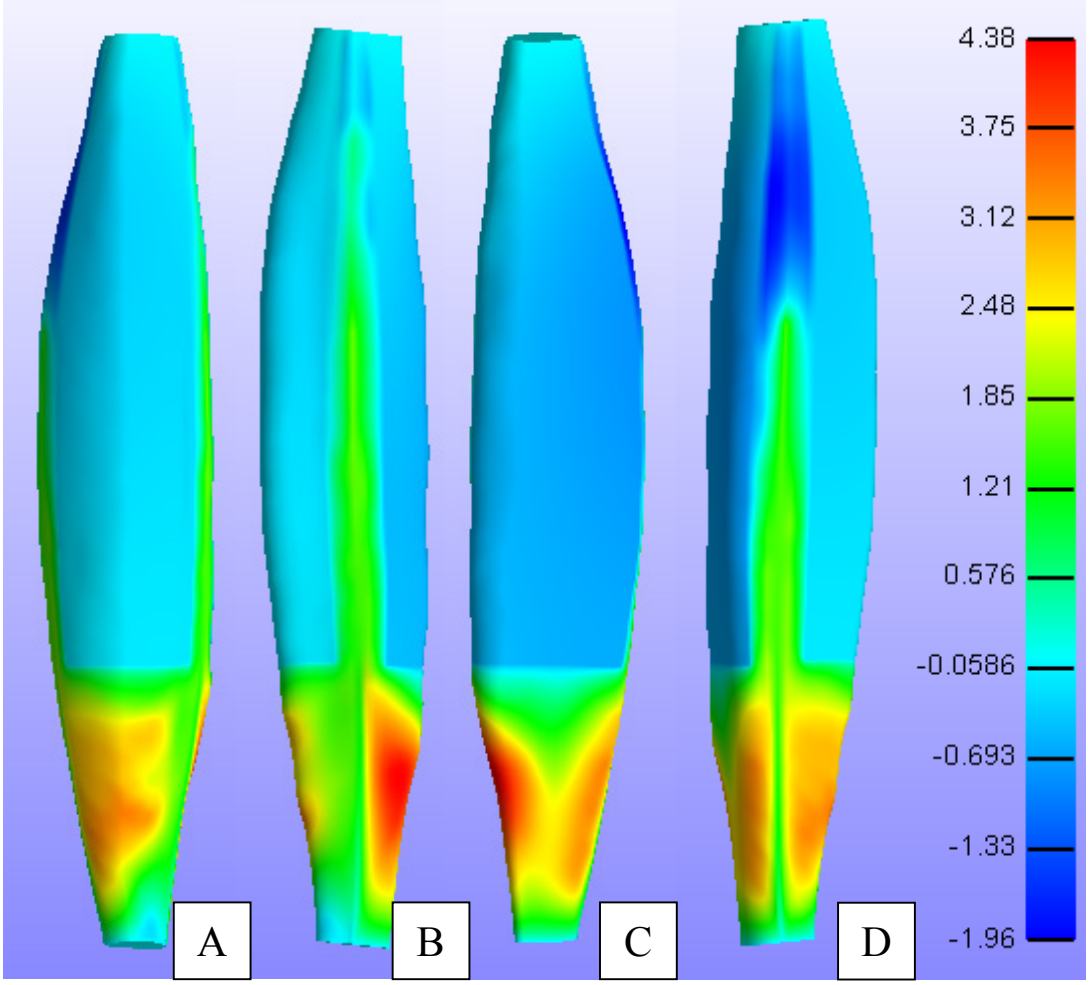

Figure 9.2A-D: Exterior views of the displacement distribution. The views are from the (A) Anterior, (B) Medial, (C) Posterior and (D) Lateral directions.

The figures above illustrate the deformation seen in the active contractile simulations. The main observation here lies in the lack of displacement seen in the exterior aponeuroses in general. The muscle portion distal to the exterior aponeuroses shows a positive (+Z) displacement, while the muscle beneath the exterior aponeuroses on the proximal end shows a negative (-Z) displacement. Together, these findings indicate a successful isometric contraction of the human TA muscle was modeled. The next set of Figures 9.3-9.6 portray longitudinal midbelly slices of the deformation, pressure and stress distributions.

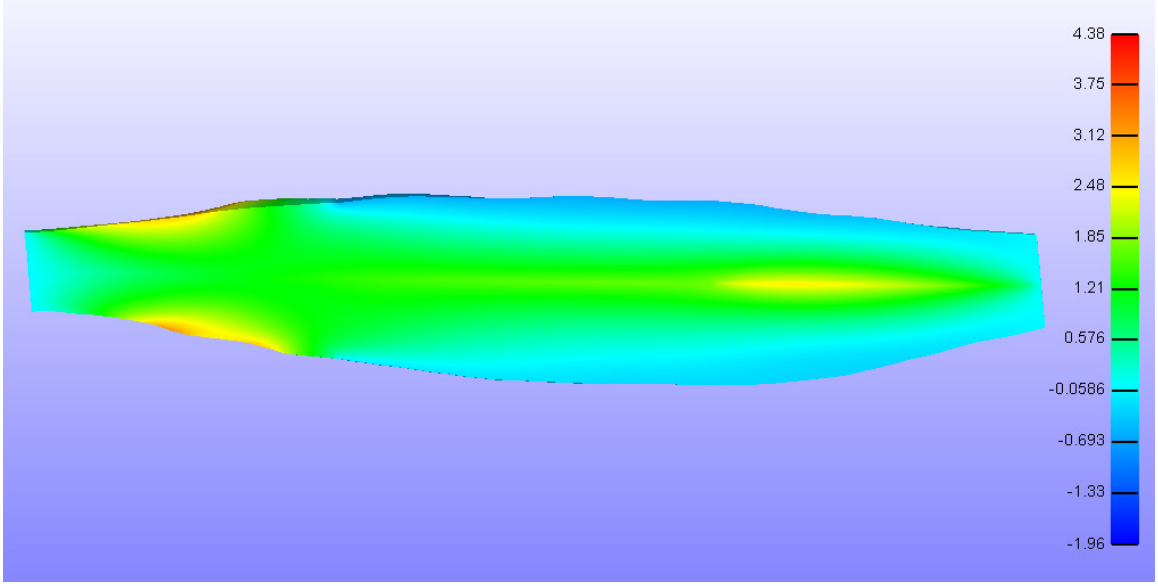

Figure 9.3: Midbelly slice of the Z-displacement distribution (mm).

The Z-displacement interior distribution follows the same trends as those identified previously. The distal muscle region has a positive displacement, while the exterior regions of the proximal muscle region nearest to the aponeuroses show a slight negative displacement, meaning both areas are getting pulled towards the center during contraction. As we may expect, the distal region experiences greater deformation because it contains half the quantity of stiff aponeurosis tissue as the proximal region.

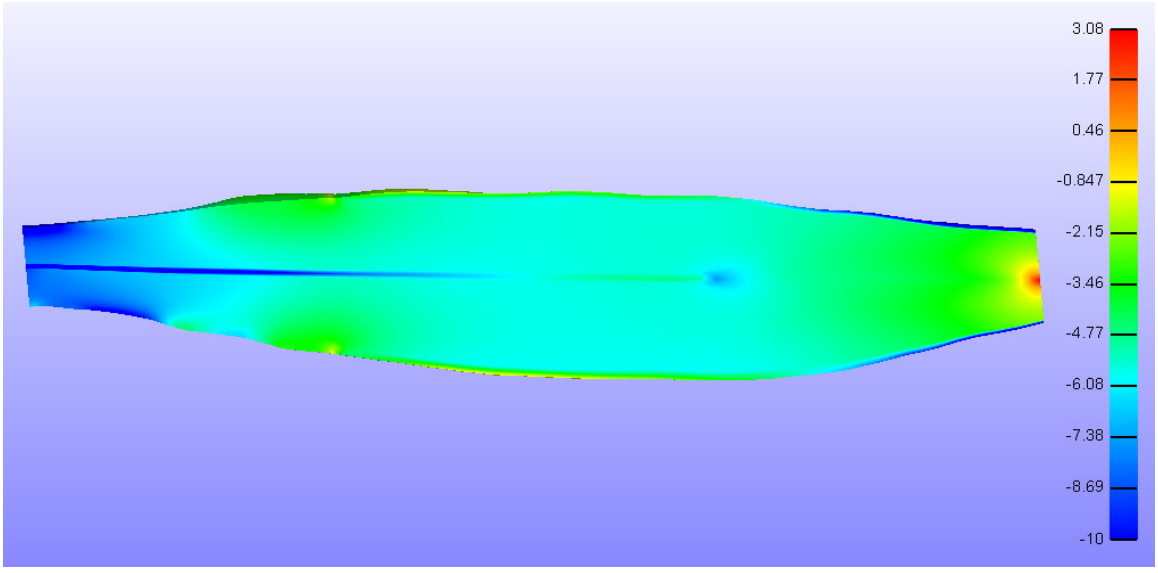

Figure 9.4: Midbelly slice of the hydrostatic pressure distribution (kPa).

The hydrostatic pressure distribution shows a generally negative (expansive) pressure, aside from a small artifact region near the proximal constraints. As seen in the passive lengthening simulations, the pressure tends to be more negative near the aponeurosis tissue due to greater application of stress occurring there.

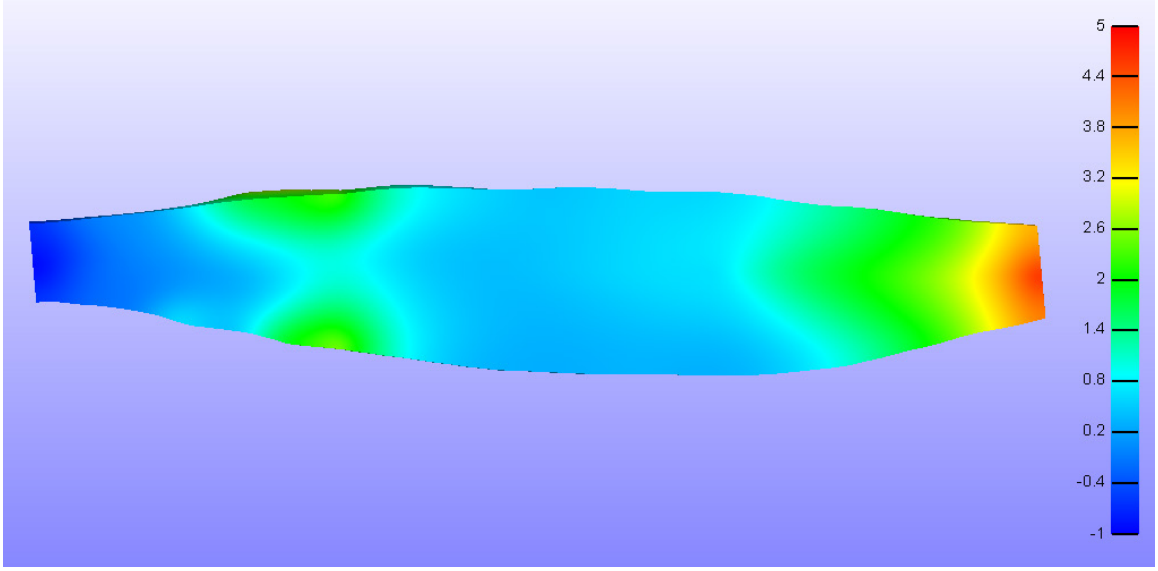

Figure 9.5: Midbelly slice of the fluid pressure distribution (kPa).

The fluid pressure distribution is mainly positive (compressive), but generally decreases in magnitude as we move distally in the model. Interestingly, the two pressure distributions appear very similar in terms of the color gradients, but the values themselves are very different.

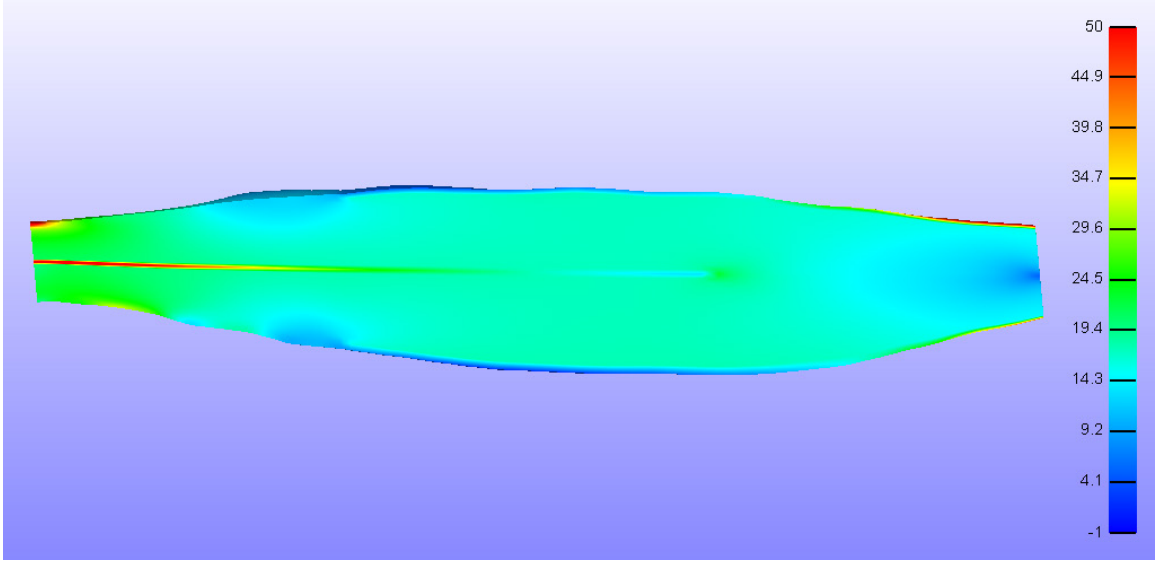

Figure 9.6: Midbelly slice of the Z-Cauchy stress distribution (kPa).

The Z-Cauchy stress distribution appears very uniform, with most values clustered around 15kPa. This is very different from the distribution seen in the passive lengthening simulations, when the muscle tissue did not transmit a significant portion of the load. Since the aponeuroses are not contracting in this simulation, it makes sense that the active muscle tissue now supports a stress. However, the peak stresses are still seen in the extreme sections of all three aponeuroses, where the values peak above 50kPa.

The reaction force readings were taken exclusively from the distal face of the model, as these were the only nodes to undergo a prescribed displacement constraint (of 0). The typical appearance of the distal face at the final timestep t=10s is shown in Figure 9.7.

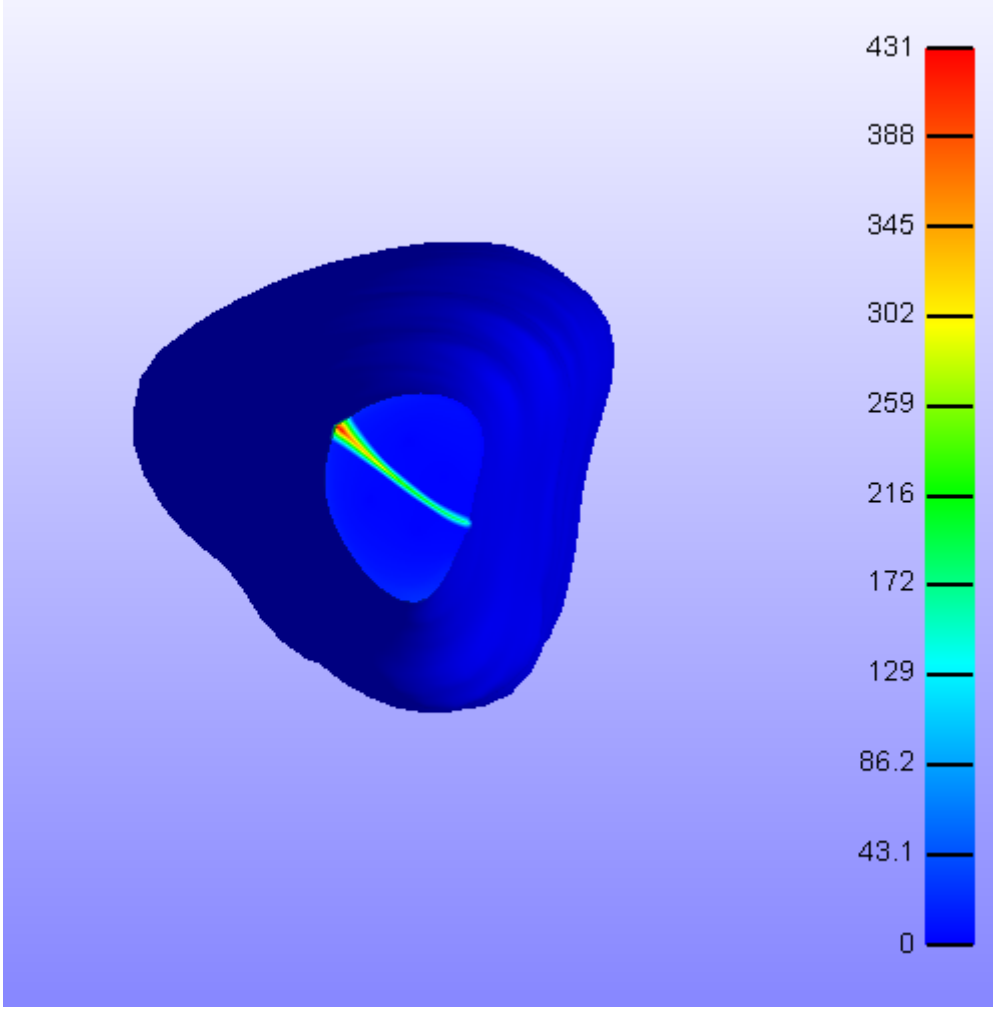

Figure 9.7: View of reaction forces on the distal face (mN).

The vast majority of reaction forces occur on nodes that are shared with the distal aponeurosis. Thinking about the vast disparity in material stiffness between the aponeurosis and muscle, it makes sense that the muscle is not able to sustain a significant portion of the load when compared to the distal aponeurosis. This likely is not realistic in terms of the physical muscle contraction. Nonetheless, averaging the reaction force over the entire distal face should still provide an accurate representation of the total reaction force generated by the model.

The figures in this section are all from the T_0=10kPa stress level simulation, chosen because it was in the intermediate range of the applied stress across all the simulations. All simulations possessed a very similar contour appearance for all the distributions discussed here. However, as

the stress level increased above 100kPa, a distinct distortion of the mesh was seen at the distal boundary of the exterior aponeuroses and the muscle tissue. This bulging is shown in Figure 9.8 below.

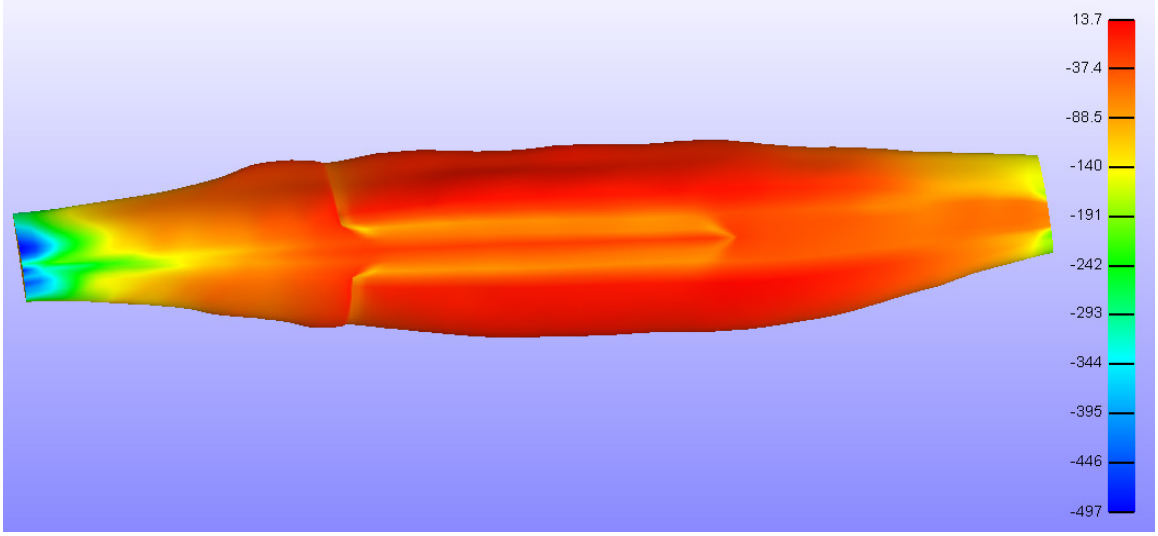

Figure 9.8: T0=100kPa distribution showing bulging at the distal boundary of the exterior aponeuroses and muscle.

Although this bulging is certainly not anatomically realistic, it can be attributed to the effect of the bidirectional contractions and the stiff exterior aponeurosis tissue. While it is an error to be remedied in the future, it should not affect either the reaction force or pressure data collection as the sources for both measurements are a significant distance from the site of the distortion.

9.2 QUANTITATIVE RESULTS / PLOTS

The total reaction force and average pressure in the chosen representative region were calculated for each simulation. To determine total reaction force, all the nodes on the distal face were selected (649 in total), and the average reaction force across this node set was output from PostView. A weighted average was used that normalizes the data based on corresponding element volume so as to prevent small element artifacts from skewing the data. For pressure, a cube of approximately $1mm^3$ was created in the belly of the muscle, precisely 1/3 of the length of the muscle from the proximal end. Aside from matching the protocol of Go's active contractile experiments, this region possessed a relatively stable pressure gradient according to the midbelly

slices taken previously. The elements in this cube were selected and their hydrostatic and fluid pressures output as weighted averages. Figures 9.9-9.11 below describe the distal reaction force and pressure collection methods.

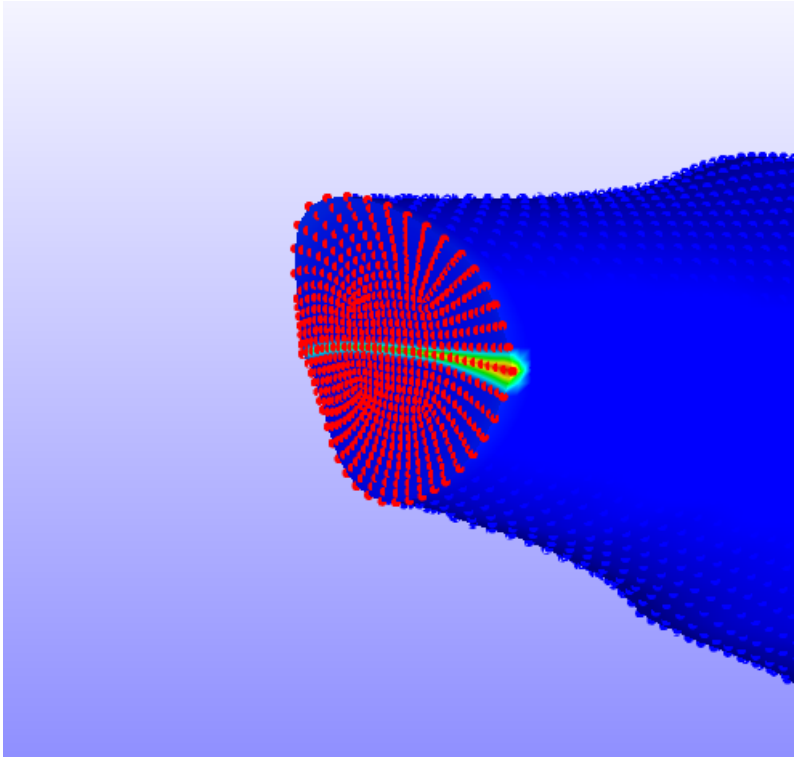

Figure 9.9: Screenshot of node selection for reaction force calculations.

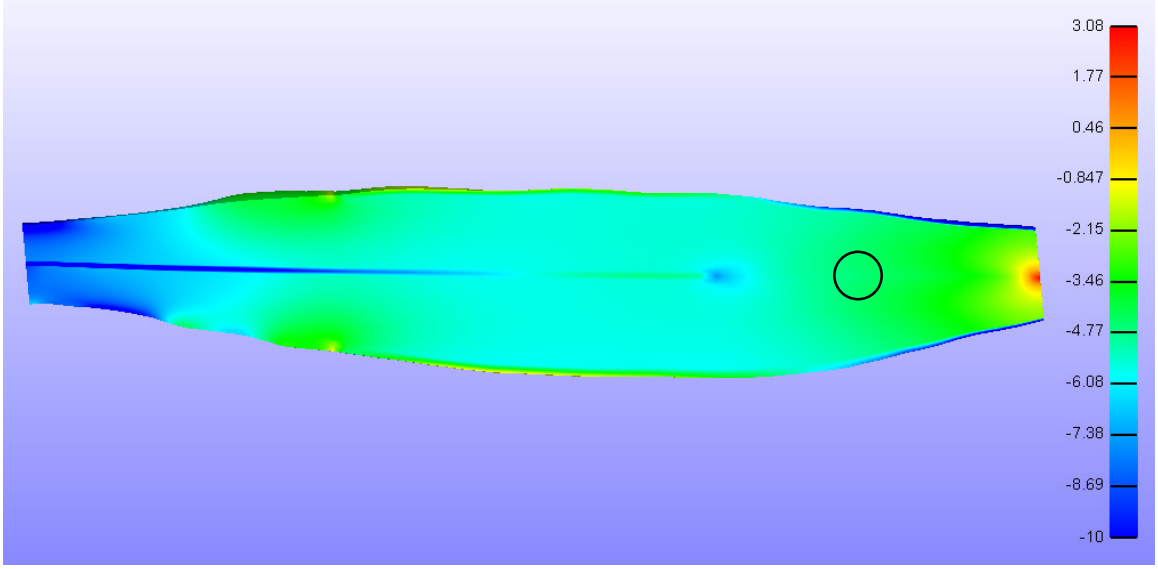

Figure 9.10: Midbelly slice of hydrostatic pressure distribution illustrating approximate location of pressure sampling point.

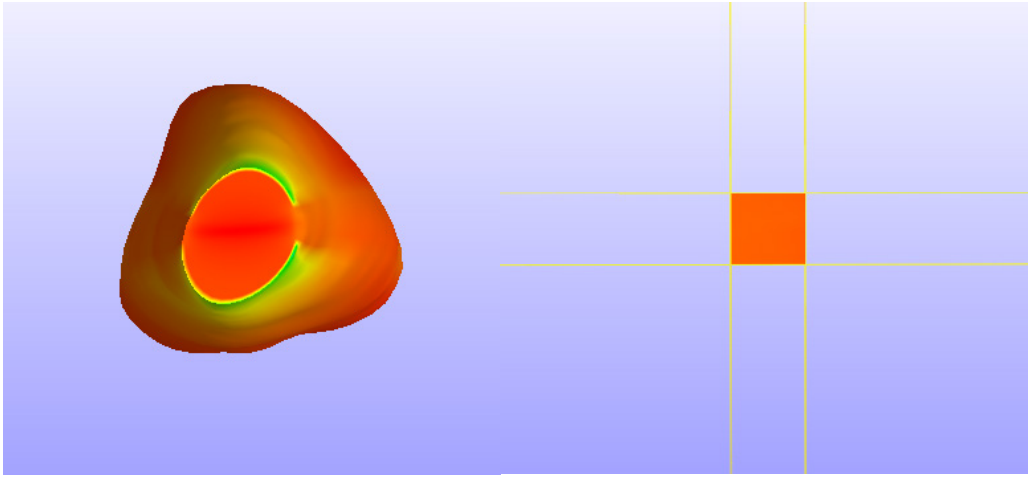

Figure 9.11: Side-by-side comparison of overall model (left) and the pressure sampling region (right). Yellow lines indicate the cutting planes used to define the region.

Reaction force and pressure data for the seven different stress level simulations were gathered using the methods described above. Table 9.1 below describes the reaction force and pressure output from each active contractile simulation.

Table 9.1: Pressure and reaction force data for the initial active contractile simulations.

Stress Level (kPa)	Hydrostatic Pressure (kPa)	Fluid Pressure (kPa)	Reaction Force (N)
1	-0.548	0.078	1.313
5	-2.575	0.642	6.21
10	-4.954	1.526	11.609
50	-22.164	9.042	42.599
100	-41.589	17.193	74.831
150	-59.566	25.373	105.306
200	-76.976	33.354	134.922

In the data analyzed from Go's experiments, the target reaction force is 77.3N, while the target IMP is 3.43kPa. As seen, the target reaction force falls at a stress level slightly higher than 100kPa. The hydrostatic pressure values are all negative (expansive) in nature, while the target IMP value is 3.43kPa. An equal magnitude pressure is achieved between 5 and 10kPa for the stress level. Similarly, a fluid pressure value of 3.43kPa would occur between the stress values of 10 and 50kPa. One encouraging finding lies in the relatively linear change in reaction force or pressure with a corresponding change in applied stress. These relationships will be examined further in Section 9.3.1.

9.2.1 APPROPRIATENESS OF PRESSURE READINGS

Unlike the passive lengthening simulations, the active contractile *in vivo* data provides a benchmark for IMP to compare to the FEM simulations. From Section 5, we are looking for a peak pressure of approximately 3.43kPa when the reaction force is around 77.3N.

An immediate issue that arises is the negative hydrostatic pressure seen in the FEM simulations. This does not match the positive IMP seen in Go's studies. However, when one considers physics of the active contraction in the FEM simulation, the negative values seem to make sense. Although the tissue itself is undergoing a contraction, the isometric nature of the contraction means that the muscle is generating tension since the ends of the model are pinned in place.

Tension in the muscle would correlate to positive stress in the Z-direction. Since this stress dominates the principal stresses, it would thus carry over to a positive trace of the stress tensor. Since FEBio outputs hydrostatic pressure as the opposite of the trace of the Cauchy stress tensor, this pressure would therefore be negative. Although this is correct mathematically, it moves us no closer to an accurate IMP reading. Therefore, this measurement suggests that, if IMP is dependent upon hydrostatic pressure during isometric contractions, it is not solely so.

On the other hand, the fluid pressure rises proportionally from 0kPa with corresponding increases in the applied stress level. The fluid pressure appears to be slightly less than half of the hydrostatic pressure, and opposite sign, at any given stress level. Because fluid pressure seems to intuitively be a better fit for modeling IMP (hydrostatic pressure is more related to deformation than it would be to an actual pressure reading), the positive fluid pressure values seen here are encouraging. However, in the realm of an appropriate reaction force of 77.3N (74.831N at T_0=100), the fluid pressure is 5-6 times the target IMP value of 3.42kPa (17.193kPa). Nonetheless, this is a good first attempt in the efforts to model the behavior of the human TA muscle with a high degree of accuracy.

9.3 SUBSEQUENT ATTEMPTS

Once again, several subsequent active contractile simulations were conducted to further examine the relationship between reaction force and pressure in the model, and ideally push the values closer to those found in Go's *in vivo* studies.

9.3.1 ITERATED STRESS LEVEL

Since the primary goal of this section of the project was to iterate T_0 stress values until a reaction force was found that matched that of Go's experiments, this was the first additional simulation conducted. The reaction force and pressure readings were plotted vs. the overall stress level T_0 below in Figures 9.12-9.14. The target pressure and load values are shown on the fluid pressure and reaction force plots as horizontal lines.

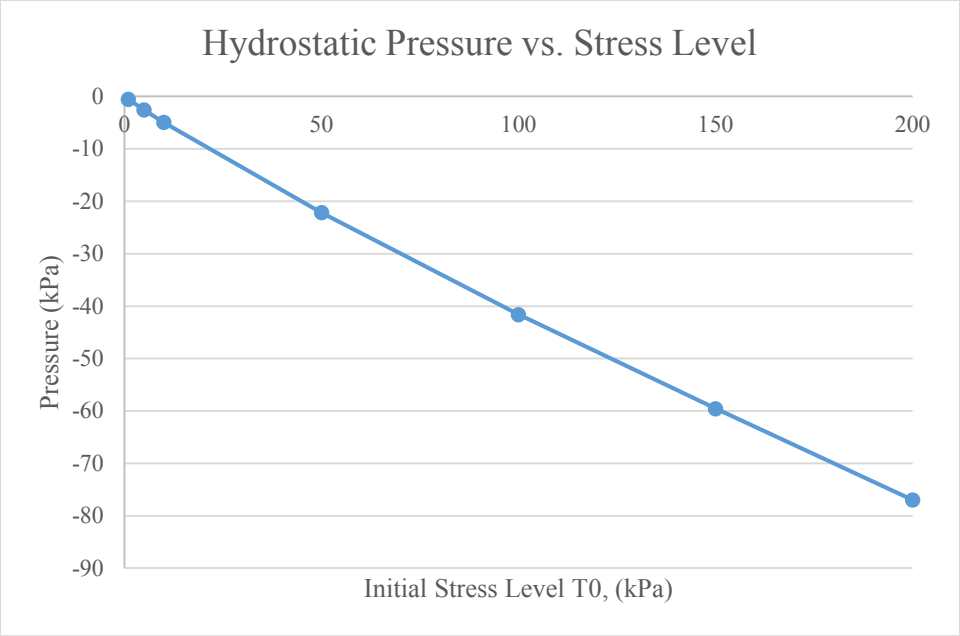

Figure 9.12: Hydrostatic pressure values (kPa) plotted against the T_0 stress values (kPa)

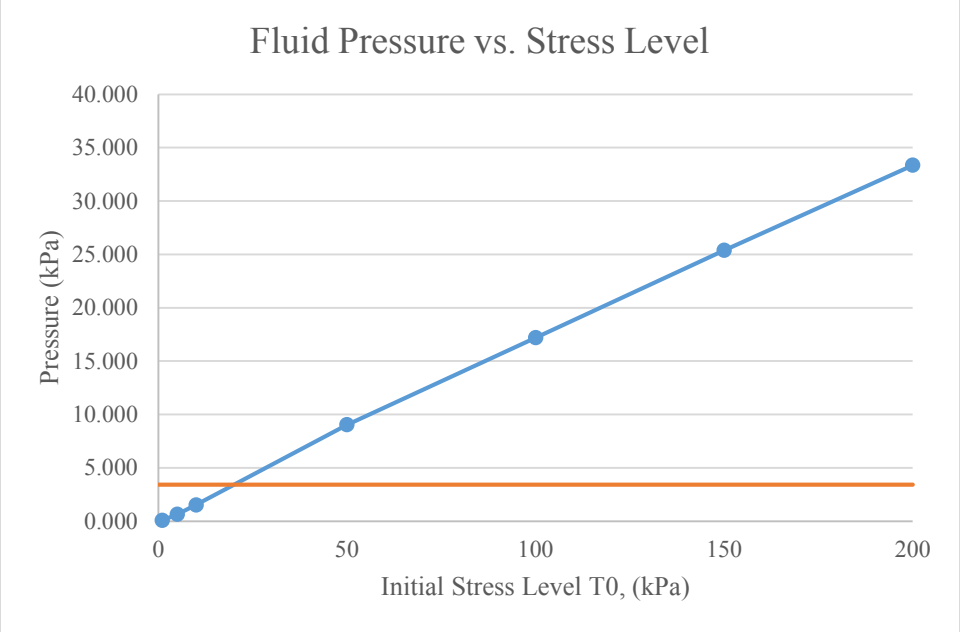

Figure 9.13: Fluid pressure values (kPa) plotted against the T0 stress values (kPa)

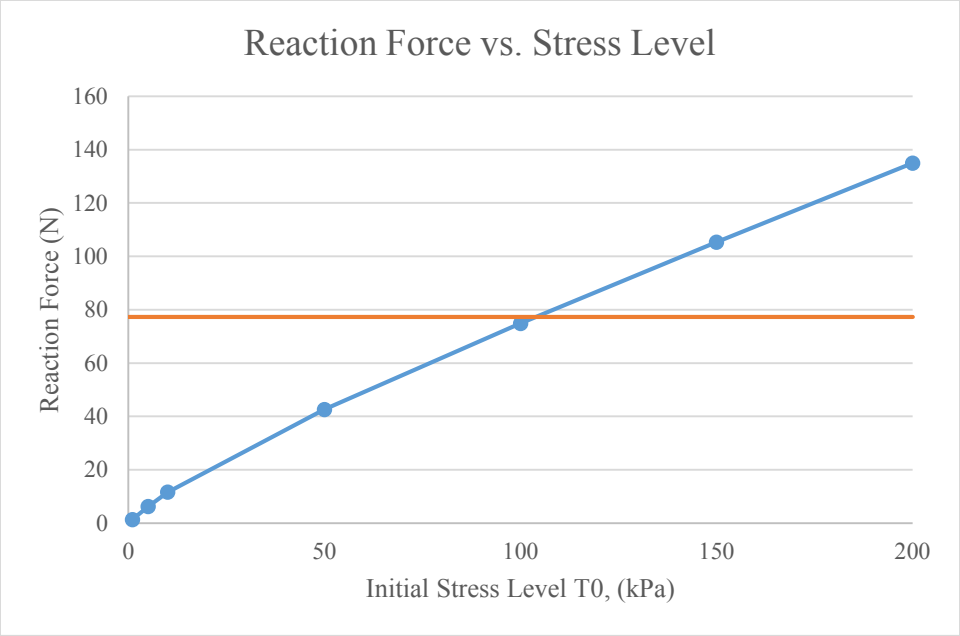

Figure 9.14: Reaction force values (N) plotted against T0 stress values (kPa)

As seen above, the desired reaction force of 77.3N seems to fall just above the stress level T_0=100kPa. Although the data does not follow a strictly linear pattern, the decrease in slope with increasing stress was gradual enough that a linear approximation could be used to determine intermediate points. After interpolating the data, a simulation was conducted at T_0=104kPa because it was believed this value would result in a total reaction force very close to 77.3N. However, the true pressure values lie at a much lower stress value. Two more rounds of interpolation were conducted to determine a stress value that provide a hydrostatic pressure and fluid pressure magnitude closest to 3.43kPa. The results of these simulations are shown in Table 9.2 below.

Table 9.2: Updated active contractile simulation statistics. Values shown in bold indicate those of the second round of simulations done to match experimental data.

Stress Level (kPa)	Hydrostatic Pressure (kPa)	Fluid Pressure (kPa)	Reaction Force (N)
1	-0.548	0.078	1.313
5	-2.575	0.642	6.210
6.8	**-3.444**	0.976	8.238
10	-4.954	1.526	11.609
20	-9.459	**3.492**	20.665
50	-22.164	9.042	42.599
100	-41.589	17.193	74.831
104	-43.202	17.956	**77.315**
150	-59.566	25.373	105.306
200	-76.976	33.354	134.922

Each simulation proved very effective in achieving its desired parameter value. The T_0=6.8kPa simulation resulted in a hydrostatic pressure of -3.444kPa. The T_0=20kPa simulation achieved a 3.492kPa fluid pressure, and the T_0=104kPa simulation output a 77.315N reaction force. All values were well within 1% error of the experimental values. However, the complementary parameter in each of these simulations does not effectively match the values from Go's *in vivo* experiments. The simulations that match the hydrostatic and fluid pressures have reaction forces of 8.238 and 20.665 N, respectively, the closest of which is still slightly less than a factor of 4 from matching the true reaction force from Go's data. Conversely, the reaction force-matching simulation (T_0=104) has hydrostatic and fluid pressures of -43.202kPa and 17.956kPa, the closest of which is again 5.25 times greater than expected. This shows that there is considerable work to be done with this model before it can be expected to achieve accurate results for the human TA. However, the ability to effectively match either parameter is a good stepping stone for future developments in these simulations. Furthermore, the fluid pressure appears to better match the data than the hydrostatic values, even when simply examining the magnitudes of each parameter. This is in line with previous theories that fluid pressure better approximates the IMP distribution than the stress-based hydrostatic pressure.

There are several lengthier methods by which this model could be adjusted to ideally bring the reaction and pressure values closer to those from Go's experimental data. These changes will be discussed in Section 10.

9.3.2 CONTRACTILE APONEUROSES

A second adjustment to the active contractile simulations was the addition of contractile aponeurosis tissue. This was an attempt to resolve the distortion of the mesh at the boundaries of the exterior aponeuroses and the muscle tissue. Although connective tissue like fascia and internal aponeuroses is typically not considered contractile, there is evidence of smooth-muscle-like contractile behavior seen during voluntary muscular contraction 18]. There is also evidence of internal aponeurosis shortening during some muscular contraction, which may indicate contractile behavior [19]. A simulation was conducted after adding the active contraction modules into the aponeurosis materials at a stress level of T_0=6.8kPa to use an appropriate range for the pressure values. This required separating the three aponeuroses into individual material distinctions because of their different contractile directions. The anterior and posterior aponeuroses were made to contract in the same direction as their respective muscle components, while the distal aponeurosis contracted along the longitudinal (Z) axis due to its model symmetry. The contractile aponeurosis simulation was run at T_0=6.8kPa and T_0=50kPa. Figures 9.15-9.16 show the midbelly pressure distributions for the T_0=6.8kPa pair.

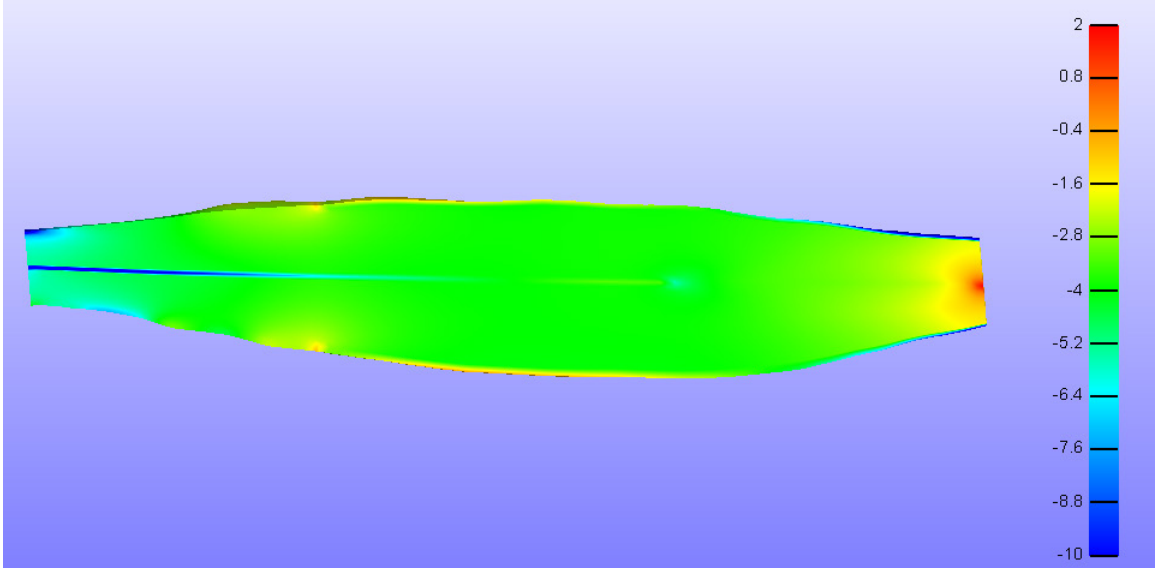

Figure 9.15: Midbelly slice of the pressure distribution for the original T_0=6.8kPa simulation.

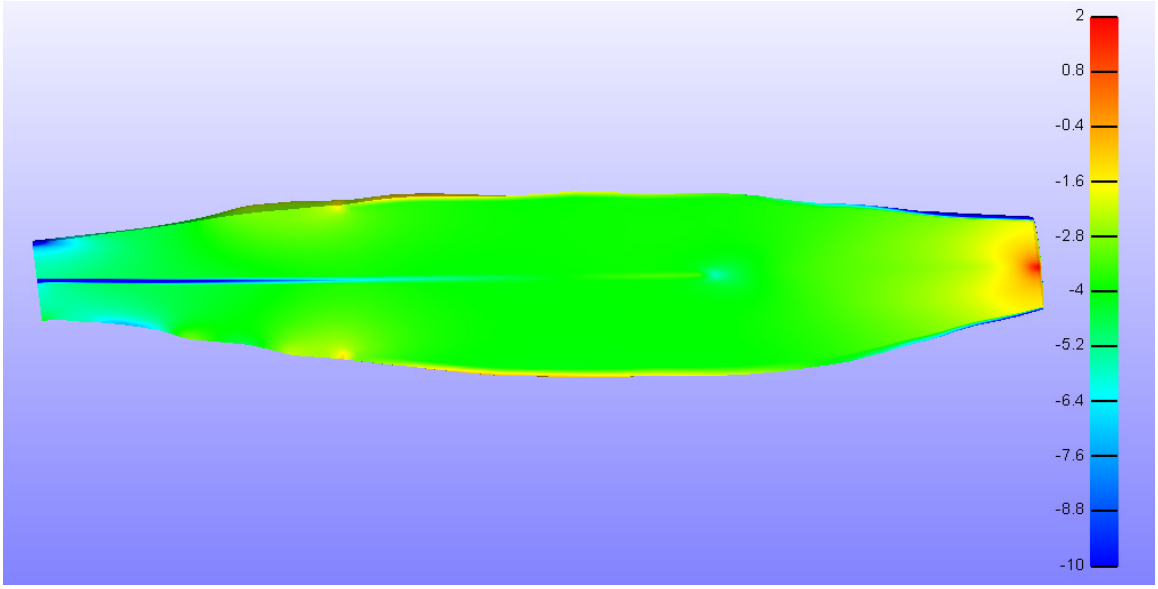

Figure 9.16: Midbelly slice of the pressure distribution for the T_0=6.8kPa contractile aponeuroses simulation.

As seen above, minimal changes in the hydrostatic pressure distributions are seen between the original and contractile aponeurosis simulations for T_0=6.8kPa. The shape of the distribution appears to be slightly more anatomical in the distortion region, but this issue will be easier to analyze when looking at the distributions for stress level T_0=50kPa below in Figures 9.17-9.18.

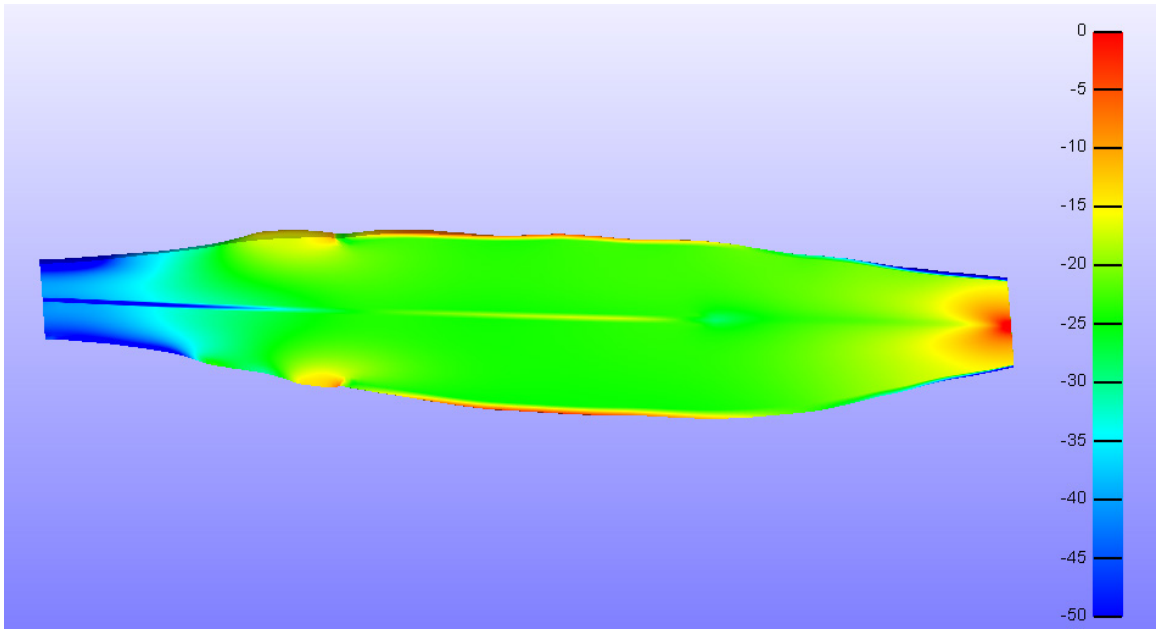

Figure 9.17: Midbelly slice of the pressure distribution for the original T_0=50kPa simulation.

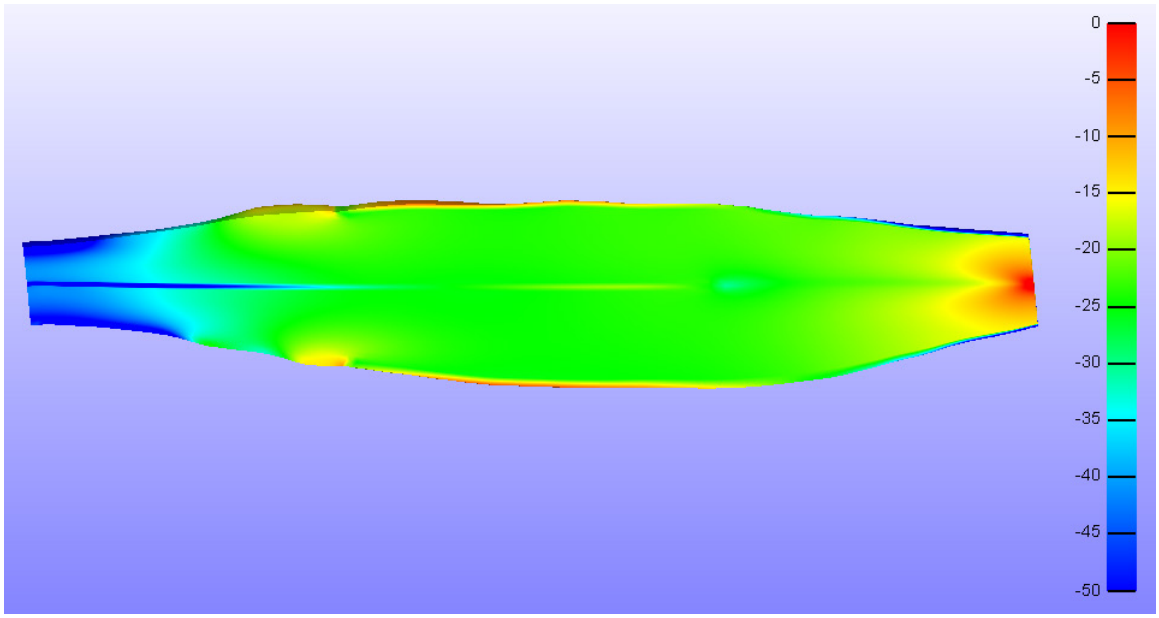

Figure 9.18: Midbelly slice of the pressure distribution for the contractile aponeurosis T_0=50kPa simulation.

Once again, the pressure distributions for the original and contractile aponeurosis simulations for T_0=50kPa appear virtually identical. However, there is a small decrease in the amount of distortion seen at the distal boundary of the exterior aponeuroses. Although the bulging effect is

not completely eliminated, it does appear to be slightly less apparent for the simulation with aponeuroses included in the contractions. This is likely because the exterior aponeuroses are contracting in the same bidirectional motion as the muscle tissue, thus preventing the build-up of muscle material behind the exterior aponeuroses. However, the applied stress induces less displacement in the aponeurosis tissue because of its greater stiffness, meaning that the muscle material distal to the exterior aponeuroses still experiences greater strain. Nonetheless, this adjustment shows promise as a potential fix for the mesh distortion issues. A quantitative analysis of the parameters of interest is shown below in Table 9.3

Table 9.3: Comparison of the original and contractile aponeurosis (CA) simulations, showing the percent change of the new values over the originals

Stress Level (kPa)	Hydrostatic Pressure (kPa)		Fluid Pressure (kPa)		Reaction Force (N)	
6.8	-3.444	-2.1%	0.976	-4.9%	8.238	4.6%
CA - 6.8	-3.516		0.928		8.618	
50	-22.164	-0.7%	9.042	-1.4%	42.599	14.3%
CA - 50	-22.329		8.911		48.675	

The results from the table highlight some potentially useful findings. The table illustrates the percent change from the standard simulations. In the previous section, we discovered that pressure readings were generally too high or reaction forces too low. Therefore, it is an encouraging sign that contractile aponeuroses tend to decrease both the hydrostatic and fluid pressures as well as increase the measured reaction force. Although the contractile aponeuroses did not fully resolve the mesh distortion problems, this adjustment could prove very beneficial for getting the pressure and reaction force values closer to those from the *in vivo* benchmarks.

9.3.3 STRAIGHT CONTRACTION

The final post-hoc simulation involved changing the differing contraction directions to a simple, longitudinal (Z-axis) contraction of the tissue. This was another attempt to resolve the mesh distortion, as the muscle tissue could then avoid "bunching up" at the distal boundary of the

exterior aponeuroses due to the off-axis contractions. This could also counteract the negative hydrostatic pressure values seen, if the ±5° contraction angles were causing significant positive stresses in the transverse directions. In this simulation, the muscle contractions (aponeurosis contractions were not input for this run) were set along the Z-axis. However, this adjustment did not yield any useful quantitative results. There was no reduction in mesh distortion seen, and the straight contraction served to increase the representative pressure output in both T_0=10kPa and 100kPa simulations, while decreasing the total reaction force along the distal face. As such, this adjustment did not result in any helpful changes to the simulation results and also moved away from the true biomechanical process of contraction in the bipennate directions. Therefore, the straight active contraction should not be pursued any further.

10. DISCUSSION

Following the completion and analysis of all simulations, a discussion of the overall findings of the research project and recommendations for the next step in the work were created.

10.1 SUMMARY OF FINDINGS

Jensen's data showed a strong trend of positive volumetric strain during passive lengthening of the TA, with typical values between 2-4% but up to 20% or more in some slices. She observed an increasing trend in volumetric strain in the anterior, medial and distal directions within the muscle. Go's data illustrated a very strong correlation between IMP and muscular force. Small fluctuations in the force data were reflected very closely in the IMP values. The average peak load measured was 77.331N, and the average increase in IMP over the course of the active contraction was 3.43kPa.

A mesh convergence study analyzed the average hydrostatic pressure in the muscle material at the end of the passive lengthening simulation. The fifth mesh resulted in a change in average pressure of only 1.22% over the fourth mesh, so it was selected for use in the remainder of the

simulations. Because a further increase in mesh density is likely to result in an even smaller improvement in pressure accuracy (likely <1% change), this fifth mesh was deemed appropriate for use in the subsequent portions of this research project. The chosen mesh contained 95114 elements, an increase from the 12734 elements found in the original mesh modeled after that of Jensen's experiments.

The passive lengthening simulation shows significant variation in volumetric strain on the exterior surface, but the distribution is much more uniform in the interior of the mesh. Significant areas of compressive volumetric strain are seen in the mesh, whereas Jensen's data did not show any negative strain (even though her raw mesh values did appear to contain some compressive strain). These compressive strain regions typically border the stiffer aponeurosis tissue, suggesting that the skewing of elements connected to the aponeuroses or transverse compression may result in a decrease in net volume.

Findings gathered from the pressure distributions also support this claim that the stiff aponeuroses have a significant effect on the simulation results. Positive (compressive) pressures are seen in the regions between the aponeuroses, again suggesting that the transition between the stronger components of the model causes a compressive effect on the muscle material between. Examination of the stress and deformation gradients uncovers the final piece of this theory. The transverse (X- and Y-directions) stresses show compressive regions between the three sets of aponeuroses. The Z-Cauchy stress gradient shows how the transmission of the deformation load does not traverse the belly of the muscle, but rather spans from the distal aponeurosis diagonally through the muscle tissue to the distal boundary of the exterior aponeuroses. Because of this, there is no Z-stress seen in the X- and Y- compressive stress regions, and thus the hydrostatic pressure (sum of principal stresses) becomes compressive in this area. In examining the Z-displacement contour, the steep diagonal gradient seen in this compressive pressure region indicates that some relaxation in the muscle tissue is occurring, likely leading to the compressive stresses. The induced load from displacement is transmitted between the aponeuroses by a narrow band of muscle tissue. The remaining muscle tissue contains minimal stress in the

longitudinal direction, but is compressed by the narrowing of the muscle as a result of elongation. This may explain some of the negligible or compressive volumetric strains seen, as well as the positive pressures in these areas.

Quantitative slice plots illustrated smaller volumetric strains on average than those seen in Jensen's data (0-2% as opposed to 2-4%). However, the FEM simulation data did share some of the same trends as those found in Jensen's data. Specifically, all sections have a peak strain on the medial side of the mesh. Additionally, aside from SI5, the remaining slices show an increasing trend as one moves from proximal to distal within the model. The hydrostatic and fluid pressure plots show increased uniformity within the model than the volumetric strain distribution, mainly in the transverse direction. This indicates that the longitudinal position of a pressure sensor placed in the TA muscle will have a greater effect on the reading than the transverse position.

Post-hoc adjustments to the model determined that a reduction in the bulk modulus approximation could result in favorable changes in the volumetric strain distribution, but this should be done after fixing larger issues with the model. The biphasic nature of the constitutive model is critical for providing compressive stiffness, and should not be removed. The use of quadratic elements could provide an additional level of accuracy within the model, but 2nd order shell elements are not yet supported by FEBio. Decreased shell thickness of the aponeurosis elements did not significantly affect the results.

The active contractile simulations effectively model a contraction by pulling the distal and proximal regions of the model towards the center of the mesh. The distal region of the mesh experiences greater deformation since less of the stiff aponeurosis tissue is modeled there. The hydrostatic pressure during contraction is generally negative (expansive). This is because, due to the isometric nature of the contraction, the muscle is actually in tension as the stress is generated, causing a tendency to increase in volume. The muscle fibers must support a stress during these simulations because they are actually generating the contraction, so the Z-stress distribution is

much more uniform than that of the passive lengthening simulations. Reaction force readings were clustered densely around the nodes of the distal aponeurosis that intersect the distal face. This is because the stiffness of the aponeurosis material dwarfs that of the muscle, meaning it sustains much more of the load induced by the contraction stress. Increasing the effective stress level above 100kPa results in distortion of the mesh around the distal boundary of the external aponeuroses as the muscle fibers try to contract out around them. This is not anatomically realistic, and several attempts were made to remedy this.

Within the active contractile simulations, the most accurate reaction force reading was found at a stress level of 104kPa (77.315N), while the most accurate hydrostatic pressure magnitude was found at the 6.8kPa stress level (3.444kPa) and at 20kPa stress for the fluid pressure (3.492kPa). These findings suggest that fluid pressure was a better measure of IMP than hydrostatic pressure for this simulation. However, the fluid pressure reading was still significantly higher than the value seen in literature. This is consistent with findings from ongoing lapine simulations as well.

Of the post-hoc adjustments made in the active contractile simulations, the addition of contractile aponeuroses was the most beneficial. This adjustment lowered pressure readings while increasing the reaction force – the desired directions for both variables. This should be pursued further in future work. However, switching to a straight longitudinal contraction resulted in the opposite response, so it will not be analyzed any further.

10.2 RECOMMENDATIONS

This research project is the first foray into FEM simulations of the human TA model for the IP research group as all previous work has been done using lapine tissue. Because of the preliminary and exploratory nature of the work discussed here, perhaps the most important part of this project is generating useful suggestions and the direction for the next round of work to be completed. These recommendations, a total of 20, are discussed in this section.

10.2.1 MESH

The stiff aponeurosis elements are positioned around the exterior of the proximal face, but bisect the distal face. Because of this, the deep regions of muscle tissue did not sustain any stress in the passive simulations. Furthermore, the full reaction force was centered around the distal aponeurosis in the active simulations. Increasing the aponeurosis shell elements to cover the proximal and distal faces could induce greater strain in the muscle tissue without sacrificing anatomical correctness within the model. A similar change could use graduated aponeurosis thickness that decreases as one moves towards the center of the model or towards the extremes of the part regions. Although there is no concrete evidence for this, it is unlikely that the aponeuroses remain constant thickness until their termination within the muscle. Additionally, the longitudinal length and transverse width of the aponeuroses (especially the exterior ones) could be varied or decreased to study changes in the results. Doing this might put more load requirements on the muscle tissue, thus potentially increasing strain values. Either way, the interactions between aponeuroses and muscle tissue should be investigated with more depth, as this is the key to understanding the strain distribution within the FEM model. The lapine FEM model only contains aponeuroses at its proximal and distal ends in accordance with lapine anatomy; no aponeurosis tissue extends towards the center of the model. Therefore, the loads and stress must be transmitted by the muscle tissue. A final suggestion, in limbo for the moment, would be to use quadratic elements for greater accuracy at such time when FEBio begins to support 2nd order shell elements.

10.2.2 SIMULATION PARAMETERS

Recommendations for the simulation setup begin with more complete analysis of the human experimental data. The raw data from Jensen's study should be acquired and analyzed further to look for compressive strains seen within the model, especially in the posterior regions as shown in her figures. Go's active contractile study is ongoing, and as such the data can be appended when more experiments are conducted to gain robustness in the benchmark data. Similarly, Go mentioned that the pressure sensor tended to migrate distally within the muscle during her

experiments. If a more concrete position metric can be acquired, this will increase the accuracy of the IMP modeling approach, as the pressure distributions vary greatly in the longitudinal direction.

Within the FEM simulations, the full active contraction protocol can be followed if desired (the initial relaxed state, ramp of force, and relaxation phase). However, this will complicate the active contraction module within the FEBio material designation due to the initial hold phase. Finally, attempts should be made to revise the mesh distortion seen at the distal boundaries of the external aponeuroses. This may require revising the constitutive model (discussed below), but could also be done by adjusting simulation parameters.

Eventually, once accurate data can be compiled for this simple FEM simulation, greater depth should be added to the model through the inclusion of more surrounding tissues, such as fascia and the tibia. The disparity in volumetric strain readings between Jensen's data and the FEM simulations indicates that some mechanism of the physical stretching is not addressed properly in the FEM model. Perhaps the muscle is constrained more on its exterior to allow longitudinal stretching without significant narrowing in the transverse direction.

10.2.3 ANALYSIS

There are small strain artifacts seen in the passive lengthening data, specifically on the exterior of the model. Jensen mentions removing a fraction of the exterior MRI data to resolve artifacts before gathering slice data, and the same process could be done with the mesh. This is especially apparent at the longitudinal extremes of the model, likely due to the boundary conditions imposed there. Further examination should be conducted on the compressive volumetric strains seen in the passive lengthening models, as these differ significantly from the experimental data. This could be done with greater slice density, using half slices divided transversely, or with a different approach.

The elements in the representative pressure regions sampled in the active contractile data were manually selected within PostView. This may have induced a small variation in the data as a different number of elements was selected each time. However, the number of elements was kept within ±1% of the mean at all times to avoid the introduction of significant human error. A workaround for this issue would involve selecting a list of elements in the region in the model's unstressed state, then rerunning the simulation to output the pressures in these specific elements. Finally, experimentation should be done with various combinations of hydrostatic and fluid pressure to determine the best match to IMP. This can be done in tandem with the same work in other models, such as the previous lapine data in the research group.

10.2.4 CONSTITUTIVE MODEL

There is a second type of active contraction available within FEBio. This involves inputting maximum calcium ion concentrations as well as optimal muscle fiber length, among other parameters. This simulation was not conducted for this research project as it is a logical second step after the first prescribed active contraction. The active contraction used in this report treats the muscle as a single sarcomere for each contraction direction. While this is certainly not anatomically accurate, it does offer a good foundation for future work in active contractile simulations for the model. Contractile aponeuroses showed promise for pushing the model towards more accurate results, so this theory should be pursued in future iterations. Similarly, decreasing the bulk modulus approximation for the muscle material also proved potentially worthwhile, but only after addressing larger disparities between the model and reality. Additionally, if human muscle testing data can be gathered to show mechanical testing of the TA model in a controlled environment, this data can be used to more accurately fit the constitutive model to the human model for TA simulations. Overall, the aponeurosis tissue seems to be modeled with an excessively high stiffness. During passive lengthening virtually no portion of the model stress was transmitted through the belly of the muscle. This suggests that adjustments in the material stiffness should be made to correct this issue. Further out, perhaps a graduated stiffness could be applied to the aponeuroses to model their assimilation into the muscle tissue. The extremes of the aponeuroses, both longitudinally and transversely, could have a lower

stiffness than elements in the center of the tissue. This would provide smoother transitions between the connective tissue and the muscle body, and likely more accurate results with less distortion of the mesh.

11. CONCLUSIONS

This research project served as an introduction of a muscle material constitutive model, previously only used in lapine work, into a mesh of a human tibialis anterior muscle and the relevant connective tissue. Human experimental data was analyzed and used as a benchmark for passive lengthening and active contractile simulations. A functional FEM model was constructed to conduct passive stretching simulations, and an active contraction module was added to the material designations in order to achieve isometric contraction. Over 50 unique FEM simulations were conducted to analyze different aspects of the muscle model and make initial adjustments in a push towards greater accuracy in the results. Volumetric strain, hydrostatic pressure, fluid pressure and reaction forces were analyzed during post-processing and output in a thorough graphical and quantitative analysis.

Analysis of the simulations indicates relatively lower volumetric strains seen in the model than Jensen's experimental data, on average. A mechanism for passive stretching and active contraction was theorized, with the aponeuroses bearing the majority of the load due to their high stiffness. Compressive volumetric strains seen in the passive lengthening data are believed to be due to transverse narrowing of the tissue as it lengthens occurring in tandem with the skewing of elements that directly border the exterior aponeuroses. Fluid pressure seems to have a stronger correlation with known IMP values than hydrostatic pressure, which conforms to current theories within the IMP research group. Fluid pressures for the active contractile simulations were higher than expected, likely owing to the stiffness of the aponeuroses being greater than necessary.

For a first attempt, good success was achieved in the similar trends seen in data from both simulation types. The results that did not match human data can be explained via investigations

into the contours of various parameters within the model, such as stress and displacement values. A complete list of recommendations for the model was compiled and listed in the discussion to be used in future iterations of this research project.

Looking back at Section 1.4, both goals for the project have been accomplished. Experimental data was analyzed, and a quality mesh was setup to conduct both passive and active simulations of the human tibialis anterior muscle. The results of these simulations were compiled and analyzed, and correlations were drawn between the results of this work and those of the experimental data from the Mayo Clinic. Disparities between the results were explained using the mechanics of the simulation, and preliminary adjustments were made to the mesh. Overall findings were discussed, and suggestions for future work provided in a concise manner.

12. REFERENCES

[1] B. Wheatley, private communication, Mar 2016.

[2] G. Odegard, private communication, Sept 2015

[3] E. Jensen, et al. "Characterization of three dimensional volumetric strain distribution during passive tension of the human tibialis anterior using cine phase contrast MRI," unpublished.

[4] J. Davis, et al. "Correlation between active and passive isometric force and intramuscular pressure in the isolated rabbit tibialis anterior muscle," J. Biomech., vol 36, pp 505-512, Nov. 2002.

[5] H. Gray. (2016, Mar 18). "8c. The muscles and fasciae of the leg" [Online, public domain]. Available: http://www.bartleby.com/107/129.html

[6] S. Go and E. Jensen, Human tibialis anterior cadaveric study, unpublished.

[7] University of Utah Musculoskeletal Research Laboratories. (2016, Mar 18). "FEBio help forums" [Online]. Available: http:// http://help.mrl.sci.utah.edu/help/index.jsp

[8] H. Khodaei, et al. "Simulation of active skeletal muscle tissue with a transversely isotropic viscohyperelastic continuum material model," Proc Inst Mech Eng H, vol 227, pp 571-580, May 2013.

[9] J. Grasa, et al. "A 3D active-passive numerical skeletal muscle model incorporating initial tissue strains. Validation with experimental results on rat tibialis anterior muscle," Biomech Model Mechanobiology, vol 10, pp 779-787, Oct. 2011.

[10] T. R. Jenkyn, et al. "Finite element model of intramuscular pressure during isometric contraction of skeletal muscle," Phys Med. Biol, vol 47, pp 4043-61, Oct. 2002.

[11] S. S. Blemker, et al. "A 3D model of muscle reveals the causes of nonuniform strains in the biceps brachii," J. Biomech, vol 38, pp 657-665, Apr. 2005.

[12] B. Wheatley, IMP research group updates, unpublished.

[13] B. Wheatley, et al. "An optimized transversely isotropic, hyper-poro-viscoelastic finite element model of the meniscus to evaluate mechanical degradation following traumatic loading," J. Biomech, vol 48, pp 1454-1460, Feb. 2015.

[14] S. Go, Active contraction *in vivo* experimental data, unpublished.

[15] Stecco, et al. “Plantar fascia anatomy and its relationship with Achilles tendon and paratenon,” J. Anat, vol 223, pp 665-676

[16] C. N. Maganaris, V. Baltzopoulos. “Predictability of in vivo changes in pennation angle of human tibialis anterior muscle from rest to maximum isometric dorsiflexion,” Eur J Appl Physiol Occup Physiol, vol 79, pp 294-297, Feb. 1999.

[17] P. Fernandez. (2015, Mar 18). The Skeletal Muscle System [Online]. Available: http://web.gccaz.edu/~pfernan2/Chap10_Muscle.pdf

[18] R. Schleip, et al. “Active fascial contractility: Fascia may be able to contract in a smooth muscle-like manner and thereby influence musculoskeletal dynamics,” Med Hypotheses, vol 65, pp 273-277, 2005.

[19] M. Tilp, et al. “Length changes of human tibialis anterior central aponeurosis during passive movements and isometric, concentric, and eccentric contractions,” Eur J Appl Physiol, vol 112, pp 1485-1494, Apr. 2012.